# An Exploration of Tropical Cyclone Simulations in NCAR's Community Atmosphere Model

by

Kevin A. Reed

A dissertation submitted in partial fulfillment
of the requirements for the degree of
Doctor of Philosophy
(Atmospheric and Space Sciences)
in The University of Michigan
2012

Doctoral Committee:

Assistant Professor Christiane Jablonowski, Chair
Associate Professor Christopher J. Poulsen
Assistant Professor Mark G. Flanner
Michael F. Wehner, Lawrence Berkeley National Laboratory

To Mom and Dad

# ACKNOWLEDGEMENTS

The completion of this dissertation is a result of a collaborative effort and the support of many people. First and foremost, I say thank you to my thesis advisor and chair of my committee, Christiane Jablonowski. Christiane Jablonowski has provided great leadership by example and has helped to provide the underpinning of my future career. I look forward to the many years of collaboration to come. I also would like to thank the remainder of my committee, Chris Poulsen, Mark Flanner and Michael Wehner. I appreciate all of your provided advice and support.

In addition, I would like to thank Ricky Rood for his mentorship and advice over the duration of my graduate career. Many thanks to Michael Wehner for his essential role as my Department of Energy mentor as part of my graduate fellowship. In addition to our joint research interests, Michael Wehner has provided great career advice. I thank Jerry Olson, David Williamson, Andrew Gettelman and Brian Medeiros at the National Center for Atmospheric Research for their advice and help on model setup and configurations in Community Earth System Model, the main model used throughout my graduate research. Thank you David Nolan (University of Miami) for providing the axisymmetric model that inspired the development of the analytic initial conditions. I also thank Mark Taylor at Sandia National Labs for his support and ideas when using the High-Order Methods Modeling Environment.

Thank you Kristi Hansen, Sandee Hicks, Margaret Reid, Cheri Champoux Johnson, Barbara Lupi and Sandra Pytlinski for the superb administrative support. You ladies have saved me countless hours of work throughout the years.

Last but certainly not least I thank all of my family and friends, without whom my success and the completion of my degree would not have been possible. I thank my Mom and Dad who have lead by example and provided me with countless opportunities to succeed not only in academics, but in life as well. Their unwavering love and support has provided a solid foundation for my future and career. In addition, I am thankful for my Grandparents, Don and Marilyn Carn and Barbara Reed, and my Uncle Ron for playing an integral part in my childhood, and now, adult life. I would also like to thank my siblings Katie, Kristopher and Kellie, my sister-in-law Lauren, and soon-to-be brother-in-law Todd for their continued support. A special thank you to my best friends Jeff and Jessica, as they are always there. Thank you, Eric, Bryan, Matt, Joe and Ben for your friendship and companionship for well over a decade and for many decades to come. Thank you to my friends from my undergraduate years, Jared, Erwin, Tom and Paul, that have remained close over the years despite now being hundreds of miles apart. Of course, thank you to my officemates (old and new) Paul, Weiye, Colin, Catalina, Michael and Ilissa for all our great conversations and for patience with my sometimes not-so-productive personality. Finally, I thank my fellow AOSS'ers, Ahmed, Matt, Shannon, Jacob, Dan, Sid, Kristen, Catherine, Gina and Alex for all great times we have had both in and, more importantly, out of the office. Thank you all for your love and support.

This work was partly supported by a Graduate Research Environmental Fellowship from the Office of Biological and Environmental Research within U.S. Department of Energy. Additional support came from the Office of Science, U.S. Department of Energy, Award No. DE-SC0003990. Acknowledgement is also given to the high performance computing support provided by NCAR's Computational and Information Systems Laboratory which is sponsored by the National Science Foundation. Without this support this dissertation would not be possible.

# TABLE OF CONTENTS

# LIST OF FIGURES

**Figure**

# LIST OF TABLES

**Table**

# LIST OF APPENDICES

**Appendix**

# ABSTRACT

An Exploration of Tropical Cyclone Simulations in NCAR's Community Atmosphere Model

by

Kevin A. Reed

Chair: Christiane Jablonowski

Using General Circulation Models (GCMs) for tropical cyclone studies is challenging due to the relatively small size of the storms, the intense convection and a host of scale interactions. However, with the advancement of computer architectures, GCMs are becoming capable of running at high horizontal resolutions with grid spacings of less than 60 km. As a result, high-resolution GCMs are becoming a tool of choice to evaluate tropical cyclones in current and future climate conditions. This raises questions concerning the fidelity of GCMs for tropical cyclone assessments. The physical and dynamical components of GCMs need to be evaluated to assess their reliability for tropical cyclone studies.

An idealized tropical cyclone test case for high-resolution GCMs is developed and implemented in aqua-planet mode with constant sea surface temperatures. The initial conditions are based on an analytic initial vortex seed that is in gradient-wind and hydrostatic balance and intensifies over a 10-day period. The influence of the model parameterization package on the development of the tropical cyclone is assessed. In particular, different physics parameterization suites are investigated within the Na-

tional Center for Atmospheric Research's Community Atmosphere Model CAM, including physics versions 3.1, 4 and 5. The choice of the CAM physics suite has a significant impact on the evolution of the idealized vortex into a tropical cyclone.

In addition, a test case of intermediate complexity is introduced. Therein it is suggested that a GCM dynamical core be paired with simple moist physics to test the evolution of the test vortex. This simple-physics configuration includes important driving mechanisms for tropical cyclones, including surface fluxes, boundary layer diffusion and large-scale condensation. The impact of the CAM dynamical core (the resolved fluid flow component) on the tropical cyclone intensity and size is evaluated. In particular, the finite-volume, spectral element, Eulerian spectral transform and semi-Lagrangian spectral transform dynamical cores are utilized. The simple-physics simulations capture the dominant characteristics of tropical cyclones and are compared to the CAM 5 full physics results for each dynamical core. The research isolates the impact of the physical parameterizations, numerical schemes and uncertainties on the evolution of the cyclone in CAM.

# CHAPTER I

# Introduction: Numerical simulation of tropical cyclones

## 1.1 Why do we model tropical cyclones?

Tropical cyclones are extreme atmospheric vortices that form and develop over the warm tropical oceans, and are among the most remarkable atmospheric phenomena. Depending on the location of formation, tropical cyclones are commonly known by different names. Tropical cyclones are typically referred to as hurricanes in the Western Hemisphere, including the North Atlantic and Eastern Pacific. Furthermore, in the Western Pacific tropical cyclones are called typhoons. In other areas of the globe, such as the Indian Ocean or the Southwestern Pacific they are referred to simply as cyclones or tropical cyclones, respectively.

Tropical cyclones are among the most destructive and lethal geophysical phenomena. In the United States, hurricanes are the costliest of all natural disasters (*Pielke and Landsea*, 1998). According to *Pielke et al.* (2008) the 2004 and 2005 hurricane seasons caused over $150 billion in damages in the United States alone. With the growth of coastal population and property it is expected that hurricane strikes in the future will increase damages significantly (*Pielke et al.*, 2008). Globally, tropical cyclones can also be very deadly. In 1970 a single tropical cyclone that hit Bangladesh

killed nearly half a million people (*Emanuel*, 2003).

Tropical cyclones are an important component of the Earth system, as they transport large amounts of energy and moisture from the tropics towards the poles. However, despite their importance and notoriety as deadly and destructive phenomenon, the physics of tropical cyclones is still not completely understood. There exists uncertainty in the mechanisms of tropical cyclone formation, intensification and decay. In addition, it remains open to question how tropical cyclone characteristics, including intensity, location, frequency and size, will vary under the changing climate conditions of the coming century. Continued modeling and model development provide insight into the uncertainties that still exist in understanding the physics of tropical cyclones. Improving our understanding through tropical cyclone modeling will help the United States and other countries throughout the world better prepare for tropical cyclones now and in the future.

## 1.2 Brief history of numerical simulation of tropical cyclones

Before discussing the techniques for numerical simulation of tropical cyclones that are used today, a brief overview of the numerical simulation of tropical cyclones is provided. The intent is not to provide a detailed history of tropical cyclone modeling, but a basic timeline of significant advances in the scientific community. A more thorough review of the earlier history of the numerical simulation of tropical cyclones is provided by *Anthes* (1982) and *Ooyama* (1982). In addition, *Smith* (2000) covers a detailed history of tropical cyclone modeling as it relates to the development and advances in parameterized convection.

The end of the 1960's marked a time of great advances in parameterized convection and therefore the numerical simulation of tropical cyclones in axisymmetric models. The successful numerical simulation of tropical cyclones starts with the work of *Kuo* (1965) and *Ooyama* (1969) and the effective implementation of convective parame-

terizations. At spatial scales larger than 10 km such parameterizations are required since the scale of convection is too small to be directly simulated in most numerical models. The main objective of convection parameterizations is to specify the amount of water to be condensed and, therefore, the amount of latent heat released in an unsaturated model grid box. These early studies made use of simple axisymmetric models that are often based on the assumption of gradient wind balance. Earlier attempts to represent latent heat release explicitly in tropical cyclone simulations were not successful. Simple axisymmetric models where developed by *Yamasaki* (1965a,b), *Ooyama* (1969), *Rosenthal* (1969) and *Sundqvist* (1965).

While basic evolution and structure of tropical cyclones were reasonably captured by these early simple axisymmetric models, the models are not realistic enough to predict individual tropical cyclones in nature. As a result, models used for the simulation of tropical cyclones became more complex and sophisticated. Perhaps, the most well known, and still commonly used axisymmetric model, is that introduced in *Rotunno and Emanuel* (1987). Such a model contains more advanced microphysics, turbulence, surface fluxes and radiation schemes.

Axisymmetric models suffer from the lack of asymmetry, large-scale storm motion, environmental vertical wind shear and other important mechanisms that affect tropical cyclone formation and development. As a result, the early 1970's witnessed the development and use of three-dimensional limited area models (LAMs) to simulate tropical cyclones. *Anthes et al.* (1971) used a three-dimensional model to simulate an asymmetric hurricane on a constant Coriolis force $f$-plane. This model integrated a three-layer primitive equation model over a uniform grid of 30 km grid spacing in an approximate circular region with a radius of 450 km. Such a model setup simulated some of the features of observed hurricanes, including asymmetries in the storm outflow and cloud bands. However, due to the limitation of the horizontal extent, there was no interaction with the large-scale flow, thus limiting additional realism of

the simulated storms. Similar studies, including *Kurihara and Tuleya* (1974), were also performed on an $f$-plane, but with variable higher-resolution meshes with grid spacings of between 20-100 km. Such studies resulted in an enhanced representation of the tropical cyclone structure.

Further improvement occurred with three-dimensional models with varying Coriolis force on a $\beta$-plane. Such an improvement was the next logical step from $f$-plane modeling studies, and an important step as the Coriolis force is vital in tropical cyclone development. A study by *Mathur* (1974) used a four-level primitive equation numerical model with variable resolution and a larger domain (1760 km by 1760 km). The simulated tropical cyclones developed asymmetries in the pressure, temperature and wind fields. In addition, the model simulated cloud bands and a hurricane eye. Over time, additional enhancements were made to the horizontal and vertical resolutions, parameterizations and numerical schemes to improve the representation of the modeled tropical cyclone, such as those seen in *Madala and Piacsek* (1975).

At the same time when advances were occurring with LAM approaches to simulating tropical cyclones, progress was being made in the modeling of tropical cyclones with global domain models, or general circulation models (GCMs). Simulating tropical cyclones in early generation GCMs presented significant limitations as the resolution was coarser than the resolution of the previous mentioned LAMs and much coarser than today's standards which are in the 25-100 km range. *Manabe et al.* (1970) was the first study to show that a low resolution (roughly 200 km) GCM developed at the Geophysical Fluid Dynamics Laboratory (GFDL) could simulate tropical cyclone-like vortices. The next study using a global model did not occur until the 1980's. *Bengtsson et al.* (1982) used the European Centre for Medium-Range Weather Forecasts (ECMWF) operational model to identify vortices that had similar structure to tropical cyclones. The first study to utilize a GCM to model the climatology of tropical cyclones was produced by *Broccoli and Manabe* (1990). The

study consisted of experiments at two horizontal resolutions of 500 km and 200 km. A reasonable global climatology of storm formation was simulated when compared to observed global climatology, however the regional distribution lacked skill. The *Broccoli and Manabe* (1990) study was also the first to perform an experiment with increased greenhouse gas concentrations in an attempt to quantify how tropical cyclones may change with climate change. Once these studies demonstrated the potential of GCMs to simulate hurricanes numerous studies followed. These are summarized in *Walsh* (2008).

The numerical simulation of tropical cyclones has developed into a very diverse research community with many scientist and modeling groups employing various models for experiments. All of the techniques used to model tropical cyclones discussed above, including axisymmetric models, LAMs and GCMs, were initiated in the late 1960's and early 1970's. Over the later part of the century these techniques were improved with enhanced numerics, physical parameterization, resolution and, of course, knowledge. While some techniques evolved quicker than others, all forms of models are still utilized in more sophisticated forms today.

## 1.3 Current state of numerical simulation of tropical cyclones

Today, tropical cyclone research is a large and diverse field, and tropical cyclone modeling represents a significant component. As evident from the history of the numerical simulation of tropical cyclones, there are three main types of models currently used for hurricane research. The hierarchy of models in order of increasing complexity are axisymmetric models, LAMs and full GCMs. Each of these model genres provides a significant contribution to the tropical cyclone community and our understanding of the formation, development and decay of these storms. Here, we provide detailed descriptions of current work performed with each of the three model techniques.

### 1.3.1 Axisymmetric models

Historically, axisymmetric models have played an integral role in the tropical cyclone community. While such models are typically of the lowest complexity and more idealized among the classes of models used for the tropical cyclone simulations, they offer valuable insight into fundamental storm dynamics. Similarly, axisymmetric models are used for process studies of resolution, physical interactions and numerous other aspects of tropical cyclone simulation. Axisymmetric models often utilize the assumption that tropical cyclones, in their mature form, are in gradient wind balance (the balance of Coriolis, centrifugal and pressure gradient forces). In addition, axisymmetric models are often initialized using a weak, balanced vortex that develops into a tropical cyclone over the course of a few simulation days. In general, these models are run at resolutions on the order of kilometers or smaller, and use prescribed boundary conditions as well as prescribed sea surface temperatures (SST). Examples of axisymmetric modeling studies are *Rotunno and Emanuel* (1987), *Nolan et al.* (2001), *Persing and Montgomery* (2003), *Bryan and Rotunno* (2009a,b).

### 1.3.2 Limited-area models (LAM)

Limited-area models are commonly used for the simulation of tropical cyclones. The three-dimensionality of LAMs allows for more realistic simulations of tropical cyclones as they permit storm motion, large-scale flow interaction and asymmetries. LAMs require that the domain boundaries be forced by either larger domain models, observational data or idealized conditions. The application of LAMs for tropical cyclone modeling is two fold and includes both short-term, deterministic simulations and longer-term climate simulations.

#### 1.3.2.1 Deterministic studies

Limited-area models such as the non-hydrostatic Weather Research and Forecasting Model (WRF, *Skamarock et al.* (2008)) are used operationally to predict the intensity and track of developing tropical cyclones during Atlantic hurricane and Pacific typhoon seasons. Similarly, limited-area models used for tropical cyclone studies are the Pennsylvania State University-NCAR Mesoscale Model (MM5, *Dudhia* (1993)) and the GFDL Hurricane Prediction System (*Kurihara et al.*, 1998). In addition, LAMs are often utilized to investigate the characteristics, including strength, development, track and decay, of individual cyclones retrospectively. In these configurations the LAM is typically used at 1-10 km-spacing resolutions over a period of a few days. Both LAM setups initiate the simulation with data-assimilated initial fields. At times these initial fields are modified to enhance the tropical cyclone's initial representation by including a bogus vortex (e.g. see *Kwon and Cheong* (2010) and *Wang et al.* (2008)). In addition to boundary conditions, LAMs are also driven by prescribed SSTs. Typically the model results are compared to observations as a measure of realism and skill. Recent examples of such LAM studies are *Nolan et al.* (2009), *Wang and Xu* (2010) and *Abarca and Corbosiero* (2011).

Limited-area models are also utilized for idealized studies of tropical cyclones. In these assessments LAMs, like WRF, are configured with artificial (i.e. simplified) initial fields and boundary conditions. The idealized approaches are useful for process studies that isolate dynamical features and environmental impacts (such as the influence of the Coriolis force, vertical wind shear or large-scale flow). In addition, the idealized studies are used to test enhancements in physical parameterization, grid resolution and dynamics-physics coupling. Therefore, the process study approaches used in idealized assessments improve the understanding of the triggers and evolution of tropical cyclones, as well as aid in the advancement of limited-area models. Idealized studies recently performed with WRF include, but are not limited to, those by

*Nolan* (2007), *Nolan et al.* (2007), *Nolan and Rappin* (2008) and *Hill and Lackmann* (2009a,b).

#### 1.3.2.2 Climatology studies

In addition to deterministic simulations, limited-area models have also been used for the simulation of longer-term decadal projections of tropical cyclone statistics, such as regions of formation, tracks and intensities, in a changing climate. These studies often use coarser grid spacings on the order of 20 km when compared to the deterministic studies, mainly a result of computation constraints. In climatology assessments the lower boundary conditions are forced by climatological SSTs with seasonal variations. The climatological SSTs are overlaid by a prescribed trend of increasing SSTs for climate change studies, in addition to trends in greenhouse gases such as carbon dioxide. Examples of experiments that use limited-area models with prescribed SSTs to investigate cyclone statistics for the North Atlantic are *Knutson et al.* (2008) and *Bender et al.* (2010). For climatology studies, the large-scale atmospheric conditions at the domain boundary, such as temperature, wind speed and water vapor, are often derived from climatologies of a low resolution coupled GCM or from reanalysis data. Additional studies such as *Knutson et al.* (2001), *Knutson and Tuleya* (2004) and *Walsh et al.* (2004) utilize coupled-atmosphere-ocean limited-area model simulations.

### 1.3.3 General circulation models (GCM)

While the use of limited-area models to simulate tropical cyclones is well established, the adaptation of GCMs for the use of simulating tropical cyclones has been limited by horizontal and vertical resolution and computational demand. GCMs have become a popular choice for hurricane studies because they eliminate the need for the forced domain boundaries required of limited-area models. Such domain boundaries

are often forced with one-way interaction and, as a result, the forcing has a strong impact on the climatological and atmospheric state within the limited-area model. This forcing raises credibility concerns of the long-term tropical cyclone statistics and climate within these models. In addition, advancements in computer architectures and high-resolution GCMs over the past decade have started to alleviate resolution restrictions. As a result, high-resolution GCMs, with grid spacings in the 10-60 km range, are becoming a tool of choice to evaluate tropical cyclones in current and future climate conditions. The majority of high-resolution GCM model simulations of tropical cyclones have been performed over the past five years, such as the results in this thesis. However, even high-resolution GCMs still face many challenges, including the relatively small size of the tropical storms, the representation of the intense convection and the interaction of large-scale and small-scale processes. Similar to limited-area approaches, GCM studies can also take two forms. There are the shorter-term deterministic or seasonal experiments and longer-term climate experiments.

#### 1.3.3.1 Deterministic and Seasonal studies

Some of the earliest short-term hydrostatic hurricane simulations were conducted with the National Aeronautics and Space Administration (NASA) GCM at grid spacings of 28 km and 14 km near the equator by *Atlas et al.* (2005), *Shen et al.* (2006a) and *Shen et al.* (2006b). The simulations demonstrated remarkable skill in capturing the individual tropical cyclone track and, less so, intensity during selected hurricane seasons. A more recent study by *Chen and Lin* (2011), which used the GFDL High-Resolution Atmospheric Model (HiRAM) at resolutions of around 25 km, found a correlation of 0.96 between the observed and model-predicted hurricane counts for the 2000-2010 Atlantic hurricane seasons. These studies started to probe the limits of the hydrostatic regime, which removes the acceleration of the vertical velocity from the system, in GCMs at these resolutions. As grid spacings approach 10 km,

non-hydrostatic GCM configurations are required as motions at this scale can be significantly influenced by large vertical velocities, and their accelerations. GCMs, such as the Nonhydrostatic ICosahedral Atmospheric Model (NICAM), have been tested with cloud-permitting resolutions of roughly 3.5 km (*Satoh et al.*, 2005; *Miura et al.*, 2007; *Fudeyasu et al.*, 2008). These experiments have been simulated on the Japanese *Earth Simulator*, a high-performance computing platform dedicated to the Earth Sciences. Most recently, *Fudeyasu et al.* (2010a) and *Fudeyasu et al.* (2010b) analyzed the multi-scale interactions in the life cycle of a tropical cyclone with NICAM at resolutions of about 7 km.

#### 1.3.3.2 Climatology studies

At slightly coarser resolutions (between 20-60 km) GCMs have become popular for longer-term (10-30 year) climate assessments that investigate the impact of climate change on tropical cyclone statistics. In addition, these studies compare cyclone statistics of simulations of the last two to three decades to observations in order to understand how well GCMs perform at simulating the climatology of tropical cyclones. For climate change experiments the impact of increased carbon dioxide (and other greenhouse gases) and/or increased, prescribed SSTs is investigated. Examples of such studies include *Yoshimura and Sugi* (2005), *Oouchi et al.* (2006), *Zhao et al.* (2009), *Sugi et al.* (2009), *Zhao and Held* (2010), *Yamada et al.* (2010), *Wehner et al.* (2010), *Murakami and Sugi* (2010) and *Held and Zhao* (2011). The tropical cyclone statistics in these studies have led to varying and partly conflicting conclusions. Overall, the trends suggest that tropical cyclones may become more intense in the simulated warmer climate of the GCMs, while the changes in storm frequency remains uncertain. There is concern that GCMs forced by prescribed SSTs do not allow for the oceans to respond to the forcing of the tropical cyclones themselves as argued by *Emanuel* (2010). This issue is eliminated by using coupled atmosphere-ocean GCM

simulations as demonstrated in *Gualdi et al.* (2008) and *Scoccimarro et al.* (2011). Recently, downscaling techniques have been developed to deduce tropical cyclone activity from GCMs and global reanalyses, and have shown good agreement with observations (*Emanuel*, 2010; *Emanuel et al.*, 2010)

There have also been attempts to complete multi-model ensemble assessments which investigate the impact of climate change on tropical cyclones using GCMs. Ongoing assessments have been a part of the Intergovernmental Panel on Climate Change (IPCC) reports that highlight the potential of recent GCMs to model tropical cyclones (*Randall et al.*, 2007), as well as the World Meteorological Organization (WMO) through the International Workshops on Tropical Cyclones (http://www.wmo.int/pages/prog/arep/wwrp/tmr/IWTC-VII.html). In January 2011, the United States Climate Variability and Predictability Research Program (CLIVAR) initiated a Hurricane Working Group to improve understanding of interannual variability and the impact of a warming climate on tropical activity (see: http://www.usclivar.org/hurricanewg.php). Such a working group is a novel approach that combines GCM results for specified experiments from over twelve different GCM modeling projects around the world. The Hurricane Working Group is an example of future multi-model ensemble approaches using high-resolution GCMs that will lead to a better understanding of tropical cyclones and how the storms might change under a changing climate.

## 1.4 Future modeling trends

While much progress has been made over the past 50 years in the modeling of tropical cyclones, there are still significant opportunities for improvement. This is especially true of GCM studies, where there are still large deficiencies in vertical and horizontal resolution, physical parameterizations, etc. Therefore, this discussion focuses on potential enhancements to GCMs that may improve the representation of

tropical cyclones both in deterministic and climatology assessments. Note that GCMs generally consist of a dynamical core, which incorporate the numerical schemes used for the resolved fluid flow, and the physical parameterizations of the sub-grid scale, unresolved dynamical features. Here, we provide descriptions of the future trends and their relation to tropical cyclone modeling.

### 1.4.1 Scalable quasi-uniform meshes

Advances in computer architectures have led to the need for models, mainly GCMs, to scale to tens of thousands of processors, if not hundreds of thousands. One technique to improve the scalability of models is to replace the typical latitude-longitude mesh with quasi-uniform meshes based on icosahedral (*Sadourny et al.*, 1968; *Williamson*, 1968) or cubed-sphere grids (*Sadourny*, 1972). Such meshes eliminate the so-called "pole problem" which cause computational inefficiency due to small physical grid spacings in the pole regions. The use of quasi-uniform meshes allows for GCMs to be run at finer horizontal resolutions, potentially improving the ability of such models to represent tropical cyclone structure and evolution. It is important to note that at horizontal resolutions of less than 10 km, GCMs need to utilize the non-hydrostatic equations as the hydrostatic approximation is no longer valid. Examples of GCMs that utilize icosahedral, or geodesic, meshes are the NICAM model (*Tomita and Satoh*, 2004), which has shown the ability to simulate tropical cyclones, and the Icosahedral Non-hydrostatic (ICON) GCM (*Wan*, 2009). The GFDL finite–volume cubed-sphere model (*Putman and Lin*, 2007, 2009) has been used to conduct tropical cyclone climate change experiments (*Zhao et al.*, 2009). This thesis will also investigate the capability of the next-generation cubed-sphere spectral element (SE) model (*Fournier et al.*, 2004; *Thomas and Loft*, 2005; *Taylor et al.*, 2007, 2008; *Taylor and Fournier*, 2010; *Taylor*, 2011) available in NCAR's CAM 5, to model tropical cyclones.

### 1.4.2 Mesh refinement

In addition to advances in quasi-uniform meshes, progress has also been made in the area of mesh refinement within GCMs. Mesh refinement techniques allow for improved resolution in limited regions of the global domain. In addition, the areas of mesh refinement can be tailored to the research problem and, therefore, offers an attractive approach to simulating tropical cyclones in GCMs. These can reduce the errors of fine-scale features, such a hurricanes, that result from insufficient resolution and reduce the computational burden of small-scale events. There are two types of mesh refinement used in models. Static mesh refinement refers to the technique in which the area with improved resolution does not change in time. Dynamic mesh refinement, or adaptive mesh refinement (AMR), allows the fine-resolution grid to change during the simulation. The potential advantage of the use of mesh refinement for regional atmospheric modeling has been discussed for decades (see *Fox-Rabinovitz et al.* (1997) for an overview). Recently, mesh refinement techniques have been included operationally in GCMs. An example of such an approach is *Jablonowski et al.* (2009). Similarly, GCMs in current development support mesh refinement such as the Model for Prediction Across Scales (MPAS) (*Skamarock et al.*, 2010) and the SE model available in NCAR's CAM 5, discussed in Section 1.4.1.

### 1.4.3 Scale-aware physical parameterizations

As the mesh of GCMs advances so must the parameterizations of the sub-grid scale processes, which include convection, clouds, radiation, turbulence, etc. As the model resolution increases the sub-grid scale processes that need to be parameterized for weather and climate simulation also change. In addition, variable resolution models, such as those that use mesh refinement, provide a unique problem in that the scales vary throughout the model domain. As a result, there is a need for scale-aware physical parameterizations to be used in future models. The need for unified param-

eterizations that are valid at all temporal and spatial resolutions is now currently being discussed in the scientific and GCM community (*Arakawa et al.*, 2011). This is particularly important for tropical cyclone simulations as the development of these storms depends on physical processes that need to be parameterized in such models. The development of scale-aware parameterizations is a new and developing research field, and only a small amount of work has been performed (*Chen et al.*, 2011). The long-term success of high-resolution and variable-resolution GCMs will depend upon the development of new, scale-aware parameterizations.

## 1.5 Overview of thesis

The goal of this thesis is to test the ability of NCAR's Community Atmosphere Model CAM in varying configurations to simulate tropical cyclones at high resolutions. A novel technique is used to initiate the GCM for a series of process studies that test the fidelity of the model's numerical schemes, physical parameterizations and horizontal resolution for the simulation of tropical cyclones. The thesis is organized as follows.

Chapter II discusses the design of idealized tropical cyclone experiments in GCMs. The evolution of an initially weak, warm-core vortex is investigated over a 10-day time period with varying initial conditions that include variations of the maximum wind speed and radius of maximum wind. The initialization of the vortex is built upon prescribed 3D moisture, pressure, temperature and velocity fields that are embedded in tropical environmental conditions. The initial fields are in exact hydrostatic and gradient-wind balance in an axisymmetric form. The formulation is then generalized to provide analytic initial conditions for an approximately-balanced vortex in GCMs with height-based vertical coordinates. An extension for global models with pressure-based vertical coordinates is presented. The analytic initialization technique can easily be implemented on any GCM computational grid.

The characteristics of the idealized tropical cyclone experiments are illustrated in high-resolution model simulations with CAM version 3.1. The finite–volume dynamical core in CAM 3.1 with 26 vertical levels is used, and utilizes an aqua-planet configuration with constant sea surface temperatures of 29°C. The impact of varying initial conditions and horizontal resolutions on the evolution of the tropical cyclone-like vortex is investigated. Identical physical parameterizations with a constant parameter set are used at all horizontal resolutions. It is suggested that the vortex initialization technique can be used as an idealized tool to study the impact of varying resolutions, physical parameterizations and numerical schemes on the simulation and representation of tropical cyclone-like vortices in global atmospheric models.

The impact of the physical parameterization suite on the evolution of an idealized tropical cyclone within CAM is explored in Chapter III. The CAM versions 3.1 and 4 are used to study the development of the idealized vortex introduced in Chapter II. The main distinction between CAM 3.1 and CAM 4 lies within the physical parameterization of deep convection. CAM 4 includes a dilute plume Convective Available Potential Energy (CAPE) calculation and Convective Momentum Transport (CMT). The finite–volume dynamical core with 26 vertical levels in aqua-planet mode is used at horizontal grid spacings of 1.0°, 0.5° and 0.25°.

Chapter IV analyzes the impact of the initial-data, parameter and structural model uncertainty on the simulation of the idealized vortex in CAM. A total of 78 ensemble simulations are performed at horizontal grid spacings of 1.0°, 0.5° and 0.25° using two versions of the model, CAM 4 and CAM 5. The ensemble members represent simulations with random small-amplitude perturbations of the initial conditions, small shifts in the longitudinal position of the initial vortex and run with slightly altered model parameters. The main distinction between CAM 4 and CAM 5 lies within the physical parameterization suite, and the simulations using both CAM versions at the varying resolutions assess the structural model uncertainty.

The ability of the NCAR's CAM 5 with the spectral element (SE) dynamical core to simulate tropical cyclones is investigated in Chapter V. CAM 5 SE successfully simulates tropical cyclones from the initial idealized vortex at the grid spacings of roughly 111 km, 55 km and 28 km near the equator. The sensitivity to these resolutions and initial uncertainty are tested. Additional simulations test the behavior of the physics parameterizations with small time steps.

Chapter VI introduces a moist, deterministic test case of intermediate complexity for atmospheric general circulation models (AGCMs). We suggest pairing an AGCM dynamical core with simple physical parameterizations to test the evolution of a single, idealized, initially weak vortex into a tropical cyclone. The initial conditions are based on those introduced in Chapter II. The suggested "simple-physics" package consists of parameterizations of bulk aerodynamic surface fluxes for moisture, sensible heat and momentum, boundary layer diffusion, and large-scale condensation. Such a configuration includes the important driving mechanisms for tropical cyclones, and leads to a rapid intensification of the initial vortex over a forecast period of ten days. The simple-physics test paradigm is not limited to tropical cyclones, and can be universally applied to other flow fields. The physical parameterizations are described in detail to foster model intercomparisons. The characteristics of the intermediate-complexity test case are demonstrated with the help of four hydrostatic dynamical cores that are part of the CAM 5 developed at the National Center for Atmospheric Research (NCAR). In particular, these are the finite-volume, spectral element, and spectral transform Eulerian and semi-Lagrangian dynamical cores that are coupled to the simple-physics suite.

The thesis ends with a summary of the major accomplishments in Chapter VII. In addition, there is a discussion of potential future research projects.

# CHAPTER II

# An analytic vortex initialization technique for idealized tropical cyclone studies in AGCMs

## 2.1 Introduction

Numerical modeling of tropical cyclones in general circulation models (GCMs) presents several challenges, including the relatively small size of the storms, intense convection and the interaction of large-scale and small-scale processes. A typical tropical cyclone has a radius of maximum wind (RMW) on the order of 10–100 km (*Emanuel*, 2003), which is mostly unresolved at typical climate model resolutions of about 100–200 km. Despite this limitation, early GCM studies since the 80's and early 90's have succeeded in simulating tropical low pressure systems that have many tropical cyclone-like characteristics, such as a warm-core structure and realistic regions of formation. These findings are summarized in *Walsh* (2008) who also provides an overview of the current state-of-the-art of tropical cyclone modeling with climate models.

Tropical cyclone modeling in GCMs is a lively research field since modern computing architectures now allow very high horizontal resolutions that even approach the transition to non-hydrostatic scales. In particular, over the last five years numerous studies have discussed the generation and development of tropical cyclones

with a variety of high-resolution GCMs. For example, *Atlas et al.* (2005) and *Shen et al.* (2006a,b) demonstrated the ability of NASA's hydrostatic finite-volume GCM to simulate tropical cyclones successfully at horizontal resolutions of 0.25° and 0.125°, or 28 km and 14 km in equatorial regions, respectively. Another example is the study by *Oouchi et al.* (2006) who used a 20 km high-resolution global atmospheric model developed by the Meteorological Research Institute and Japan Meteorological Agency (MRI/JMA). They simulated the frequency, distribution and intensity of tropical cyclones in the current climate, and despite some shortcomings the model was successful in reproducing the overall geographical distribution and frequency of tropical storms. However, similar to *Shen et al.* (2006b), *Oouchi et al.* (2006) had difficulty simulating the maximum intensity, suggesting that even higher resolutions may be required to simulate both tropical cyclone tracks and intensity accurately. Other recent investigations include the studies by *Bengtsson et al.* (2007) and *Zhao et al.* (2009), who evaluated tropical cyclone statistics in the Max-Planck Institute for Meteorology ECHAM-5 model at the spectral resolution T319 (approx. 42 km) and in the Atmospheric Model AM2.1 by the Geophysical Fluid Dynamics Laboratory on a 0.5° grid, respectively. The research shows that GCMs have developed an increasingly sophisticated ability to simulate tropical cyclones. This is further supported by the tropical cyclone assessments in the latest Intergovernmental Panel on Climate Change (IPCC) report that highlights the potential of recent GCMs to model tropical cyclones (*Randall et al.*, 2007). Most recently, global cloud resolving models, such as the Nonhydrostatic ICosahedral Atmospheric Model (NICAM), have shown enhanced skill in the simulation of real and projected future tropical cyclone activity (*Fudeyasu et al.*, 2008; *Yamada et al.*, 2010).

A number of recent studies have used simplified models to understand the factors that influence tropical cyclogenesis and rapid intensification. For example, *Nolan* (2007) used the Weather Research and Forecast Model (WRF) developed at the

National Center for Atmospheric Research (NCAR) at a grid spacing of 6 km with a 2 km nested grid to investigate the development and structure of tropical cyclones on a constant $f$-plane. The model simulations started from prescribed initial conditions that favor cyclogenesis. In particular, the initial conditions were based on a tropical sounding with no mean wind and no wind shear, and the sea surface temperature (SST) was held constant at 29°C. In addition, *Nolan et al.* (2007) and *Nolan and Rappin* (2008) used WRF at high-resolutions (4 km) to investigate the impact of environmental variables, such as the SST, Coriolis parameter, mean surface wind and wind shear on the evolution and intensification of a pre-existing, weak, warm-core vortex into a tropical cyclone on an $f$-plane. Similarly, *Hill and Lackmann* (2009a) studied the development of an initial vortex in hydrostatic and gradient-wind balance in a warm moist environment to investigate the impact of the grid spacing, turbulence parameterizations and surface layer fluxes in WRF. Such investigations have been very successful in simulating the development from an initially-weak vortex to a hurricane-strength tropical cyclone, and shed light on cyclogenesis processes and the cyclone structure. The findings suggest that the lessons learned in idealized simulations are also relevant and applicable to real conditions. The idealized simulations are thereby a modeling tool that allow for further studies with respect to the horizontal and vertical model resolutions, physics parameterizations and even the choice of the GCM dynamical core.

Inspired by the success of tropical cyclone simulations in regional models like WRF, we show that similar evolutions of an initially weak vortex into a tropical cyclone-like vortex can also be simulated in high-resolution GCMs that employ grid spacings of 0.5° and finer. This paper describes the design of the suggested initial conditions, the chosen aqua-planet setup of the GCM with constant SSTs and sensitivity tests. The first goal of this paper is to introduce a set of analytic initial conditions to initialize a weak, warm-core vortex in an aqua-planet configuration of

NCAR's Community Atmosphere Model CAM 3.1 at high horizontal resolutions. The second goal is to exemplify the use of the analytic initial conditions by exploring the sensitivity of GCM simulations to varying initial conditions that include variations of the maximum wind speed and radius of maximum wind. From such sensitivity tests a control case is determined that simulates the development of the initial vortex into an intense tropical cyclone-like vortex. The control case can then be used to explore the model sensitivity to horizontal resolution. In general, the hope is that increased resolutions in GCMs in combination with adequate physical parameterizations will improve future climate simulations to a point that they can be reliably used to study the impact of changing climatic conditions on tropical cyclone statistics.

The paper is organized as follows. Section 2.2 discusses the design of the analytic initial conditions for the idealized tropical cyclone experiments. The initial setup comprises tropical environmental conditions with an embedded vortex in hydrostatic and axisymmetric gradient-wind balance. Section 2.3 provides a brief description of the NCAR model CAM 3.1. Section 2.4 reviews the results of the simulations in aqua-planet mode with different initial conditions for two different model resolutions of 0.5° and 0.25°. The identified control case is then used in Section 2.5 to assess the evolution of the highly-energetic idealized cyclone at the four horizontal resolutions 1.0°, 0.5°, 0.25° and 0.125°. This includes a discussion of the simulated convective and large-scale precipitation, moisture, temperature and vertical velocity fields. The conclusions and summary are provided in Section 2.6, as well as an outline of future work.

## 2.2 Idealized initial conditions

The first goal is to define an analytic set of idealized initial conditions that favor the development of tropical cyclone-like vortices in GCMs over the course of ten simulation days. Our initialization technique differs from traditional bogussing tech-

niques, as for example described in *Leslie and Holland* (1995) or *Wang et al.* (2008), since we prescribe analytic functions for the initial data that can readily be evaluated on any computational grid. The section is organized as follows. First, the 1D vertical profiles of the background temperature, moisture and pressure conditions are introduced. Second, we use an axisymmetric approach to define a vortex in hydrostatic and gradient-wind balance. Third, we project the axisymmetric conditions onto the spherical domain for height-based vertical coordinate systems, and fourth, we generalize the formulation for pressure-based vertical coordinates that are most often used in GCMs today. The latter part involves simple fixed-point iterations that can also be applied to isentropic vertical coordinates (see Appendix of *Jablonowski and Williamson* (2006a)). All parameters and physical constants used in the derivation are listed in Table 2.1.

### 2.2.1 1D vertical profiles for the background conditions

The first step is to provide analytic background moisture and virtual temperature profiles that fit the observed tropical soundings by *Jordan* (1958). The analytic form of the background specific humidity profile $\bar{q}(z)$ as a function of height $z$ is specified as

$$\begin{aligned} \bar{q}(z) &= q_0 \exp\left(-\tfrac{z}{z_{q1}}\right) \exp\left(-\left(\tfrac{z}{z_{q2}}\right)^2\right) \quad \text{for } 0 \le z \le z_t, \\ \bar{q}(z) &= q_t \qquad\qquad\qquad\qquad\qquad\qquad\quad \text{for } z_t < z, \end{aligned} \tag{2.1}$$

where $z_t = 15$ km approximates the tropopause height as seen in the *Jordan* (1958) sounding, $q_0$ is the specific humidity at the surface ($z = 0$ m), which is taken to be 21 g kg$^{-1}$, and $q_t$ is the specific humidity in the upper atmosphere set to a constant value of $10^{-8}$ g kg$^{-1}$. The specific humidity $q_0$ was chosen to match the value of the relative humidity at the surface from the *Jordan* (1958) sounding, using a surface temperature of $T_0 = 302.15$ K or 29°C. It ensures that the surface temperature matches the SST of 302.15 K. The constant $z_{q1}$ determines the rate of decrease of the specific humidity

Table 2.1: List of parameters and physical constants. The values that are varied in this study are $\Delta p$, $r_p$ and $q_0$.

| Parameter | Description | Control Value |
|---|---|---|
| $a$ | Radius of Earth | $6.37122 \times 10^6$ m |
| $\Omega$ | Rotational speed of Earth | $7.292115 \times 10^{-5}$ s$^{-1}$ |
| $R_d$ | Gas constant for dry air | 287.04 J kg$^{-1}$ K$^{-1}$ |
| $g$ | Gravity | 9.80616 m s$^{-2}$ |
| $z_t$ | Tropopause height | 15000 m |
| $q_0$ | Specific humidity at the surface | 21 g kg$^{-1}$ |
| $q_t$ | Specific humidity of upper atmosphere | $10^{-8}$ g kg$^{-1}$ |
| $z_{q1}$ | Constant for specific humidity profile | 3000 m |
| $z_{q2}$ | Constant for specific humidity profile | 8000 m |
| $T_0$ | Surface temperature and sea surface temperature | 302.15 K |
| $T_{v0}$ | Background virtual temperature at the surface | $T_0(1 + 0.608\, q_0)$ |
| $T_{vt}$ | Virtual temperature in upper atmosphere | $T_{v0} - \Gamma z_t$ |
| $\Gamma$ | Virtual temperature lapse rate | 0.007 K m$^{-1}$ |
| $p_0$ | Background surface pressure | 1015 hPa |
| $p_t$ | Pressure at the tropopause height $z_t$ | See Eq. (2.5) |
| $\Delta p$ | Surface pressure difference between the background and center | 11.15 hPa |
| $r_p$ | Constant for pressure fit | 282 km |
| $z_p$ | Constant for pressure fit | 7000 m |
| $\varphi_c$ | Center latitude of initial vortex | 10°N |
| $\lambda_c$ | Center longitude of the initial vortex | 180°E |
| $f_c$ | Coriolis parameter | $2\Omega \sin(\varphi_c)$ |
| $\epsilon$ | Small constant to avoid division by zero | $10^{-25}$ |
| $\varepsilon$ | Convergence limit for fixed-point iterations | $2 \times 10^{-13}$ |

with height and is set to 3000 m. In addition, the constant $z_{q2}$ is set to 8000 m to quickly nudge the specific humidity profile towards zero in the higher troposphere.

The analytic background virtual temperature sounding $\bar{T}_v(z)$ is split into two different representations for the lower and upper atmosphere. The virtual temperature profile is given by

$$\begin{aligned} \bar{T}_v(z) &= T_{v0} - \Gamma z \quad \text{for } 0 \leq z \leq z_t, \\ \bar{T}_v(z) &= T_{vt} \qquad\quad \text{for } z_t < z, \end{aligned} \tag{2.2}$$

with the virtual temperature at the surface $T_{v0} = T_0(1 + 0.608\, q_0)$ (approximately 306 K). The virtual temperature lapse rate $\Gamma$ is set to 0.007 K m$^{-1}$. It approximates the observed sounding from *Jordan* (1958) and is similar to the average lapse rate in the troposphere. Such a lapse rate provides conditionally unstable conditions in the troposphere. For simplicity, the virtual temperature in the upper atmosphere is set to the constant $T_{vt} = T_{v0} - \Gamma z_t$ (approximately 201 K), which equals the virtual temperature at the tropopause height. As a result, the background temperature profile $\bar{T}(z)$ is

$$\bar{T}(z) = \frac{\bar{T}_v(z)}{1 + 0.608\bar{q}(z)}. \tag{2.3}$$

The analytic background vertical profiles of the temperature, specific humidity and relative humidity are depicted in Fig. 2.1, along with a comparison to the soundings of *Jordan* (1958). The specific humidity values correspond to relative humidities of about 80% at lower levels and prescribe a warm and moist environment.

The background pressure profile $\bar{p}(z)$ is computed using the hydrostatic equation and ideal gas law. Note that the virtual temperature must be used in this calculation. As before, the background pressure profile has different representations in the lower

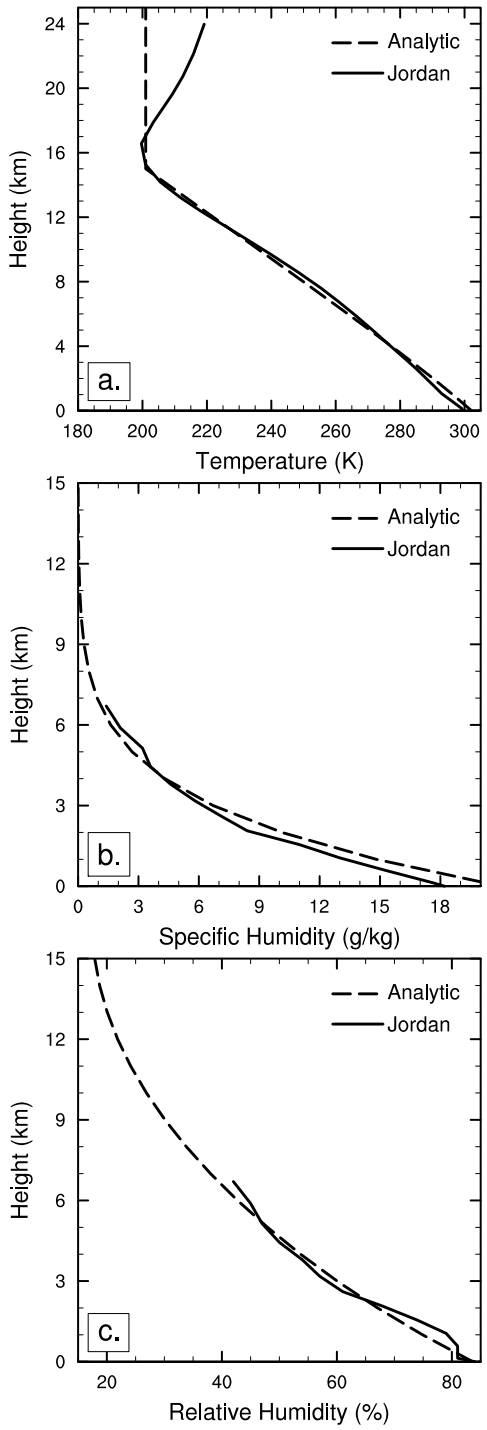


Figure 2.1: Comparison of the analytic vertical profiles to the observed *Jordan* (1958) mean hurricane season soundings of (a) temperature, (b) specific humidity and (c) relative humidity.

and upper atmosphere

$$\begin{aligned} \bar{p}(z) &= p_0 \left(\frac{T_{v0}-\Gamma z}{T_{v0}}\right)^{\frac{g}{R_d\Gamma}} && \text{for } 0 \leq z \leq z_t, \\ \bar{p}(z) &= p_t \exp\left(-\left(\frac{g(z-z_t)}{R_d T_{vt}}\right)\right) && \text{for } z_t < z, \end{aligned} \tag{2.4}$$

where $p_0 = 1015$ hPa is the background surface pressure, $R_d = 287.04$ J kg$^{-1}$ K$^{-1}$ is the ideal gas constant for dry air and $g = 9.80616$ m s$^{-2}$ is the gravity. The pressure at the tropopause level $z_t$ is continuous and given by

$$p_t = p_0 \left(\frac{T_{vt}}{T_{v0}}\right)^{\frac{g}{R_d\Gamma}}, \tag{2.5}$$

which is approximately 130.5 hPa.

### 2.2.2 2D axisymmetric vortex

The formulation of the 2D axisymmetric pressure field is inspired by an offline axisymmetric model, originally described in *Nolan et al.* (2001) and *Nolan* (2007). Here, we fit analytic functions to the pressure field from a similar offline model, which allows us to derive all other fields analytically. The fitted pressure equation $p(r, z)$ is comprised of a background pressure profile $\bar{p}(z)$ (Eq. (2.4)) plus a 2D pressure perturbation $p'(r, z)$ where $r$ symbolizes the radial distance (or radius) to the center of the prescribed vortex. The chosen center position is further explained in Section 2.2.3 and also listed in Table 2.1. The pressure is expressed as

$$p(r, z) = \bar{p}(z) + p'(r, z) \tag{2.6}$$

with

$$\begin{aligned} p'(r,z) &= -\Delta p \, \exp\left(-\left(\frac{r}{r_p}\right)^{3/2}\right) \exp\left(-\left(\frac{z}{z_p}\right)^{2}\right) \left(\frac{T_{v0}-\Gamma z}{T_{v0}}\right)^{\frac{g}{R_d\Gamma}} && \text{for } 0 \le z \le z_t, \\ p'(r,z) &= 0 && \text{for } z_t < z. \end{aligned} \tag{2.7}$$

The pressure perturbation depends on the pressure difference $\Delta p$ between the background surface pressure $p_0$ and the pressure at the center of the initial vortex, and is chosen to decay exponentially in radius and height. $r_p$ determines the pressure change in the radial direction and $z_p = 7$ km precribes how fast the pressure difference decays in height within the vortex. The pressure perturbation becomes negligible in the upper atmosphere and is set to zero above $z_t$. Both $\Delta p$ and $r_p$ determine the initial maximum wind and the initial RMW. The values are specified in Section 2.4 for a variety of initial conditions.

Using Eqs. (2.4), (2.6) and (2.7) we can represent the axisymmetric pressure field as

$$\begin{aligned} p(r,z) &= \left[p_0 - \Delta p \, \exp\left(-\left(\frac{r}{r_p}\right)^{3/2}\right) \exp\left(-\left(\frac{z}{z_p}\right)^{2}\right)\right] \left(\frac{T_{v0}-\Gamma z}{T_{v0}}\right)^{\frac{g}{R_d\Gamma}} && \text{for } 0 \le z \le z_t, \\ p(r,z) &= p_t \, \exp\left(-\left(\frac{g(z-z_t)}{R_d T_{vt}}\right)\right) && \text{for } z_t < z. \end{aligned} \tag{2.8}$$

In the limit of large $r$ the expression approaches the background pressure profile $\bar{p}(z)$ as expected. The surface pressure $p_s(r)$ is computed by setting $z = 0$ m in Eq. (2.8), which gives

$$p_s(r) = p_0 - \Delta p \, \exp\left(-\left(\frac{r}{r_p}\right)^{3/2}\right). \tag{2.9}$$

Such a representation of the surface pressure is similar to that derived for mature hurricanes by *Holland* (1980). It describes an idealized vortex with a pressure decrease of $\Delta p$ in its center.

Next, we calculate an analytic function for the axisymmetric virtual temperature $T_v(r,z)$ using the hydrostatic equation and ideal gas law

$$T_v(r,z) \;=\; -\frac{gp(r,z)}{R_d\frac{\partial p(r,z)}{\partial z}}, \tag{2.10}$$

which leads to the expression

$$\begin{aligned} T_v(r,z) &= (T_{v0}-\Gamma z)\left[1+\frac{2R_d(T_{v0}-\Gamma z)z}{gz_p^2\left[1-\frac{p_0}{\Delta p}\exp\left(\left(\frac{r}{r_p}\right)^{3/2}\right)\exp\left(\left(\frac{z}{z_p}\right)^2\right)\right]}\right]^{-1} && \text{for } 0\le z\le z_t, \\ T_v(r,z) &= T_{vt} && \text{for } z_t < z\ . \end{aligned} \tag{2.11}$$

It describes the warm core structure of the initial vortex. The expression for the lower troposphere below $z_t$ approaches the background temperature profile (Eq. (2.2)) in the limit of large $r$, as expected.

The axisymmetric specific humidity $q(r,z)$ is set to the background profile everywhere

$$q(r,z) = \bar{q}(z). \tag{2.12}$$

Therefore, the virtual temperature can simply be converted to the temperature $T(r,z)$, resulting in the following expression

$$\begin{aligned} T(r,z) &= \frac{T_{v0}-\Gamma z}{1+0.608\bar{q}(z)}\left[1+\frac{2R_d(T_{v0}-\Gamma z)z}{gz_p^2\left[1-\frac{p_0}{\Delta p}\exp\left(\left(\frac{r}{r_p}\right)^{3/2}\right)\exp\left(\left(\frac{z}{z_p}\right)^2\right)\right]}\right]^{-1} && \text{for } 0\le z\le z_t, \\ T(r,z) &= T_{vt} && \text{for } z_t < z. \end{aligned} \tag{2.13}$$

Due to the small specific humidity value in the upper atmosphere ($10^{-8}$ g kg$^{-1}$ for $z > z_t$) the virtual temperature equals the temperature to a very good approximation in this region. Eq. (2.13) can also be expressed in the form of the background

temperature $\bar{T}(z)$ (Eq. (2.3)) plus a temperature perturbation $T'(r,z)$

$$T(r,z) = \bar{T}(z) + T'(r,z). \tag{2.14}$$

Then the temperature perturbation is

$$\begin{aligned} T'(r,z) &= \frac{T_{v0}-\Gamma z}{1+0.608\bar{q}(z)} \frac{-2R_d(T_{v0}-\Gamma z)z}{2R_d(T_{v0}-\Gamma z)z+gz_p^2\left[1-\frac{p_0}{\Delta p}\exp\left(\left(\frac{r}{r_p}\right)^{3/2}\right)\exp\left(\left(\frac{z}{z_p}\right)^2\right)\right]} && \text{for } 0 \le z \le z_t, \\ T'(r,z) &= 0 && \text{for } z_t < z. \end{aligned} \tag{2.15}$$

In the limit of large $r$ the temperature perturbation goes to zero.

Figure 2.2 shows the vertical temperature profile of the environmental conditions versus the temperature profile of an insulated parcel of air that is hypothetically lifted from the surface. The profiles are shown both for an environmental (unperturbed) background position and for the center of the vortex. The parcel first follows the dry adiabatic lapse rate. Once the parcel becomes saturated it cools at the moist adiabatic lapse rate and becomes buoyant. Therefore, the initial conditions are unstable for saturated air. The lifting condensation level (LCL) for the background environment is about 380 m and for the center of the vortex is about 400 m.

Finally, the tangential velocity field $v_T(r,z)$ of the axisymmetric vortex is defined by utilizing the gradient-wind balance, which depends on the pressure (Eq. (2.8)) and the virtual temperature (Eq. (2.11)). The tangential velocity is given by

$$v_T(r,z) = -\frac{f_c r}{2} + \sqrt{\frac{f_c^2 r^2}{4} + \frac{R_d\, T_v(r,z)\, r}{p(r,z)} \frac{\partial p(r,z)}{\partial r}}, \tag{2.16}$$

where $f_c = 2\Omega\sin(\varphi_c)$ is the Coriolis parameter at the constant latitude $\varphi_c$ and $\Omega = 7.292115 \times 10^{-5}$ s$^{-1}$ is the rotational speed of the Earth. We set $\varphi_c = \pi/18$ (or 10°N), which is also the center latitude of the vortex for all experiments. Substituting

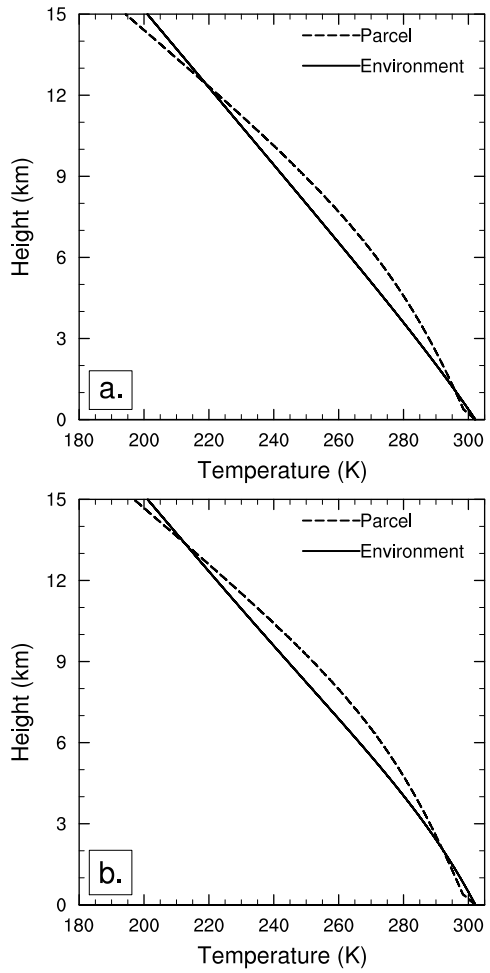


Figure 2.2: Environmental and air parcel temperature profiles for (a) background conditions and (b) in the center of the vortex. The parcel is lifted from the surface.

$T_v(r,z)$ and $p(r,z)$ into Eq. (2.16) gives

$$v_T(r,z) = -\frac{f_c r}{2} + \sqrt{\frac{f_c^2 r^2}{4} - \frac{\frac{3}{2}\left(\frac{r}{r_p}\right)^{3/2}(T_{v0}-\Gamma z)R_d}{1+\frac{2R_d(T_{v0}-\Gamma z)z}{g z_p^2}-\frac{p_0}{\Delta p}\exp\left(\left(\frac{r}{r_p}\right)^{3/2}\right)\exp\left(\left(\frac{z}{z_p}\right)^2\right)}} \quad \text{for } 0 \le z \le z_t,$$

$$v_T(r,z) = 0 \quad \text{for } z_t < z. \tag{2.17}$$

The tangential wind is zero in the upper atmosphere since the pressure no longer depends on the radial distance $r$ above $z_t$. Here, it is evident that the initial maximum wind speed $v_0 = \max|v_T|$ and RMW are dependent on many different parameters, but the only free parameters are $\Delta p$ and $r_p$.

### 2.2.3 3D spherical representation with height-based vertical coordinate

To initialize a global model with the idealized vortex, the axisymmetric fields need to be defined on the GCM grid. Here, we use spherical coordinates where $\lambda$ and $\varphi$ denote the longitudinal and latitudinal positions, respectively. The vertical coordinate is represented by the height above the surface. A coordinate transformation to other representations, such as Cartesian coordinates, is straightforward. We introduce the spherical grid by redefining $r$ to be the great circle distance to the center of the vortex. The great circle distance is given by

$$r = a \arccos\left(\sin\varphi_c \sin\varphi + \cos\varphi_c \cos\varphi \cos\left(\lambda - \lambda_c\right)\right), \tag{2.18}$$

where $a = 6.37122 \times 10^6$ m symbolizes the radius of the earth. The vortex is centered at $(\lambda_c, \varphi_c) = (\pi, \pi/18)$, which corresponds to the position 180°E and 10°N.

The great circle distance replaces $r$ in the equations for the surface pressure (Eq. (2.9)), specific humidity (Eq. (2.12)), temperature (Eq. (2.13)) and the tangential velocity (Eq. (2.17)). The surface geopotential $\Phi_s$ is set to zero. If non-hydrostatic model formulations are employed the vertical velocity needs to be set to zero. As mentioned before, the surface temperature in the background environment is identical to the prescribed SSTs of 29°C.

As a last step, the tangential velocity Eq. (2.17) needs to be split into its zonal and meridional wind components $u(\lambda, \varphi, z)$ and $v(\lambda, \varphi, z)$ in spherical coordinates. Similar to *Nair and Jablonowski* (2008) this is done via the expressions

$$d_1 = \sin\varphi_c \cos\varphi - \cos\varphi_c \sin\varphi \cos(\lambda - \lambda_c) \tag{2.19}$$

$$d_2 = \cos\varphi_c \sin(\lambda - \lambda_c) \tag{2.20}$$

$$d = \max\left(\epsilon, \sqrt{{d_1}^2 + {d_2}^2}\right), \tag{2.21}$$

which are utilized in the projections

$$u(\lambda, \varphi, z) = \frac{v_T[r(\lambda, \varphi), z]\, d_1}{d} \tag{2.22}$$

$$v(\lambda, \varphi, z) = \frac{v_T[r(\lambda, \varphi), z]\, d_2}{d}\,. \tag{2.23}$$

A small $\epsilon = 10^{-25}$ value avoids divisions by zero. The analytic initial conditions can easily be computed on any GCM grid provided the positions $(\lambda, \varphi, z)$ are known. The vortex is well-balanced on the spherical grid, but not in exact balance due to the use of the axisymmetric approach with constant Coriolis parameter. However, the balance is sufficient to foster the evolution of the pre-existing, low-level vortex into an intense tropical cyclone-like vortex over a forecast period of ten days. It provides a suitable basis for the studies of horizontal resolutions as discussed in Sections 2.4 and 2.5.

### 2.2.4 3D spherical representation with pressure-based vertical coordinate

For GCMs that are built upon pressure-based vertical coordinates, such as the $\sigma$-coordinate (*Phillips*, 1957) or the hybrid $\sigma$-pressure so-called $\eta$-coordinate (*Simmons and Burridge*, 1981), the analytic initial conditions can be converted into the pressure-based systems. The conversion is analytic for the background conditions and in the upper atmosphere above $z_t$ but requires straightforward fixed-point iterations in the vortex-covered region. Given the background pressure profile (Eq. (2.4)) where $p_0$ is now generalized to be $p_s$, the conversion between pressure $p$ and height $z$ is given by

$$\begin{aligned} z &= \tfrac{T_{v0}}{\Gamma}\left(1 - \left(\tfrac{p}{p_s}\right)^{\frac{R_d\Gamma}{g}}\right) \quad \text{for } p_s \geq p \geq p_t, \\ z &= z_t + \tfrac{R_d T_{vt}}{g} \ln\left(\tfrac{p_t}{p}\right) \qquad \text{for } p_t > p. \end{aligned} \tag{2.24}$$

The pressure $p$ denotes the vertical pressure position of a GCM grid point, which can be computed via the known surface pressure (Eq. (2.9)) for $\sigma$- or $\eta$-coordinates. The

corresponding $z$-value can now be plugged into the equations for the specific humidity, temperature and horizontal velocities according to Eqs. (2.12), (2.13), (2.22) and (2.23).

Note again that this analytic conversion is not accurate within the vortex due to the pressure perturbation and warm-core structure. Within the vortex the $z$-value at each model level needs to be computed iteratively via Newton's method

$$z^{n+1} = z^n - \frac{F(\lambda, \varphi, z^n)}{\partial F/\partial z(\lambda, \varphi, z^n)}. \tag{2.25}$$

The superscript $n = 0,\ 1,\ 2,\ 3,...$ indicates the iteration count. The function $F$ is determined by

$$F(\lambda, \varphi, z) = p_{model} - p(\lambda, \varphi, z). \tag{2.26}$$

$p_{model}$ is the pressure of the GCM grid point at a given longitude $\lambda$, latitude $\varphi$ and model level, and $p(\lambda, \varphi, z)$ represents Eq. (2.8) evaluated with the great circle distance $r$. Therefore, $\partial F/\partial z$ is defined by

$$\frac{\partial F(\lambda, \varphi, z)}{\partial z} = -\frac{\partial p(\lambda, \varphi, z)}{\partial z}, \tag{2.27}$$

which can be computed analytically from Eq. (2.8). The analytic form of $\partial p/\partial z$ in terms of the great circle distance $r$ is

$$\begin{aligned} \frac{\partial p(r,z)}{\partial z} &= \frac{2\Delta p\, z}{z_p^2} \exp\left(-\left(\frac{r}{r_p}\right)^{3/2}\right) \exp\left(-\left(\frac{z}{z_p}\right)^2\right) \left(\frac{T_{v0} - \Gamma z}{T_{v0}}\right)^{\frac{g}{R_d \Gamma}} \\ &\quad -\frac{g}{R_d T_{v0}} \left[p_0 - \Delta p \exp\left(-\left(\frac{r}{r_p}\right)^{3/2}\right) \exp\left(-\left(\frac{z}{z_p}\right)^2\right)\right] \left(\frac{T_{v0} - \Gamma z}{T_{v0}}\right)^{\frac{g}{R_d \Gamma} - 1}. \end{aligned} \tag{2.28}$$

Eq. (2.25) is iterated until it converges to $|z^{n+1} - z^n|/|z^{n+1}| < \varepsilon$ where $\varepsilon$ is set to 2 $\times\ 10^{-13}$ (close to machine precision for double precision arithmetic). We recommend

starting the iterations with the start value $z^0$ equal to $z$ given in Eq. (2.24). Typically, the computations converge within the $\varepsilon$ precision in under ten iterations. We apply the iterative technique below $z_t$ (equivalent to $p_{model} > p_t$) within a great circle distance of $r \leq 1000$ km from the vortex center. It represents the distance at which the pressure (Eq. (2.7)) and temperature (Eq. (2.15)) perturbations become negligible.

It is possible to initialize the GCM without the iterative method using the background pressure to height conversion (Eq. (2.24)), but this intoduces inaccuracies in the initial temperature and wind fields within the troposphere. We strongly recommend the iterative procedure to foster model intercomparisons between models with height-based and pressure-based vertical coordinates. As demonstrated in Section 2.4, the evolution of the vortex is sensitive to the initial conditions.

### 2.2.5 Characteristics of the initial conditions

Figure 2.3 shows the horizontal cross sections of the initial wind speed at a height of 100 m, the surface pressure and the temperature at 4.35 km. The latter corresponds to the altitude of the maximum (warm-core) temperature perturbation, which is about 3 K. The vortex is computed with the parameters $r_p = 282$ km and $\Delta p = 11.15$ hPa, which leads to a maximum wind speed of $v_0$ of 20 m s$^{-1}$ and an RMW of 250 km. The surface pressure is lowest in the center of the storm with a central pressure of 1003.85 hPa. In addition, the wind is greatest at the RMW and decreases rapidly in magnitude towards the center of the vortex, where the wind is zero. The wind field also decreases at radii larger than RMW and approaches the zero background flow at an approximate distance of about 1200 km from the center.

Figure 2.4 shows longitude-height cross sections of the magnitude of the wind, the pressure perturbation, the temperature perturbation, potential virtual temperature, square of the moist Brunt-Väisälä frequency and the relative vorticity through the center latitude of the vortex. From the vertical cross section of the wind, we see that

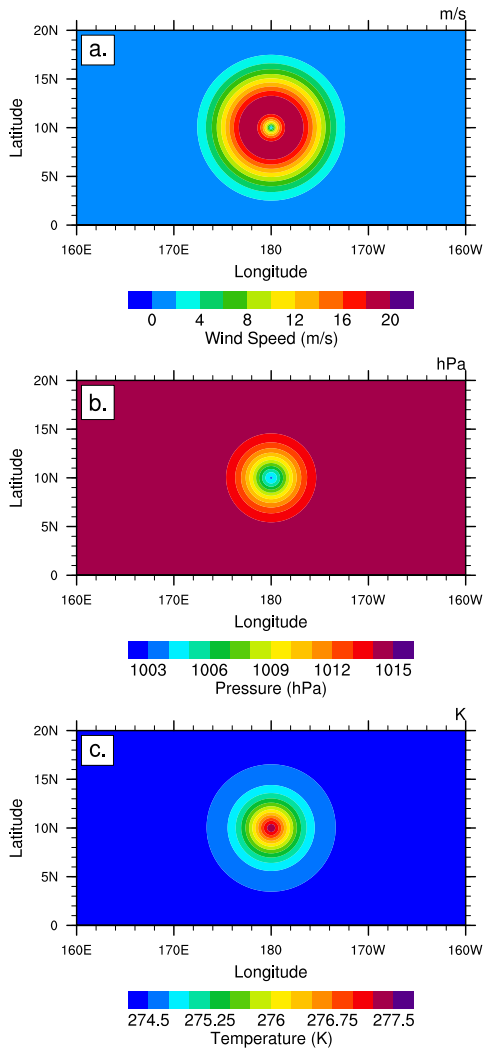


Figure 2.3: Horizontal cross sections of the (a) initial wind speed at a height of 100 m, (b) surface pressure and (c) temperature at a height of 4.35 km. The maximum wind speed is 20 m $s^{-1}$ with an RMW of 250 km.

the wind is greatest at the surface and decays with height. The pressure perturbation is greatest at the surface and center of the vortex and decays with height and radius from the center, as expected from Eq. (2.7). The cross section of the temperature perturbation reiterates that the maximum perturbation occurs at a height of 4.35 km and decreases in magnitude radially and vertically, both below and above the maximum. The plot of the potential virtual temperature and the square of the moist Brunt-Väisälä both show that the initial vortex is stable to unsaturated air, but as indicated earlier in Fig. 2.2 is conditionally unstable with a lifting condensation level

between 380 and 400 m throughout the vortex. The vorticity cross section displays that the maximum vorticity occurs at the center and decays radially and vertically until it reaches a minimum approximately 5° west and east of the center.

The maximum potential intensity (MPI) based on the theory of *Emanuel* (1986) is approximately 66 m $s^{-1}$ for this environmental sounding. The MPI is calculated using the surface temperature of 29°C, or 302.15 K, assuming that the outflow temperature is equal to the tropopause temperature of 201 K, and that the ambient boundary layer relative humidity is 80 %. In addition, the ratio of the boundary layer exchange coefficients $C_k/C_D$ is taken to be 1, $r_0 = 1200$ km, $p_a = 1015$ hPa and $f = 2\Omega \sin(\varphi_c)$ (for definitions of these variables see *Emanuel* (1986)). During the simulation the ratio $C_k/C_D$ fluctuates. Therefore, our assumption that $C_k/C_D$ is 1 is an approximation that contributes uncertainty to the MPI estimate.

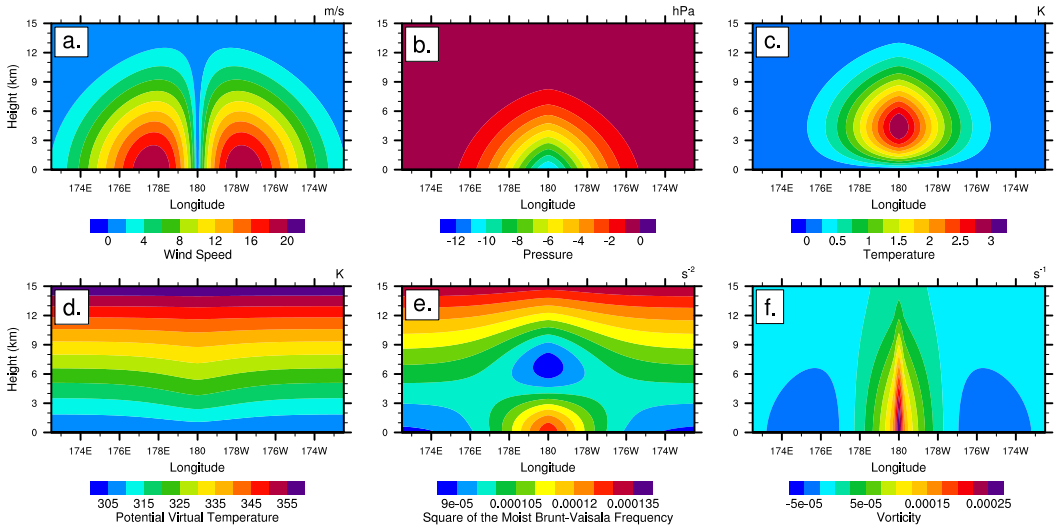


Figure 2.4: Initial longitude-height cross sections of the (a) wind speed, (b) pressure perturbation $p'$, (c) temperature perturbation $T'$, (d) potential virtual temperature, (e) square of the moist Brunt-Väisälä frequency and (f) the relative vorticity though the center latitude of the vortex at 10°N. The maximum wind speed is 20 m $s^{-1}$ with an RMW of 250 km.

## 2.3 CAM 3.1 model description

We test and evaluate the effects of the initial conditions in idealized tropical cyclone simulations with the hydrostatic GCM CAM 3.1 (*Collins et al.*, 2004, 2006). CAM is part of NCAR's Community Climate System Model (CCSM) that is routinely used for climate change projections. We utilize a CAM 3.1 configuration with the mass-conservative finite-volume (FV) dynamical core in flux-form (*Lin*, 2004) that is built upon a 2D shallow water approach in the horizontal plane. The vertical discretization follows a "Lagrangian control-volume" principle, which is based on a terrain-following "floating" Lagrangian coordinate system and a fixed "Eulerian" reference frame. In particular, the vertically-stacked finite volumes are allowed to float for a duration of several (in our simulations 10) short dynamics time steps before they are mapped back monotonically and conservatively to a fixed hybrid reference system. The physics parameterizations are called immediately after the vertical remapping step. The advection algorithm makes use of the monotonic Piecewise Parabolic Method (PPM) with an explicit time-stepping scheme. A regular latitude-longitude computational mesh is selected that includes both pole points. The prognostic variables are staggered as in the Arakawa-D grid. An almost identical FV dynamical core with different physics parameterizations and SSTs was also used in the tropical cyclone studies by *Atlas et al.* (2005), *Shen et al.* (2006a) and *Zhao et al.* (2009).

CAM 3.1 is run with the identical $(\Delta\lambda, \Delta\varphi)$ horizontal grid spacings of 1.0°, 0.5°, 0.25° and 0.125° and 26 vertical $\eta$-levels (L26). The hybrid coefficients for the standard CAM 3.1 vertical levels are documented in *Jablonowski and Williamson* (2006b). The four horizontal resolutions correspond to grid spacings of about 110 km, 55 km, 28 km and 14 km in the equatorial region. The dynamics time steps at these four resolutions are 180 s, 90 s, 45 s and 22.5 s, respectively. The model is run with the full CAM 3.1 physics parameterization suite and utilizes the aqua-planet setup as proposed by *Neale and Hoskins* (2000), but with constant sea surface temperatures of

29°C. These isothermal SSTs prescribe very warm ocean conditions and avoid latitudinal gradients in the initial background surface pressure or atmospheric temperature fields. The only external forcing is the distribution of the insolation at the top of the atmosphere. In particular, the solar irradiance is set to equinox conditions with a solar constant of 1365 W $m^{-2}$. In addition, the distributions of atmospheric constituents, such as ozone, carbon dioxide, methane and nitrous oxide are prescribed. The ozone distribution is zonally symmetric. The geophysical constants, including the earth's rotation rate, the gravitational acceleration and gas constants follow the suggestions by *Neale and Hoskins* (2000).

The CAM 3.1 physics suite is described in detail in *Collins et al.* (2004). It incorporates the *Zhang and McFarlane* (1995) deep convective parameterization, shallow moist convection and dry adiabatic adjustment, cloud microphysics, orographic gravity wave drag, the radiative effects of aerosols and parameterizations of shortwave and longwave radiation. In addition, the bulk exchange formulations for surface fluxes are based on the Monin-Obukhov similarity theory, and the vertical diffusion and boundary layer processes with turbulent mixing depend on static stability indicators.

## 2.4 Sensitivity of the cyclone to initial conditions

In this section we provide a series of sensitivity tests to varying initial conditions, including the initial maximum wind speed and the RMW. For this study the RMW is assessed as the great circle distance between the wind maximum to the location of the vortex center as determined by the surface pressure minimum. Using the location of the surface pressure minimum as the vortex center can lead to errors of up to a half-grid spacing in the estimated RMW, which should be kept in mind during the analysis. In addition, we supply sensitivity tests to a different initial moisture profile and to small changes in the initial velocity and temperature fields. The aqua-planet tests are run for ten days at both 0.5° and 0.25° horizontal resolutions. The results

inform us about a configuration that triggers an intense tropical cyclone-like vortex from an initial vortex seed. A selected configuration is then used as the control case for further convergence studies in Section 2.5.

### 2.4.1 0.5° resolution sensitivity to initial size and strength

The first analysis assesses variance of the initial maximum wind speed while keeping the initial RMW constant at 250 km. Maximum wind speeds $v_0$ are 15 m s$^{-1}$, 20 m s$^{-1}$, 25 m s$^{-1}$ and 30 m s$^{-1}$, which are derived from the prescribed $r_p$ and $\Delta p$ values discussed in Section 2.2. The corresponding $r_p$ and $\Delta p$ values for the four wind values are listed in Table 2.2. Figure 2.5 shows the time evolution of the minimum surface pressure, maximum wind speed and radius of maximum wind at 100 m for the four initial setups. The wind speed is linearly interpolated to this height level using the wind speeds and heights of the two surrounding model levels. The lowermost model level always lies below 100 m, which avoids extrapolation.

Table 2.2: Corresponding $r_p$ and $\Delta p$ constants for sensitivity tests with varying initial maximum wind speed and RMW.

| Constant RMW = 250 km | | |
|---|---|---|
| $v_0$ (m s$^{-1}$) | $r_p$ (km) | $\Delta p$ (hPa) |
| 15 | 290 | 6.84 |
| 20 | 282 | 11.15 |
| 25 | 276 | 16.46 |
| 30 | 273 | 22.80 |

| Constant $v_0$ = 20 m s$^{-1}$ | | |
|---|---|---|
| RMW (km) | $r_p$ (km) | $\Delta p$ (hPa) |
| 150 | 162 | 9.99 |
| 200 | 221 | 10.56 |
| 250 | 282 | 11.15 |
| 300 | 345 | 11.74 |

Figure 2.5 reveals that the initial vortex does not intensify immediately. The time it takes for the initial vortex to intensify seems to be dependent upon the initial intensity. The weakening shortly after the initialization is most likely due to the spin

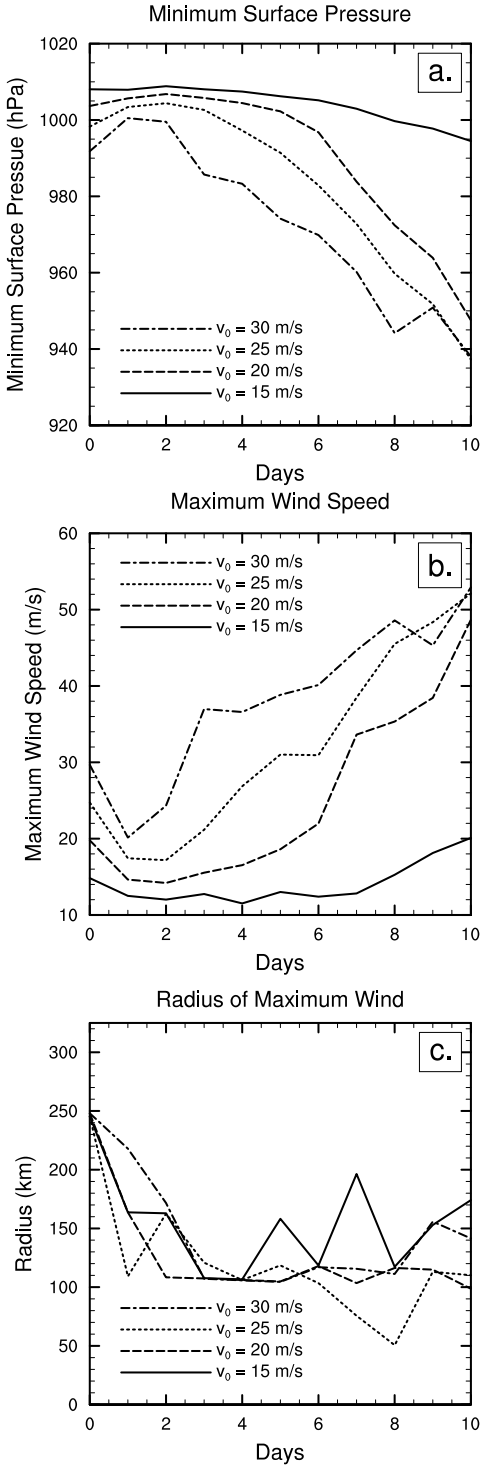


Figure 2.5: Time evolution of the (a) minimum surface pressure, (b) maximum wind speed at 100 m and (c) radius of maximum wind at 100 m with varying initial maximum tangential wind speed and constant initial RMW of 250 km. The grid spacing is 0.5°.

down of the vortex due to surface friction and the need for the development of a secondary circulation. The secondary circulation is absent in the initial conditions and takes some time to spin up. In addition, the vortex is not in perfect balance on the spherical grid as mentioned earlier. Both the surface pressure and maximum wind speed plots show that for the two strongest initial conditions, $v_0 = 30$ m s$^{-1}$ and $v_0 = 25$ m s$^{-1}$, there is an initial weakening of the vortex for the first day and first two days, respectively, after which point the vortex begins to intensify. For the $v_0 = 20$ m s$^{-1}$ case we also see a slight weakening of the initial vortex, but although the vortex starts to intensify at day 2, it does not intensify significantly until day 6.

The results suggest that there is a threshold value of the initial strength of the vortex $v_0$ between 15 m s$^{-1}$ and 20 m s$^{-1}$, below which development does not occur. This is evidenced by the $v_0 = 15$ m s$^{-1}$ case, which never intensifies significantly within 10 days. In addition, further tests (not shown) reveal that an initial vortex with $v_0 = 15$ m s$^{-1}$ never develops significantly for any initial RMW=150–300 km.

The second group of tests explores varying initial values of the RMW from 150 km to 300 km in increments of 50 km, while holding the initial maximum wind speed at a constant 20 m s$^{-1}$. In order to keep the maximum wind speed constant at different RMW both $r_p$ and $\Delta p$ have to be adjusted. The values are listed in Table 2.2. Note again that the discrete grid spacing in CAM 3.1 causes the initial RMW in the model to slightly deviate from the theoretical values.

The results in Fig. 2.6 show that the vortex intensity initially decreases for a day, at which point the three cases with the largest initial RMW (200-300 km) start to intensify. By day 2, the vortex for these three cases has intensified and begins a rapid intensification phase at day 6. The two largest RMW cases become the strongest, with the 250 km case showing maximum 100 m wind speeds of about 48 m s$^{-1}$ at day 10. While the third case (RMW=200 km) intensifies, it does not become as strong as the other two cases after 10 days. For the fourth case, RMW=150 km, the

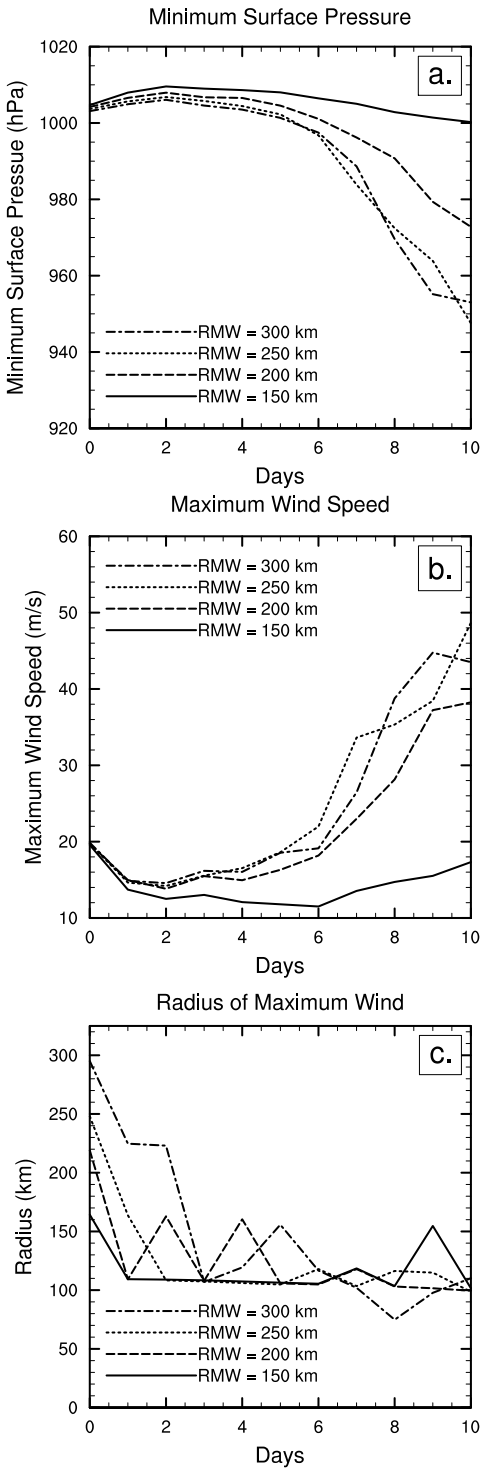


Figure 2.6: Time evolution of the (a) minimum surface pressure, (b) maximum wind speed at 100 m and (c) radius of maximum wind at 100 m with varying initial RMW and constant initial maximum tangential wind of 20 m $s^{-1}$. The grid spacing is 0.5°

initial vortex weakens for two days and remains rather constant in intensity until day 6. It thereafter begins to slightly intensify, but it does not actually pass its initial maximum wind speed of 20 m $s^{-1}$ during the 10-day simulation.

When the initial vortex is weak, it apparently needs to be of an initial RMW equal to or greater than roughly 200 km in order to intensify. Further experiments at 0.5° (not shown) give evidence that an initial vortex can intensify when the initial RMW is less than 200 km, but to do so requires that $v_0$ be substantially greater than 20 m $s^{-1}$ ($\approx$ 30 m $s^{-1}$, which is nearly hurricane strength). The fact that the 0.5° simulation can support 100 km vortices by day 10 demonstrates that the reason why smaller initial vortices fail to develop may not be simply an issue of inadequate horizontal resolution. However, further tests (described later) show that the RMW=150 km case does develop at 0.25° resolution, so the failure mechanism is at least indirectly related to model resolution. Possible failure mechanisms here include the initial structure of the vortex (e.g., imbalance) and the nature of convection at lower horizontal resolutions. However, an in-depth investigation of these factors is not the focus of this study.

These results seem to contrast somewhat with those of *Rotunno and Emanuel* (1987) and *Emanuel* (1989). For example, *Rotunno and Emanuel* (1987) found that larger initial vortices struggle to develop. We find that an additional vortex simulation with an initial RMW of 500 km (not shown) is only slightly weaker by day 10 than those with smaller initial RMW. However, there is no clear relationship between the initial RMW and the later strength for the smaller initial vortices in Fig. 2.6 (omitting the RMW=150 km case which does not develop). In addition, the somewhat weaker evolution for the initial RMW=200 km case might reflect the fact that the vortex lies in the transition region wherein the structure of the smaller initial vortices cannot be supported by the model. *Emanuel* (1989) also found that the length scale of the mature vortex depends on that of the initial vortex. In contrast, we find that

there is no relationship between the initial and final RMW. Furthermore, we find that varying the initial RMW has less of an impact on the final RMW variability than does varying the initial maximum wind speed $v_0$ (Fig. 2.5). A better understanding of how our results compare with those two studies would require additional simulations that are beyond the scope of this study. Nonetheless, any differences from *Rotunno and Emanuel* (1987) and *Emanuel* (1989) are seen as a result of a differing initial vortex structure and the use of a different model with varying model resolution and model physics.

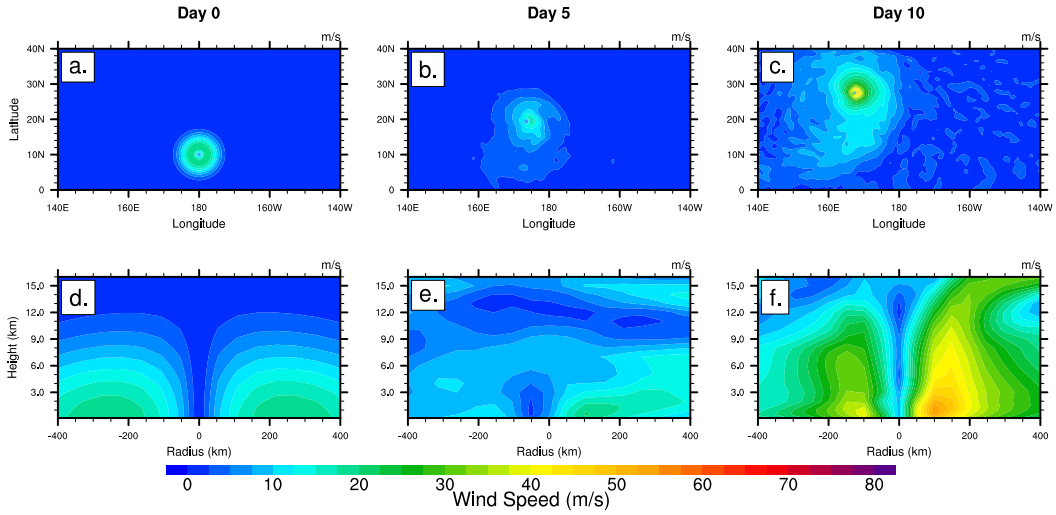


Figure 2.7: Snapshots of the tropical cyclone-like vortex at day 0 (left), 5 (middle) and day 10 (right) at the resolution 0.5° L26. Top row (a-c): horizontal cross section of the wind speed at a height of 100 m. Bottom row (d-f): longitude-height cross section of the wind speed through the center latitude of the vortex as a function of the radius from the vortex center. The initial maximum wind is 20 m $s^{-1}$ with an RMW of 250 km. The center position is (167.5°E, 27.5°N) at day 10.

From the sensitivity studies of the varying initial conditions we choose a control case for further analysis. The control case produces the strongest storm from a weak initial vortex. We choose the case with $v_0 = 20$ m $s^{-1}$ and RMW= 250 km as our control case, which corresponds to $r_p = 282$ km and $\Delta p = 11.15$ hPa. Figure 2.7 shows the intensification of the wind speed for the control case, with specific snapshots at days 0, 5 and 10. The top row of Fig. 2.7 displays the horizontal cross

section of the magnitude of the wind at 100 m. The bottom row of Fig. 2.7 shows the longitude-height cross section of the magnitude of the wind through the center latitude of the vortex. The time series displays the intensification of the vortex from an initial surface vortex to a tropical cyclone-like vortex. We also see strong vertical development, especially near the RMW. During the entire simulation the cyclone experiences beta-drift towards the north-west (*Holland*, 1983). There is also somewhat of a resemblance of a calm eye that forms as the vortex intensifies. However, due to resolution constraints the eye is not completely defined. The cyclone is a warm-core vortex (not shown).

### 2.4.2 0.25° resolution sensitivity to initial size and strength

We repeat the sensitivity tests at a higher horizontal resolution of 0.25°, or about 28 km, to assess the robustness of the sensitivity analysis and the control case. Again, we review the sensitivity to the varying initial maximum wind speeds with a constant RMW of 250 km presented in Table 2.2. Similar to the 0.5° tests depicted in Fig. 2.5, Fig. 2.8 shows that at first the intensity weakens, and the initially stronger vortices rebound from this weakening more quickly and strongly. Rapid intensification occurs after one day for the strongest case, $v_0 = 30$ m s$^{-1}$, and at days 2 and 3 for the $v_0 = 25$ m s$^{-1}$ and $v_0 = 20$ m s$^{-1}$ cases, respectively. The $v_0 = 15$ m s$^{-1}$ case intensifies substantially more within the ten day simulation (but the intensity is still less than the other 3 cases) at the 0.25° resolution than that at the 0.5° resolution, reaching an intensity of over 2.5 times that of the lower resolution. This suggests that the threshold intensity needed to foster development and rapid intensification is resolution dependent.

All three plots in Fig. 2.8 show that the vortices develop into more intense and more compact cyclones at the higher resolution, with the maximum wind speed at 100 m approaching a value of 62 m s$^{-1}$ for the strongest three cases. Such a storm would

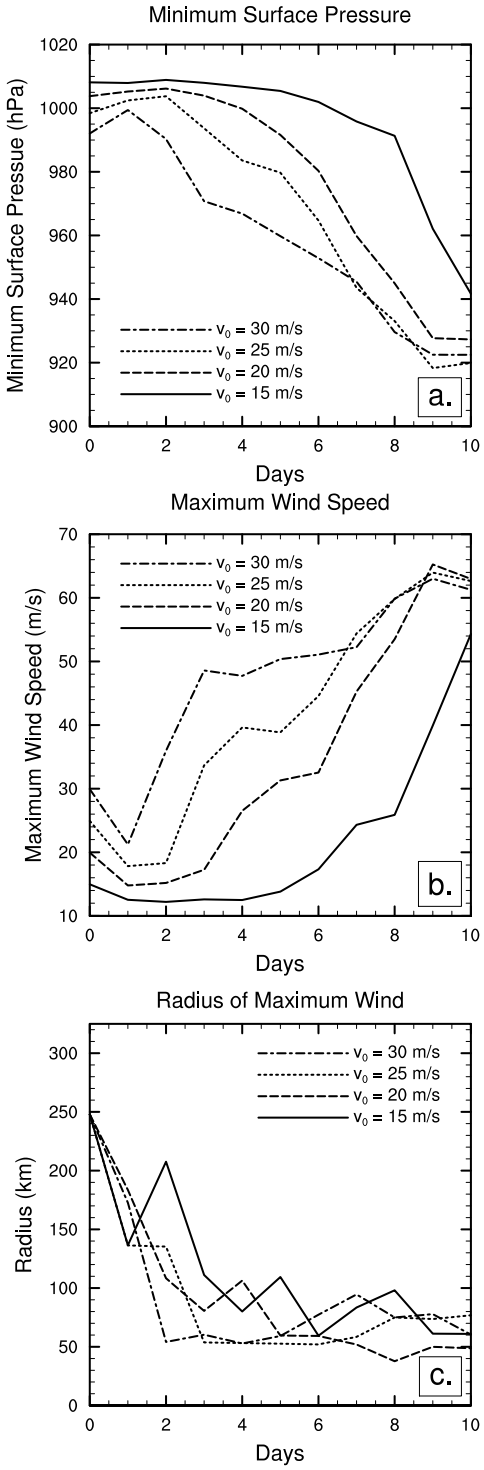


Figure 2.8: Same as Fig. 2.5, but for the 0.25° resolution.

correspond to a category-4 hurricane on the Saffir-Simpson scale. Additionally, the RMW for each case seems to converge towards a value in between roughly 50 and 80 km at day 10 for all cases, which is smaller than the RMW range at the 0.5° resolution. Similar resolution dependencies are also discussed in *Bengtsson et al.* (2007) and *Hill and Lackmann* (2009a).

The second set of tests at the 0.25° resolution is an examination of the sensitivity to varying initial RMW with a constant maximum wind speed of $v_0 = 20$ m s$^{-1}$. The associated $r_p$ and $\Delta p$ values are again listed in Table 2.2. The results are very similar to those with the 0.5° grid spacing. Initially, the intensity of all vortices weakens for two days and then increase as seen in Fig. 2.9. However, the vortices begin rapid intensification by day 3, which is three days earlier than for the 0.5° tests (Fig. 2.6). By day 10 the maximum 100 m wind speed approaches 62 m s$^{-1}$ for the two cases with the largest RMW. In addition, the case with an initial RMW of 150 km develops substantially more at 0.25° than at 0.5° resolution, indicating that a vortex with a smaller RMW more readily develops when the model resolution is higher.

The RMW plot in Fig. 2.9 shows that as the vortex develops the RMW ranges between 50 and 100 km in all cases. They have a smaller RMW at day 10 as compared to the 0.5° resolution runs. Similar to the 0.5° resolution runs, varying the initial maximum wind speed has more of an effect on the subsequent RMW variability than does varying the initial RMW. Given a suitable initial size the initial maximum wind speed $v_0$ of the cyclone seems to be the decisive factor that determines the potential for development and rapid intensification.

The analysis suggests that the control case described above will suffice in the simulation of the growth of the initial vortex into a tropical cyclone for both the 0.25° and 0.5° simulations. Figure 2.10 is the same as Fig. 2.7, but for 0.25° resolution. It displays snapshots of the wind speed for the control case in both a horizontal and vertical cross section at day 0, 5 and 10. At the higher resolution the cyclone becomes

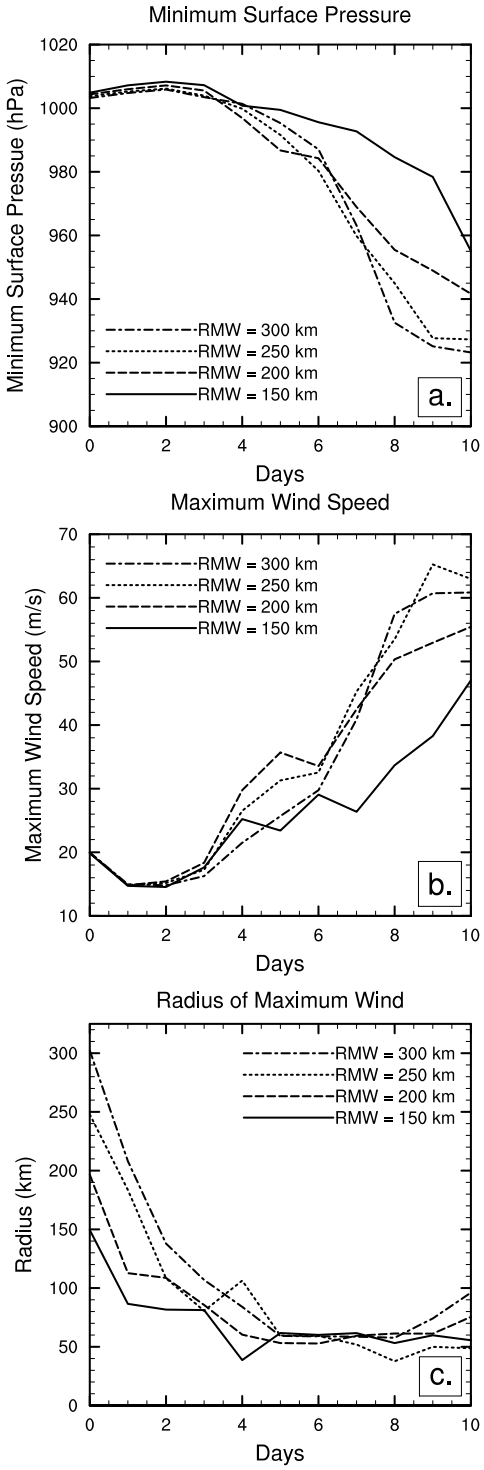


Figure 2.9: Same as Fig. 2.6, but for the 0.25° resolution.

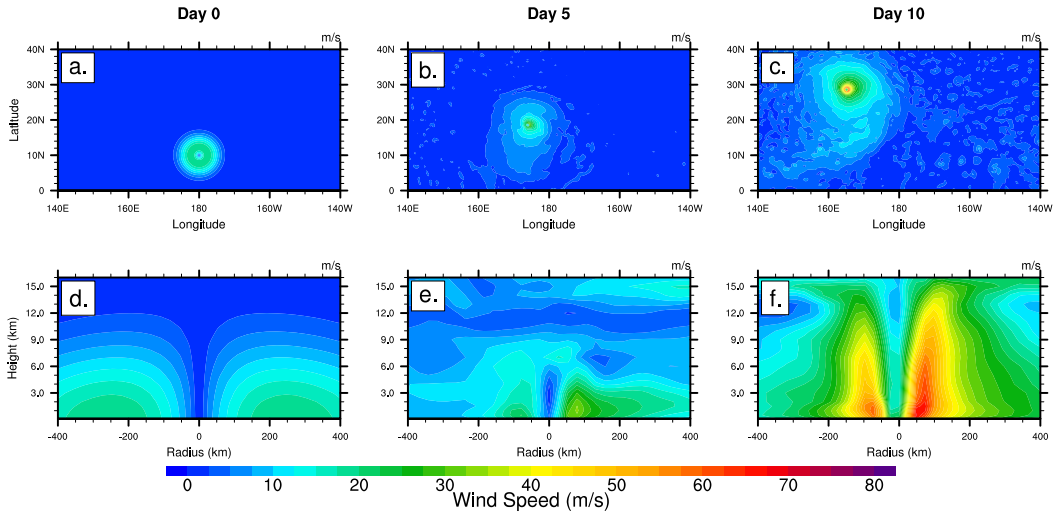


Figure 2.10: Same as Fig. 2.7, but for the 0.25° resolution. The center position is (165.25°E, 28.75°N) at day 10.

substantially (about 14 m $s^{-1}$) stronger by day 10. The day-5 snapshot also shows that the storm has intensified quicker than the 0.5° resolution case (Fig. 2.7). In addition, there is more significant vertical development, with a noticeable slant of the eyewall, and the storm is more compact as indicated by a smaller RMW.

### 2.4.3 0.25° resolution sensitivity to small changes in the initial fields

The model sensitivity to tiny changes in the initial temperature and velocity fields within the vortex is tested. This is done by changing the value $\varepsilon$ to which the iterations in Eq. (2.25) converge. This produces very small changes in the height and therefore initial fields within the vortex. The model is run for three values of $\varepsilon$ that are $2 \times 10^{-13}$, $2 \times 10^{-12}$ and $2 \times 10^{-11}$. These small changes in $\varepsilon$ result in maximum absolute differences in the zonal and meridional velocity fields of about $1 \times 10^{-13}$ m $s^{-1}$ and in the temperature field of about $1 \times 10^{-12}$ K. Figure 2.11 displays the time evolution of the minimum surface pressure, maximum wind speed and radius of maximum wind at 100 m for the three different values of $\varepsilon$ using the control specific humidity at the surface ($q_0 = 21$ g $kg^{-1}$). It is evident that even very small changes in the model initialization can cause some small but notable variations in the storm's

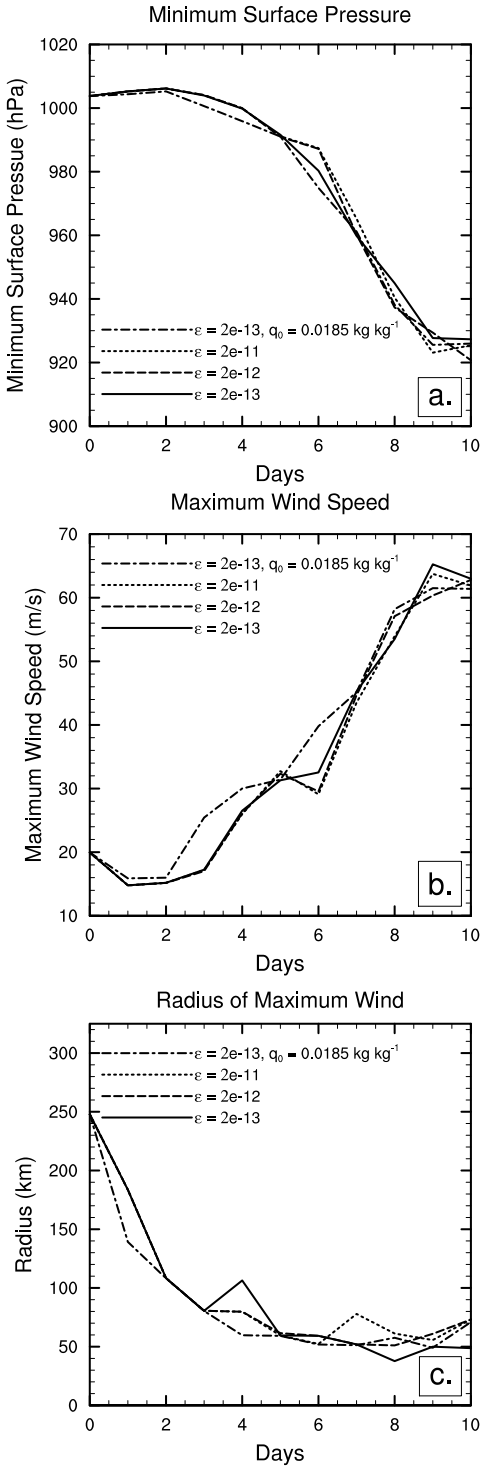


Figure 2.11: Time evolution of the (a) minimum surface pressure, (b) maximum wind speed at 100 m and (c) radius of maximum wind at 100 m with slight changes to the initial fields as indicated by the convergence limit for the fixed-point iterations $\varepsilon$. The specific humidity at the surface is set to $q_0$ =21 g kg$^{-1}$ except in the case with $q_0$ =18.5 g kg$^{-1}$. The grid spacing is 0.25°.

intensity and size during the 10-day simulation. This indicates that there might be a predictability limit after which the solutions have greater uncertainty. Such a limit of predictability due to minute changes in initial conditions is also observed in *Zhang and Sippel* (2009) using a mesoscale model and the study implies that the predictability of tropical cyclones in models is restrained at all time scales.

### 2.4.4 0.25° resolution sensitivity to the moisture profile

We also test the sensitivity to the low-level moisture. In Eq. (2.1) we set the specific humidity at the surface $q_0$ to 21 g kg$^{-1}$ according to the *Jordan* (1958) relative humidity profile with the surface temperature of 29°C. However, $q_0$ could also be set to the specific humidity value of the *Jordan* (1958) sounding at the surface, which is 18.5 g kg$^{-1}$. This would cause a change in the initial moisture profile and therefore the initial temperature profile. It is informative to evaluate the sensitivity of the model simulations to such variations of the initial conditions as shown by the fourth experiment in Fig. 2.11. The time evolution of the minimum surface pressure, maximum wind speed and radius of maximum wind at 100 m can be compared for the two cases with $\varepsilon = 2 \times 10^{-13}$ that utilize the default setting $q_0 = 21$ g kg$^{-1}$ and the new value of 18.5 g kg$^{-1}$. It is apparent that the change in the initial profiles causes only small changes, on par with those discussed earlier in Section 2.4.3. The $q_0 = 18.5$ g kg$^{-1}$ case with decreased low-level moisture results in a slightly weaker storm at day 10, but the variation lies within the uncertainty range discussed above. This small sensitivity to the initial moisture profiles could be due to the use of a relatively coarse model resolution and the specifics in the CAM 3.1 model physics, in particular in the convection parameterization.

## 2.5 Horizontal resolution convergence test

The previous section identified the control case with $v_0 = 20$ m s$^{-1}$ and RMW= 250 ($r_p = 282$ km, $\Delta p = 11.15$ hPa). We now initialize this vortex at the wide range of horizontal resolutions (1.0°, 0.5°, 0.25° and 0.125°) with 26 levels to gain insight into the physical characteristics of the idealized cyclone. All simulations are run with identical physical parameterizations without re-tuning the physics parameter set. The adjustable parameters have been derived for CAM 3.1 climate simulations with the Eulerian spectral transform dynamical core at the T85L26 resolution (see *Collins et al.* (2004)). We use these defaults to match the CAM 3.1 aqua-planet setups assessed in *Williamson* (2008a,b). We do not change the vertical resolution since the CAM 3.1 physics parameterization suite is known to be sensitive to the placement of the levels.

Figure 2.12 presents the time evolution of the minimum surface pressure, maximum wind speed at 100 m and the position of the storm centers at all four horizontal resolutions. The storm centers are determined by the grid point locations of the minimum surface pressure. The filled circles in Fig. 2.12(c) denote the daily positions over the 10-day simulation period.

As the horizontal resolution increases the vortex becomes more intense by day 10. The maximum 100 m wind at day 10 is 48.7 m s$^{-1}$, 63.0 m s$^{-1}$ and 72.4 m s$^{-1}$ for the horizontal resolutions of 0.5°, 0.25° and 0.125°, respectively. Note that the absolute maximum wind occurs at approximate heights of 1–1.5 km, where wind speeds are about 6–11 m s$^{-1}$ greater than those at the height of 100 m. The storms simulated at the higher resolutions also intensify earlier during the simulation, as seen in the minimum surface pressure and maximum wind speed plots. This is evidenced by the fact that after the initial weakening it takes the vortex 132, 84 and 72 hours at 0.5°, 0.25° and 0.125°, respectively, to surpass the initial maximum wind speed of 20 m s$^{-1}$. In the 1.0° simulation the storm never becomes as strong as the initial vortex.

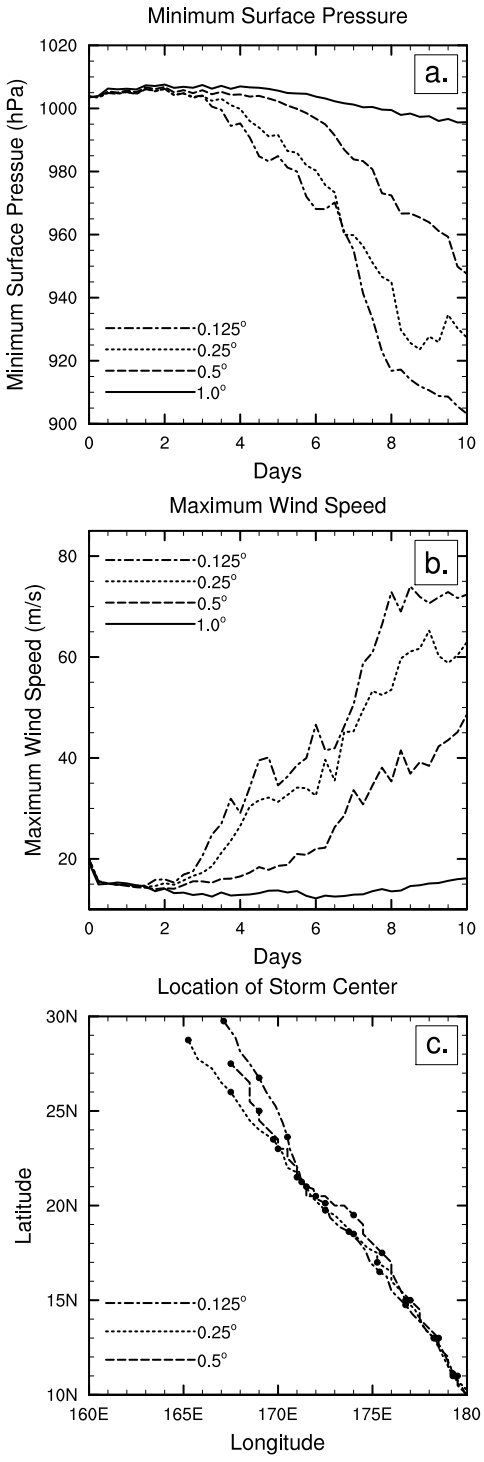


Figure 2.12: Time evolution of the (a) minimum surface pressure, (b) maximum wind speed at 100 m and (c) the location of the storm center for simulations at four horizontal resolutions ranging from 1.0° to 0.125°. The filled circles in (c) denote the daily positions of the center over the 10-day simulation period.

There is no sign of convergence in intensity at the highest resolutions, which might suggest that even higher resolutions are desirable.

In addition, Fig. 2.12(c) shows that the horizontal resolution impacts the storm track and location of the storm center. The spread in the positions increases notably after day 8. However, the center positions do not change systematically with resolution.

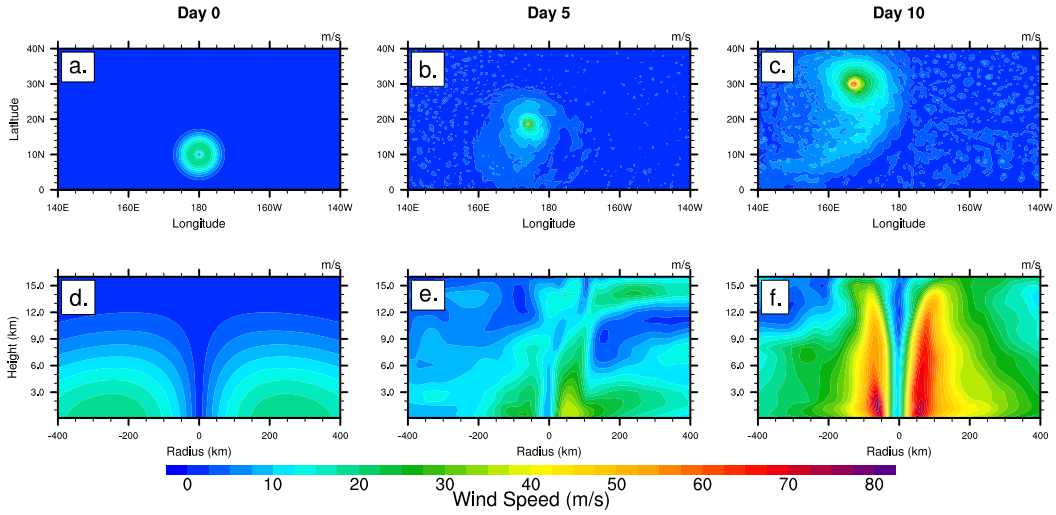


Figure 2.13: Same as Fig. 2.7, but for the 0.125° resolution. The center position is (167.125°E, 29.75°N) at day 10.

When simulated at 0.125° (Fig. 2.13), the cyclone is stronger and more compact than the storms at both 0.5° (Fig. 2.7) and 0.25° (Fig. 2.10) simulations. Similar results were also found by *Bengtsson et al.* (2007). The 0.125° cyclone has a distinct slanted eyewall-like structure and relatively calm eye at day 10. The 100 m maximum wind speed at day 10 of 72.4 m $s^{-1}$ is equivalent to a category-5 hurricane on the Saffir-Simpson scale.

It is interesting to note that this intensity is larger than the estimated Emanuel's MPI of about 66 m $s^{-1}$, which could be related to inadequate physics parameterizations at these high resolutions. As mentioned before, no tuning of the physics parameterizations, such as the convection and boundary layer parameterizations, were made. It is possible that this allows for storms that are too intense. However, further

investigations of the physics parameterizations are beyond the scope of this investigation and will be a subject of future work. Simpler axisymmetric hurricane models and full-physics 3D models have also been documented to produce storms that exceed Emanuel's MPI. This is discussed in *Persing and Montgomery* (2003), *Bryan and Rotunno* (2009a) and *Wang and Xu* (2010).

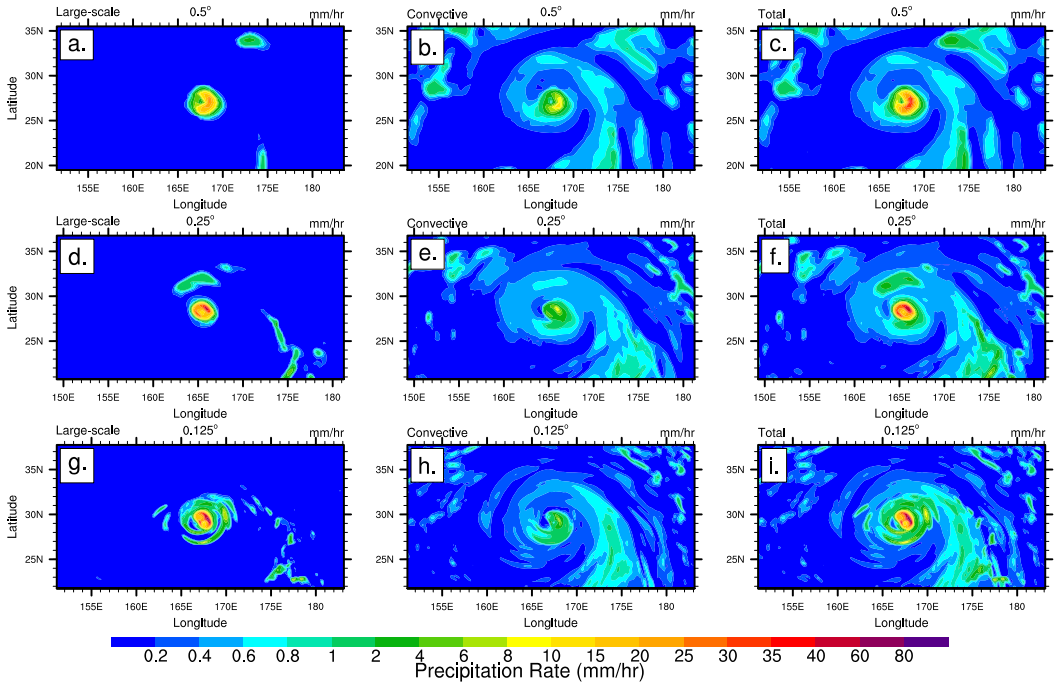


Figure 2.14: Precipitation rate in mm per hour at day 10 for large-scale precipitation (left), convective precipitation (middle) and total precipitation (right) for 0.5° (a-c), 0.25° (d-f) and 0.125° (g-i) simulations. At day 10 the storm is centered at (167.5°E, 27.5°N), (165.25°E, 28.75°N) and (167.125°E, 29.75°N) for the 0.5°, 0.25° and 0.125° simulations, respectively.

Figure 2.14 displays the precipitation rate for large-scale, convective and the total precipitation at day 10 for the 0.5°, 0.25° and 0.125° simulations. It can be seen that as the horizontal resolution increases from 0.5° to 0.125° the precipitation fields show rainband-like features spiraling out from the storms center that become increasingly resolved. These rainband-like features are apparent in both the large-scale and convective precipitation fields.

Figure 2.14 also shows that for all simulations the large-scale precipitation contributes the majority to the total precipitation near the central core of the storm. Even though Fig. 2.13 shows a relatively calm eye there is still precipitation in the eye at the 0.125° resolution. The most intense total precipitation rate for the 0.125° simulation is near the center of the storm and has a maximum value of about 88.22 mm $hr^{-1}$ which represents a 6-hour average. This rather extreme peak precipitation rate only covers a very small region, but could provide another hint that the physics parameterizations might need re-tuning at these high resolutions with hurricane strength winds.

Table 2.3: Maximum 6-hour average rainfall rates of total, convective and large-scale precipitation at days 5 and 10 for the 0.5°, 0.25° and 0.125° simulations in mm $hr^{-1}$.

Day 5

| | Total | Convective | Large-scale |
|---|---|---|---|
| 0.5° | 3.99 | 2.77 | 1.66 |
| 0.25° | 31.47 | 5.54 | 25.93 |
| 0.125° | 47.74 | 2.68 | 46.66 |

Day 10

| | Total | Convective | Large-scale |
|---|---|---|---|
| 0.5° | 36.96 | 10.88 | 26.32 |
| 0.25° | 58.57 | 10.42 | 48.15 |
| 0.125° | 88.22 | 8.90 | 79.32 |

Table 2.3 lists the maximum large-scale, convective and total precipitation rates at day 5 and 10 for the 0.5°, 0.25° and 0.125° simulations. As the resolution increases the maximum 6-hour average total and large-scale precipitation rates increase, while the maximum convective precipitation rate decreases mainly in the core of the storm. These results are similar to other aqua-planet studies that address the convergence with resolution aspects of global precipitation (*Williamson*, 2008a) and equatorial precipitation fields (*Lorant and Royer*, 2001).

As a last point we assess the realism of highest resolution (0.125°) simulation

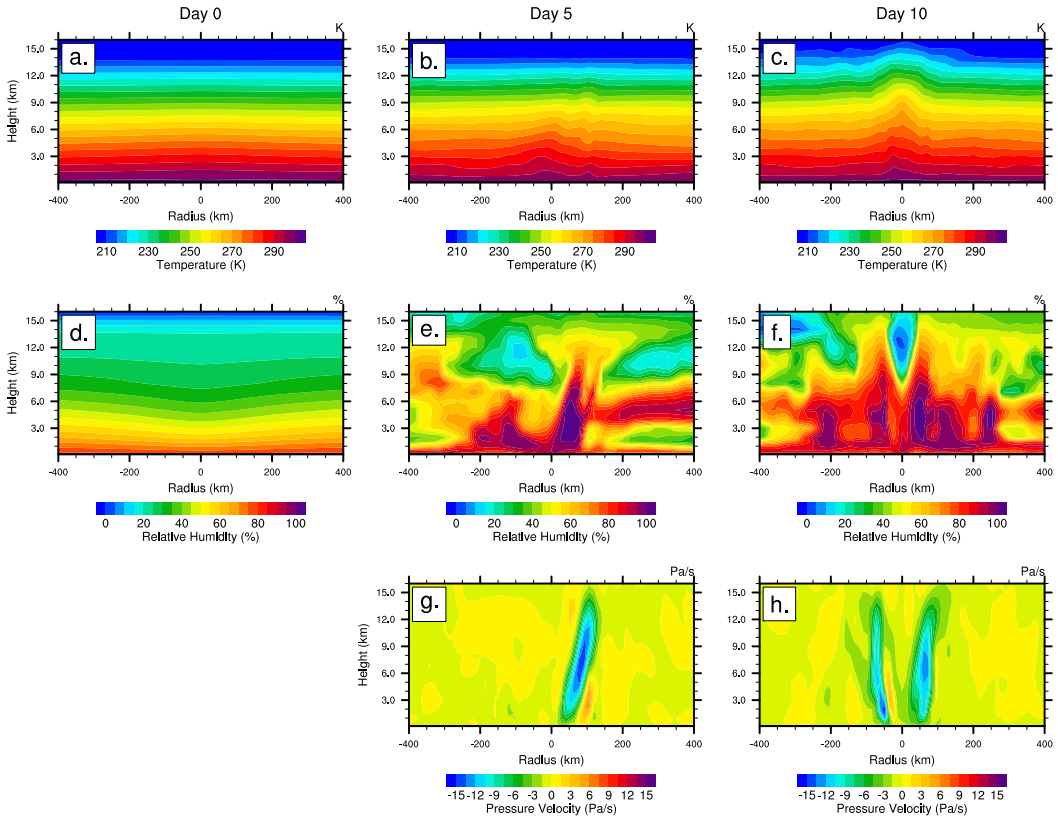


Figure 2.15: Snapshots of the 0.125° simulation at days 0 (left), 5 (middle) and 10 (right). The temperature (a-c), relative humidity (d-f) and vertical pressure velocity (g-h) are displayed as longitude-height cross sections through the center latitude (29.75°N) of the vortex as a function of the radius from its center.

used in the convergence study. Figure 2.15 displays vertical cross sections through the center latitude of the vortex as a function of the radius from the center of the vortex for the temperature, relative humidity and vertical pressure velocity at days 0, 5 and 10 for the 0.125° simulation. The top row shows the evolution of the warm core. At day 0 there is only a slight perturbation representing the warm core, and by day 5 and 10 the perturbation has become more defined.

The middle row of Fig. 2.15 shows the relative humidity. At day 0 the maximum is located at the surface as prescribed in the initial conditions. By day 5 the troposphere near the center of the storm has moistened, reaching saturation in some locations. By day 10 the atmosphere has moistened even more, especially near the eyewall

at the radius of about 50 km, with high relative humidities reaching high into the troposphere. In addition, the day-10 relative humidity field is rather symmetric about the center of the storm, indicating an organized, intense storm. Another indication of an organized storm is the relative humidity minimum located at the center of the storm just below the tropopause. The large values of the relative humidity at the center of the storm in the lower and middle troposphere are linked to the precipitation that is seen at the center (Fig. 2.14). At day 10 the relative humidity field also shows hints of spiral rainbands with areas of maximum relative humidity that extend into the vertical at a radius slightly larger than 200 km.

The vertical pressure velocity fields (bottom row of Fig. 2.15) confirm the evolution of the intense organized storm by day 10, with a maximum value of about -15.72 Pa $s^{-1}$ near the RMW as expected with intense updrafts in the eyewall. At day 10, there is also a distinct downdraft region slightly (25 km) west of the storm center positioned at (28.75°N, 165.25°E). The downdrafts reach from the surface to a height of about 9 km. Note that initially (day 0) the pressure velocity is zero and therefore omitted in the figure.

Three conclusions can be drawn from the convergence study. First, the vortex seed as specified in the control case develops into a strong tropical cyclone-like storm at all resolutions except at the coarsest 1° grid spacing. Second, the physical characteristics of the idealized storms have many realistic features, especially the highest resolution (0.125°) simulation. Third, the model simulations do not converge in intensity in the range of horizontal resolutions between 110 and 14 km. The latter aspect needs further investigation. Overall, the results suggest that the analytic functions represent a robust initialization technique to study idealized cyclones in GCMs.

## 2.6 Summary and conclusions

The paper introduces an analytic initialization technique for idealized tropical cyclone experiments in atmospheric general circulation models. The initial axisymmetric vortex is in hydrostatic and gradient-wind balance and provides favorable conditions for rapid intensifications over a simulation period of 10 days. The initial data set triggers the evolution of a single, weak warm-core vortex into a much stronger tropical cylone-like storm. This has been demonstrated in high-resolution simulations with the Community Atmosphere Model CAM 3.1. The simulations were conducted in an aqua-planet configuration with constant SSTs of 29°C. 10-day model simulations with grid spacings of 1.0°, 0.5°, 0.25° and 0.125° and 26 vertical levels were shown.

Several sensitivity studies were presented that highlighted the effects of varying initial conditions. In particular, the role of the maximum initial wind speed and radius of maximum wind has been investigated. We showed that the initial vortex must satisfy certain threshold conditions to support the intensification of the pre-existing vortex. We found that the prescribed vortices with a maximum initial wind speed of 15 m $s^{-1}$ did not develop into strong tropical storms in both the 0.5° and 0.25° simulations during the 10-day assessment period. A suitable vortex must therefore exhibit a maximum initial wind speed that is stronger than this threshold, approximately 20 m $s^{-1}$, for the described analytic initialization technique. In addition, the initial RMW needs to be at least 200–250 km wide to foster the intensification of the pre-existing storm that is initially weak ($v_0$ =20 m $s^{-1}$). However, the model can support storms with RMW of 100 km and this initial RMW threshold of 200–250 km is possibly related to the initial structure of the vortex and the behavior of the model physics. These thresholds do vary with model resolution. In general, the high-resolution experiments with 0.25° grid spacing lead to more intense and compact storms than the lower resolution (0.5°) simulations.

A favorable initial configuration was picked as a candidate to study the impact of horizontal resolution on the evolution of the tropical cyclone-like vortices. This control case has an RMW of about 250 km and a 20 m $s^{-1}$ maximum initial wind speed and is used as the basis for a second group of sensitivity tests in which the horizontal resolution is recursively halved from 1.0° to 0.125°. As the resolution increases the initial vortex produces storms that are more intense and compact. The storm simulated at the finest 0.125° resolution even exceeds Emanuel's maximum potential intensity limit of about 66 m $s^{-1}$. This gives an indication that the physics suite might need to be modified at high resolutions. At the highest resolution the model starts to resolve rainband-like structures as seen from the precipitation and relative humidity fields. In addition, we see regions of intense updrafts near the RMW. However, despite the relatively calm eye (in terms of wind speed) there is still precipitation and large relative humidity values within the eye. Again, this might indicate potential inadequacies within the physics package at high resolutions or for intense hurricane conditions. It also could indicate that even higher resolutions are necessary, both in the horizontal and, equally important, vertical directions.

In future work, we will use these idealized initial conditions to assess different types of physics parameterizations and their impact on tropical cyclone development in GCMs. In addition, we plan to assess the impact of different dynamical cores on the evolution of idealized cyclones.

# CHAPTER III

# Impact of physical parameterizations on idealized tropical cyclones in the Community Atmosphere Model

## 3.1 Introduction

Recent studies have shown the ability of general circulation models (GCMs) to simulate the development and evolution of tropical cyclones. These GCM studies range from short-term studies to long-term climate studies. For example, *Atlas et al.* (2005) and *Shen et al.* (2006b) used NASA's hydrostatic finite-volume GCM at horizontal resolutions of 0.25° and 0.125°, or 28 km and 14 km in equatorial regions, to simulate selected Atlantic hurricanes for a duration of 5 days. Climate studies, including *Oouchi et al.* (2006), *Bengtsson et al.* (2007) and *Zhao et al.* (2009), aim at understanding how tropical cyclones simulations will be altered by a warmer future climate. Since modern computing architectures now allow very high horizontal resolutions, that will soon approach the transition to non-hydrostatic scales, the use of GCMs to model tropical cyclones is likely to become even more prominent. This raises the question of how well their dynamical cores and physical parameterizations are suited to model the evolution of these rather extreme storms.

The use of GCMs to simulate tropical cyclones presents numerous challenges, in-

cluding the small size of the storms, the interaction of large-scale and small-scale processes and the parameterization of sub-grid scale physical processes. Such physical processes include the representation of convection (*Smith*, 2000) and the surface and planetary boundary layers (*Hill and Lackmann*, 2009a). These processes play a paramount role in tropical cyclone development. The choice of the parameterization schemes highly influences the ability of a GCM to simulate tropical storms. This paper sheds light on the impact of one particular physical parameterization. It analyzes the sensitivity of a tropical cyclone to changes in the deep convection scheme in the National Center for Atmospheric Research's (NCAR) Community Atmosphere Model (CAM). In addition, the impact of a change in the cloud macrophysics is assessed.

*Reed and Jablonowski* (2011a) introduced an analytic initialization technique for GCMs to simulate the development of a single, initially weak vortex into a tropical cyclone. Such a vortex is placed into an idealized environment within an aquaplanet setup with a constant sea surface temperature (SST). They observed that high-resolution CAM version 3.1 (CAM 3.1) model runs, with horizontal grid spacings of 0.5° or less, are able to simulate the growth of the initial vortex into a tropical cyclone.

Recently, NCAR released an updated version of CAM, version 4 (CAM 4), in which changes were made to the physical parameterizations. The changes focused on the deep convection scheme. This paper aims to evaluate the impact of the individual enhancements within CAM 4 on the ability of the model to simulate tropical cyclones. The analytic initialization technique introduced in *Reed and Jablonowski* (2011a) provides a basis for such a comparison. Section 3.2 briefly reviews the design of the models CAM 3.1 and CAM 4 and Section 3.3 introduces the simulation design. Section 3.4 compares the simulations of the initially weak vortex into a tropical cyclone and explores the impact of the individual enhanced parameterizations within CAM 4. Section 3.5 discusses the conclusions and future research.

## 3.2 Model description

In this paper we use two versions of NCAR's CAM, version 3.1 (*Collins et al.*, 2004) and version 4 (*Neale et al.*, 2010a). CAM is part of NCAR's Community Climate System Model (CCSM) that is routinely used for climate change projections. We utilize both CAM 3.1 and CAM 4 in a configuration with the mass-conservative finite–volume (FV) dynamical core in flux-form on a regular latitude-longitude grid (*Lin*, 2004). An almost identical FV dynamical core with different physics parameterizations and SSTs was also used in the tropical cyclone studies by *Atlas et al.* (2005), *Shen et al.* (2006b) and *Zhao et al.* (2009) (cubed-sphere grid). CAM 3.1 and CAM 4 are run with the identical $(\Delta\lambda, \Delta\varphi)$ horizontal grid spacings of 1.0°, 0.5° and 0.25° and the default 26 vertical $\eta$-levels (L26). The three horizontal resolutions correspond to grid spacings of about 110, 55 and 28 km in the equatorial region. The dynamics time steps at these three resolutions are 180 s, 90 s and 45 s, respectively. The physics time step is ten times the dynamics time step. The models are run with the full physics parameterization suites and utilize the aqua-planet setup as proposed by *Neale and Hoskins* (2000), but with constant SSTs of 29°C.

The CAM 4 physics package is mostly identical to the CAM 3.1 physics suite except for two main enhancements to the *Zhang and McFarlane* (1995) deep convective parameterization. The first change is to the calculation of the Convective Available Potential Energy (CAPE). CAM 4 now assumes a dilute entraining plume (*Neale et al.*, 2008), replacing the standard undilute non-entraining plume method in CAM 3.1. The second enhancement is the addition of Convective Momentum Transport (CMT) in CAM 4 (*Richter and Rasch*, 2008).

Table 3.1: Physical parameterization suite configurations

| | |
|---|---|
| Case 1 | Full CAM 3.1 physics suite |
| Case 2 | Full CAM 4 physics suite |
| Case 3 | CAM 4 physics suite with CAM 3.1 undilute CAPE calculation |
| Case 4 | CAM 4 physics suite with CMT turned off |
| Case 5 | CAM 4 physics suite with both CAM 3.1 undilute CAPE calculation and CMT turned off |
| Case 6 | Case 5 with an additional modification to match CAM 3.1 cloud macrophysics |

## 3.3 Simulation design

The initialization technique for the model simulations is described in detail in *Reed and Jablonowski* (2011a). In all cases we initialize the model with a single, initially weak, warm-core vortex in an idealized background environment. The vortex has a radius of maximum wind (RMW) of about 250 km and a 20 m $s^{-1}$ maximum initial wind speed located at the surface. Table 3.1 provides a description of the simulations presented in Section 3.4. Simulations are run with both CAM 3.1 (case 1) and CAM 4 (case 2) physics. To understand the impact of the individual changes additional simulations are run with the CAM 4 physics suite. These configurations include the CAM 4 physics suite with the new dilute plume calculation of CAPE turned off in favor of the CAM 3.1 undilute plume CAPE calculation (case 3), no CMT used (case 4), and both cases 3 and 4 together (case 5). An additional configuration, case 6, is used and is explained in Section 3.4. Each model configuration is run for 10 simulation days with the identical physics tuning parameter set. These adjustable parameters have been derived for CAM 4 climate simulations with the FV dynamical core at 1.0° resolution as documented in *Neale et al.* (2010a).

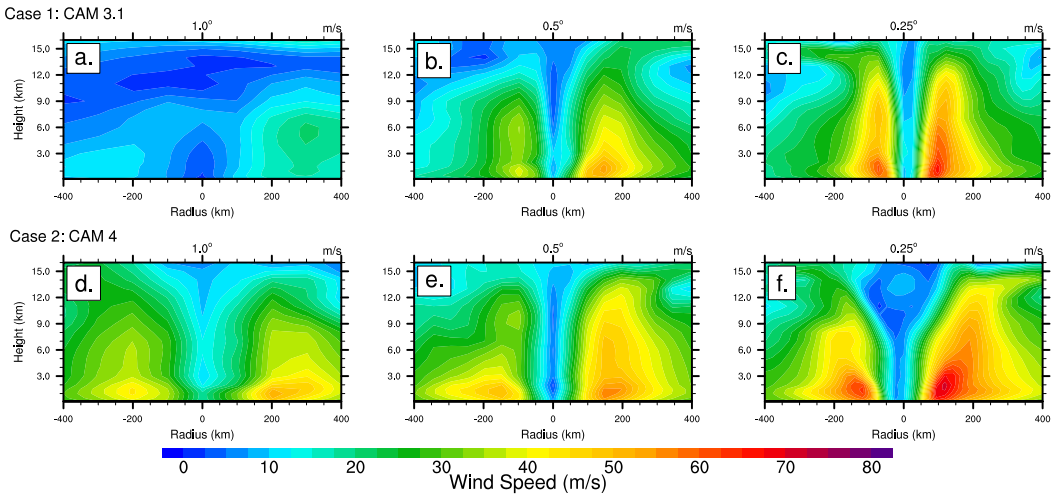


Figure 3.1: Snapshot of the longitude-height cross section of the wind speed through the center latitude of the tropical cyclone as a function of the radius from the vortex center at day 10. Top row: Results of case 1: CAM 3.1 physics simulations at the resolutions of (a) 1.0°, (b) 0.5° and (c) 0.25°. Bottom row (d-f): Results of case 2: corresponding CAM 4 physics simulations.

## 3.4 Results: Evolution of the tropical cyclone

### 3.4.1 Comparison of CAM 3.1 and CAM 4

Figure 3.1 displays the longitude-height cross section of the magnitude of the wind through the center latitude of the vortex at day 10 for simulations with CAM 3.1 physics (top row) and CAM 4 physics (bottom row) at all three resolutions 1.0°, 0.5° and 0.25°. At all resolutions the tropical cyclones simulated with CAM 4 physics (case 2) are stronger with a higher maximum wind speed by day 10 than those cyclones simulated with CAM 3.1 physics (case 1). Figure 3.1 also shows that at 1.0° the CAM 4 simulation produces a tropical cyclone with a broad RMW. In CAM 3.1 the initial vortex fails to intensify. This is in agreement with the 1.0° simulations of the control vortex in *Reed and Jablonowski* (2011a), which also used CAM 3.1 but with a different physics tuning parameter set.

Figure 3.1 indicates that the structure of the CAM 3.1 storm is rather different than that of the CAM 4 storm. At the 0.5° and 0.25° grid spacings, in which trop-

ical cyclones develop in both versions, the overall size of the CAM 4 storm is larger as evidenced by the larger range in which the strongest wind speeds occur. This is especially evident for the 0.25° grid spacing. The CAM 3.1 storm has a slightly smaller RMW than the CAM 4 storm and produces a much narrower area of vertical development. In addition, there is a noticeable difference in structure at higher altitudes. At 0.25° the CAM 3.1 simulation produces vertical development near the RMW that is almost directly vertical. The CAM 4 simulation also has an area of vertical development near the RMW, but the contours of constant wind speed start to slope more outward at higher altitudes (above 7 km).

Figure 3.2 shows the time evolution of the maximum wind speed at 100 m for each configuration listed in Table 3.1 at each resolution from 1.0° (top) to 0.25° (bottom). The wind speed is linearly interpolated to this height level using the wind speeds and heights of the two surrounding model levels. The lowermost model level always lies below 100 m, which avoids extrapolation. The figure reveals that all simulations experience an initial weakening of the storm, most likely due to surface friction and the lack of secondary circulation in the initial vortex (*Reed and Jablonowski*, 2011a). Figure 3.2 confirms that by day 10 the magnitude of the maximum wind speed at 100 m is greater for the CAM 4 simulations (case 2) than for the CAM 3.1 simulations (case 1) at all resolutions, except in the 0.25° simulations when the day-10 maximum wind speeds are roughly the same. Again, the figure shows that no tropical cyclone forms for the 1.0° simulation with CAM 3.1. At the other two resolutions (0.5° and 0.25°) the manner in which the cyclone intensifies is substantially different. After day 1 the CAM 4 storms begin to intensify rapidly (shown by the increase in maximum wind speed) while the CAM 3.1 storms do not start to intensify until much later, depending on the resolution. Despite this difference in intensification, the full CAM 3.1 and CAM 4 simulations at 0.25° approach approximately the same value of maximum wind speed by day 10. This may suggest that an intensity limit has been reached for

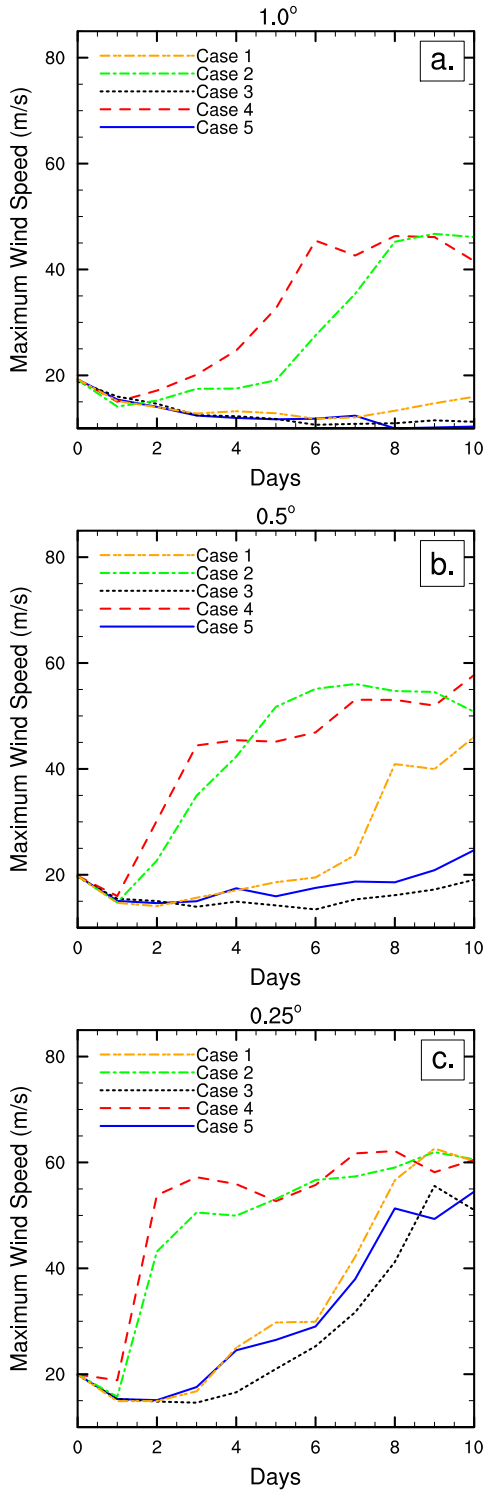


Figure 3.2: Time evolution of the maximum wind speed at 100 m for configuration 1 through 5 listed in Table 3.1 at resolutions (a) 1.0°, (b) 0.5° and (c) 0.25°. Cases 2 and 4 use the new (diluted) CAPE calculation.

the grid spacing of 0.25°.

Due to the idealized nature of this study (i.e. no vertical wind shear, no background flow, constant SSTs, etc.) it is difficult to judge which path (CAM 4 or CAM 3.1) to development is more accurate. *Kaplan and Demaria* (2003) stated that 83% of all category 4 and 5 hurricanes from 1989 to 2000 underwent rapid intensification, defined to be a wind speed increase of 15.4 m $s^{-1}$ over a 24 hour period, at least once. At 0.25° both the CAM 3.1 and CAM 4 cyclones reach category 4 strength, yet only the CAM 4 simulation undergoes rapid intensification, with an increase of about 27.4 m $s^{-1}$ from day 1 to 2. However, this magnitude of rapid intensification is rare. Of the 2621 cases explored in *Kaplan and Demaria* (2003) only 7 were events with increases greater than 27 m $s^{-1}$ over a 24 hour period. While the CAM 3.1 cyclone never classifies as undergoing rapid intensification, its largest increase of 14.4 m $s^{-1}$ from day 7 to 8 is close to the threshold and might be more typical.

### 3.4.2 Analysis of the changes in the deep convection scheme

The impact of the individual enhancements to CAM 4 on the evolution of the initial vortex can be investigated by turning them off and on. Figure 3.2 displays that when the dilute CAPE calculation enhancement is turned off (case 3) no tropical cyclone develops at 1.0°. At the 0.5° and 0.25° resolutions the intensification of the initial vortex is significantly altered when compared to the full CAM 4 simulations. The case 3 storm develops in a similar manner to that of the CAM 3.1 (case 1) storm. Figure 3.2 also shows that the CAM 4 without CMT (case 4) simulations are rather similar to the full CAM 4 versions (case 2) with some minor changes in the evolving storm's strength and intensification.

Figure 3.3 provides insight into the impact of the individual enhancements in CAM 4 on the tropical cyclone structure. It depicts the longitude-height cross section of the magnitude of the wind through the center latitude of the vortex at day 10 for 0.25°

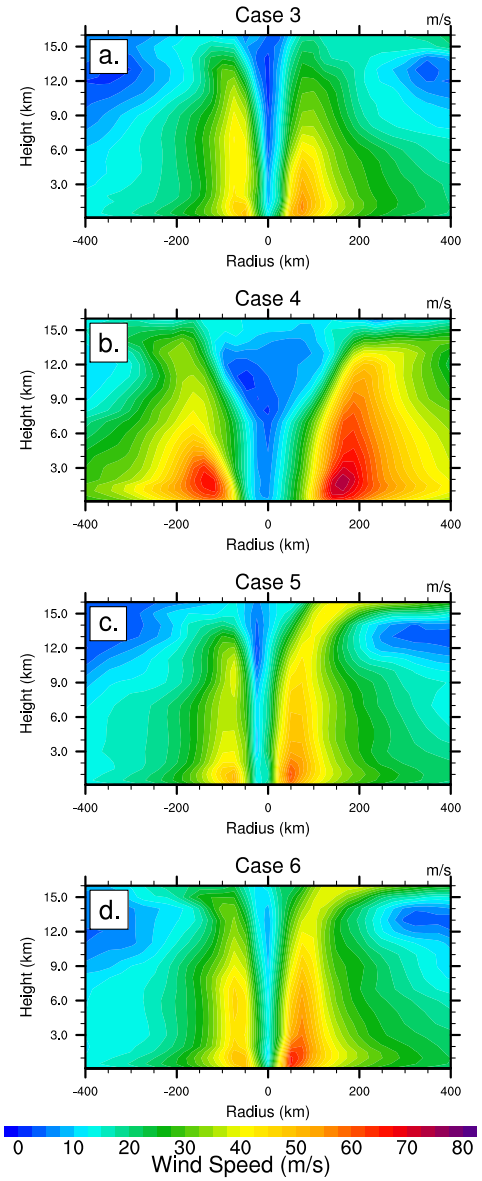


Figure 3.3: Snapshot of the longitude-height cross section of the wind speed through the center latitude of the tropical cyclone as a function of the radius from the vortex center at day 10. Results at 0.25° resolution for (a) case 3: CAM 4 physics with the CAM 3.1 undilute CAPE calculation, (b) case 4: CAM4 without CMT, (c) case 5: CAM 4 with the CAM 3.1 undilute CAPE calculation and without CMT and (d) case 6: case 5 with the additional modification to the cloud macrophysics.

simulations of case 3 through case 5. The enhanced outward-pointing radial slope of the wind speed contours only appears in case 4, and resembles the full CAM 4 physics simulation (case 2 as seen in Fig. 3.1f). This is again an indication that the dilute CAPE calculation significantly alters the structure of the tropical cyclone. It also suggests that the changes in structure from CAM 3.1 to CAM 4 are systematic and robust rather than random fluctuations. Note that when both CAM 4 enhancements are turned off (case 5) the simulations have resemblance to case 3 as shown in Figs. 3.2 and 3.3a,c.

The results demonstrate that the way in which CAPE is calculated in CAM 4 has a larger impact on the differences between the full CAM 3.1 and CAM 4 simulations than does the addition of CMT. Since these two enhancements are the main differences between CAM 3.1 and CAM 4 we would expect the CAM 3.1 physics simulation (case 1) and the CAM 4 run without enhancements (case 5) to be almost identical. However, this is not the case. Figures 3.2b,c show that case 5 is always weaker in magnitude by day 10 in comparison to case 1.

### 3.4.3 Impact of cloud macrophysics

The above mentioned difference is associated with an additional change in the cloud fraction state that is provided to the cloud macrophysics scheme. Namely, the cloud macrophysics scheme expects the atmospheric state from the previous time-level. In CAM 3.1 the cloud macrophysics scheme is provided the previous time-level state for all variables except the cloud fraction. This approach is corrected in CAM 4. Case 5 is altered to reproduce the manner in which CAM 3.1 handles the cloud macrophyics in CAM 4 (referred to as case 6). With this additional modification to the cloud macrophysics the results for case 6 (Fig. 3.3d) are now more comparable to the CAM 3.1 physics simulation in Fig. 3.1c (case 1) than are those of case 5. This is evidenced by the increase in the wind speed throughout the entire storm, including

the maximum wind speed, in case 6. It verifies that the main differences from CAM 3.1 to CAM 4 are due to changes in the physics suite. It is not expected that the case 1 and case 6 simulations match exactly since there are numerous other minor modifications in CAM 4.

## 3.5 Concluding remarks

Changes in physical parameterizations within the same model have a profound impact on the simulation of tropical cyclones. This paper shows that the development of the initial vortex into a tropical cyclone is significantly impacted by the choice of CAM 3.1 and CAM 4. For example, CAM 4 simulations produce a tropical cyclone in the 1.0° resolution case, whereas the cyclone in CAM 3.1 fails to develop. In addition, the CAM 4 simulations intensify earlier (after 1 day) and produce a stronger storm by day 10 when compared to the same CAM 3.1 simulations at the 0.5° and 0.25° grid spacings. It remains unclear as to which physics version produces a more realistic evolution of the very idealized tropical cyclone. By toggling the individual enhancements to the *Zhang and McFarlane* (1995) deep convective parameterization introduced in CAM 4, it is evident that the new manner in which CAPE is calculated is largely responsible for the difference in the simulations. This enhancement in the CAPE calculation leads to the extreme rapid intensification of the initial vortex much earlier during the simulation, resulting in stronger and larger storms by day 10 at all horizontal grid spacings. The CAPE enhancement also appears to account for the difference in vertical structure of the tropical storm, as seen with the 0.25° simulations. An additional modification to the cloud macrophysics scheme is required to approximately match the CAM 3.1 and CAM 4 tropical cyclone simulations.

This paper sheds light on the impact that the relatively small differences between NCAR's CAM 3.1 and CAM 4 have on idealized tropical cyclones. Even larger differences could be expected when comparing GCMs with very different physical parame-

terizations suites, like CAM version 5. In future work, we will perform similar studies that investigate the impact of different physics suites on the tropical cyclone development, intensity and structure. In addition, the effect of different GCM dynamical cores will be explored using identical physical parameterizations.

# CHAPTER IV

# Assessing the uncertainty of tropical cyclone simulations in NCAR's Community Atmosphere Model

## 4.1 Introduction

With the advancement of modern parallel computer architectures, general circulation models (GCMs) are becoming capable of running operationally at higher horizontal resolutions than ever before. At horizontal resolutions of 0.5° (roughly 55 km near the equator) or finer, various GCMs have been successful at simulating tropical cyclones or tropical cylone-like vortices. Examples include the simulations by *Atlas et al.* (2005), *Shen et al.* (2006a,b), *Oouchi et al.* (2006), *Bengtsson et al.* (2007), *Zhao et al.* (2009), *Wehner et al.* (2010) or *Reed and Jablonowski* (2011a,b). Over the coming decade the use of GCMs to simulate tropical cyclones is likely to become even more prominent. This is partly due to the forthcoming unified modeling approaches that aim at bridging the classical scale discrepancies between weather and climate models (*Palmer et al.*, 2008; *Hurrell et al.*, 2009). Emerging trends like models with variable-resolution meshes (*Baer et al.*, 2006; *Jablonowski et al.*, 2009; *Weller et al.*, 2009; *Ringler et al.*, 2011) will enable future-generation GCMs to seamlessly embed high-resolution regions within the global domain. These will allow GCMs

to compete with limited-area models traditionally used for tropical cyclone studies, and, equally important, provide a pathway for nonhydrostatic GCM modeling. This raises questions concerning the fidelity of GCMs for tropical cyclone assessments. In particular, it is unclear whether the designs of the underlying GCM dynamics and physics packages are adequate to reliably represent extreme storms. Answering such questions demands a targeted and systematic analysis approach. Here, we focus on an assessment of an ensemble of deterministic tropical cyclone simulations to gain insight into forecast uncertainties.

Simulations of climate and weather are inherently uncertain, and a single deterministic forecast without an uncertainty estimate has therefore limited significance. A key aspect to understanding the ability of GCMs to simulate tropical cyclones is to recognize the impact of various types of uncertainties. GCM simulations are susceptible to uncertainties in both the initial state and the model formulation itself, due to the strong nonlinearity of the climate system (*Palmer*, 2001). The main errors in GCM predictions are twofold. There are uncertainties in the initial conditions and boundary data that are a result of uncertain measurements and the data assimilation system. In addition, there are uncertainties within the model due to the temporal and spatial limitations of GCMs and the inability of GCMs to simulate every exact detail of the climate system (*Palmer*, 2000; *Stainforth et al.*, 2007). These limitations can be manifested within both the dynamical core (the resolved fluid flow component) and the physical parameterizations. The latter approximate the effects of the unresolved processes on the resolved scales and mimic processes such as precipitation, convection or radiation. In the study here, we focus on the quantification of the parameter and structural uncertainties that arise from different resolutions and physical parameterizations, and compare these to initial-data uncertainty estimates.

It is common to address uncertainties in the initial conditions by performing ensemble simulations that introduce perturbations in the initial state. Examples of this

technique and its application to tropical and extratropical cyclones are discussed in *van Sang et al.* (2008) and *Zhu and Thorpe* (2006), respectively. In addition, both the dynamical core and the physical parameterizations exhibit parameter and structural uncertainties. Examples of parameter uncertainty within an individual GCM encompass different physical constants, the choice of the tuning parameters in the physical parameterizations, or the selection of diffusion coefficients in the dynamical core. Relevant GCM ensemble studies include *Murphy et al.* (2004), *Stainforth et al.* (2005) and *Doblas-Reyes et al.* (2009), as well as the dynamical core assessments by *Jablonowski and Williamson* (2011). Examples of structural uncertainty incorporate model discrepancies due to different spatial resolutions, different dynamical cores or physical parameterizations. Such assessments can either be performed within an individual GCM when using model variants as in *Reed and Jablonowski* (2011b), or they rely on multi-model ensembles as e.g. presented in *Lauritzen et al.* (2010). A prominent multi-model ensemble approach is used by the Intergovernmental Panel on Climate Change (IPCC) (*Meehl et al.*, 2007).

The goal of the paper is to evaluate the impact of uncertainties on the simulation of a tropical cyclone-like vortex within an individual GCM. In particular, we utilize the National Center for Atmospheric Research's (NCAR) Community Atmosphere Model (CAM) with a variant of the aqua-planet setup (*Neale and Hoskins*, 2000). An analytic initialization technique is used to simulate the development of a single, initially weak vortex into a tropical cyclone (*Reed and Jablonowski*, 2011a). We evaluate the uncertainty of perturbations to the idealized initial conditions and the model parameters using versions 4 and 5 of CAM (*Neale et al.*, 2010a,b). The study thereby sheds light on the impact of the initial-data, parameter and structural uncertainties as they pertain to the development of the specific initial vortex. In general, another source of uncertainty is due to external forcings and boundary data, such as the solar variability, the aerosol distribution, soil characteristics and land use,

or sea surface temperatures (SSTs). However, such uncertainties do not apply to the idealized aqua-planet configuration used here, and are therefore not assessed. We note that our model setup is more idealized than that used for full climate or realistic tropical cyclone assessments, which might lead to a lower bound (or potential underestimation) of the uncertainty estimate. However, this represents a deliberate approach to more clearly isolate the causes and effects of the GCM modeling choices and their uncertainties as they relate to extreme storms. The idealized cyclone also removes the dependence on case-specific conditions that real cyclones exhibit.

The paper is structured as follows. A description of both model versions, CAM 4 and CAM 5, and the differences between them is presented in Section 4.2. Section 4.3 provides a brief overview of the analytic initial conditions and the design of the experiments. The evolution of the unperturbed control case simulation of the initial vortex using both CAM 4 and CAM 5 is examined in Section 4.4. Section 4.5 investigates the ensemble simulations and evaluates the initial-data and parameter uncertainties. Section 4.5 also includes a discussion of the differences between the two model versions at the varying resolutions and the impact of structural uncertainties. Section 4.6 presents the conclusions and plans for future research.

## 4.2 Description of the model CAM in aqua-planet mode

Our study utilizes the two recently released versions CAM 4 (*Neale et al.*, 2010a) and CAM 5 (*Neale et al.*, 2010b). CAM 4 and CAM 5 are part of NCAR's Community Earth System Model (CESM) that is routinely used for climate change projections. Both versions of CAM are configured with the mass-conservative finite–volume (FV) dynamical core in flux-form (*Lin*, 2004) that is built upon a 2D shallow water approach in the horizontal direction. The vertical discretization follows a "Lagrangian control-volume" principle, which is based on a terrain-following "floating" Lagrangian coordinate system and a fixed "Eulerian" reference frame. In particular,

the vertically-stacked volumes are allowed to float for several sub-cycled dynamics time steps before they are mapped back to fixed reference levels. The advection algorithm makes use of the monotonic Piecewise Parabolic Method (PPM) with an explicit time-stepping scheme (*Lin and Rood*, 1996). A regular latitude-longitude computational mesh is selected that includes both pole points. The prognostic variables are staggered as in the Arakawa-D grid.

The two CAM model configurations in aqua-planet mode are tested at the longitudinal and latitudinal resolutions $\Delta\lambda = \Delta\varphi = 1.0°$, $0.5°$ and $0.25°$. These three horizontal resolutions correspond to grid spacings of about 110 km, 55 km and 28 km in the equatorial region. Note that we use the terms resolution and grid spacing interchangeably in this paper. The corresponding dynamics time steps are 180 s, 90 s and 45 s, respectively. The physics time step is ten times the dynamics time step. All simulations are run for ten simulation days. The vertical resolution depends on the model version. CAM 4 utilizes its default 26 vertical levels (L26), while the CAM 5 default simulations use 30 vertical levels (L30). The model top is approximately at 2 hPa in both versions of CAM. All of the additional four model levels in CAM 5 are below 700 hPa to accommodate a new boundary layer parameterization scheme in CAM 5. This increases the number of full model levels between 700 hPa and the surface from five in CAM 4 to nine in CAM 5. The location of the vertical model levels is determined by the default configurations of CAM. The physical parameterizations in CAM 4 and CAM 5 are known to be sensitive to the level placement (especially the boundary layer and shallow convection schemes) so that CAM 4 cannot be run with 30 vertical levels.

The simulations with both the CAM 4 and CAM 5 physics suites utilize the aqua-planet setup as proposed by *Neale and Hoskins* (2000), but with constant sea surface temperatures of 29 °C. These isothermal SSTs prescribe very warm ocean conditions and avoid latitudinal gradients in the initial background surface pressure

or atmospheric temperature fields. The only external forcing is the distribution of the insolation at the top of the atmosphere. In particular, the solar irradiance is set to equinox conditions with a solar constant of 1365 W $m^{-2}$. In addition, the zonally symmetric distributions of atmospheric constituents, such as ozone, carbon dioxide, methane, and nitrous oxide are prescribed and symmetrized about the equator. Furthermore, the geophysical constants, including the earth's rotation rate and gas properties are prescribed in the aqua-planet experiment. We use these prescribed physical constants, except for the CAM default values for gravity and the Earth's radius. The latter two will be tested against the aqua-planet default constants to estimate the parameter uncertainty in an ensemble approach (see section 4.3.2).

### 4.2.1 CAM 4 physics suite

The CAM 4 physics suite is described in detail in *Neale et al.* (2010a). CAM 4 incorporates the *Zhang and McFarlane* (1995) deep convective parameterization and the *Hack* (1994) shallow moist convection scheme. The *Zhang and McFarlane* (1995) deep convective parameterization includes a dilute entraining plume (*Neale et al.*, 2008) and Convective Momentum Transport (CMT) in CAM 4 (*Richter and Rasch*, 2008). The physics package also includes the dry boundary layer turbulence scheme by *Holtslag and Boville* (1993), in addition to parameterizations of cloud microphysics, cloud macrophysics, orographic gravity wave drag, the radiative effects of aerosols and parameterizations of shortwave and longwave radiation. All of the CAM 4 physics runs use the identical physics tuning parameter set derived for CAM 4 climate simulations with the FV dynamical core at the 1.0° resolution as documented in *Neale et al.* (2010a).

### 4.2.2 CAM 5 physics suite

The CAM 5 physics package, documented in *Neale et al.* (2010b), is substantially different than the CAM 4 physics suite. While CAM 5 uses the same *Zhang and McFarlane* (1995) deep convective parameterization, the *Hack* (1994) shallow convection scheme is replaced by the University of Washington (UW) scheme (*Park and Bretherton*, 2009). The dry *Holtslag and Boville* (1993) turbulence scheme is replaced by the moist boundary layer turbulence scheme of *Bretherton and Park* (2009). However, CAM 4 and CAM 5 share the same surface flux parameterizations which are an important driver for tropical cyclones. In CAM 5 major changes were implemented in the cloud macrophysics, cloud microphysics and radiation schemes. The CAM 5 version used in this particular study contains a so-called Bulk Aerosol Model that we utilize with prescribed aerosols to mimic the aqua-planet setup of CAM 4 as closely as possible. We do not activate the default Modal Aerosol Model which includes prognostic aerosols. Similar to the CAM 4 simulations, an identical physics tuning parameter set from CAM 5 climate simulations with the FV 1.0° dynamical core is selected for all CAM 5 simulations. Note that these tuning parameters are not documented in *Neale et al.* (2010b). The variant of CAM 5 used in this study is a recent configuration (CAM 5.0.45 from February 2011) that will closely resemble a forthcoming release CAM 5.1.

## 4.3 Simulation design

### 4.3.1 Initial conditions of the control vortex

The analytic initialization technique for the tropical cyclone simulations is described in detail in *Reed and Jablonowski* (2011a). The initialization of the vortex is built upon prescribed 3D moisture, pressure, temperature and velocity fields that are embedded into tropical environmental conditions. The moisture and temperature

profiles and surface pressure of the background environment fit the observed mean hurricane season sounding for the Caribbean from *Jordan* (1958). The background surface temperature is set to match the SST of $T_0 = 302.15$ K or 29 °C and the background surface pressure is set to $p_0 = 1015.1$ hPa. The global background wind and therefore the background wind shear are zero. In addition, the topography is set to zero as required in aqua-planet experiments.

In all cases we initialize the model with a single, initially weak, warm-core vortex. The vortex has a radius of maximum wind (RMW) of about 250 km and a 20 m $s^{-1}$ maximum initial wind speed located at the surface. The vortex is in hydrostatic and gradient-wind balance in an axisymmetric form. Figures 4.1(a-c) show the horizontal cross sections of the initial wind speed at a height of 100 m, the surface pressure and the temperature at a height of 4.35 km. The latter corresponds to the altitude of the maximum (warm-core) temperature perturbation, which is about 3 K. The surface pressure minimum of 1003.85 hPa is in the center of the storm. Figures 4.1(d-f) depict the longitude-height cross sections of the magnitude of the wind, the pressure perturbation and the temperature perturbation through the center latitude of the vortex. The pressure perturbation is greatest at the center and surface of the initial vortex and the maximum temperature perturbation occurs at a height of 4.35 km at the center of the vortex. CAM 4 and 5 use the hybrid $\sigma$-pressure coordinate, i.e. the so-called $\eta$-coordinate (*Simmons and Burridge*, 1981). Since the analytic initial conditions are provided in height coordinates they are converted to the pressure-based system by straightforward fixed-point iterations in the vortex-covered region (*Reed and Jablonowski*, 2011a).

### 4.3.2 Composition of the ensemble members

The ensemble simulations consist of 39 runs with each version of CAM for a total of 78 model simulations in this study. This corresponds to 13 individual runs at each

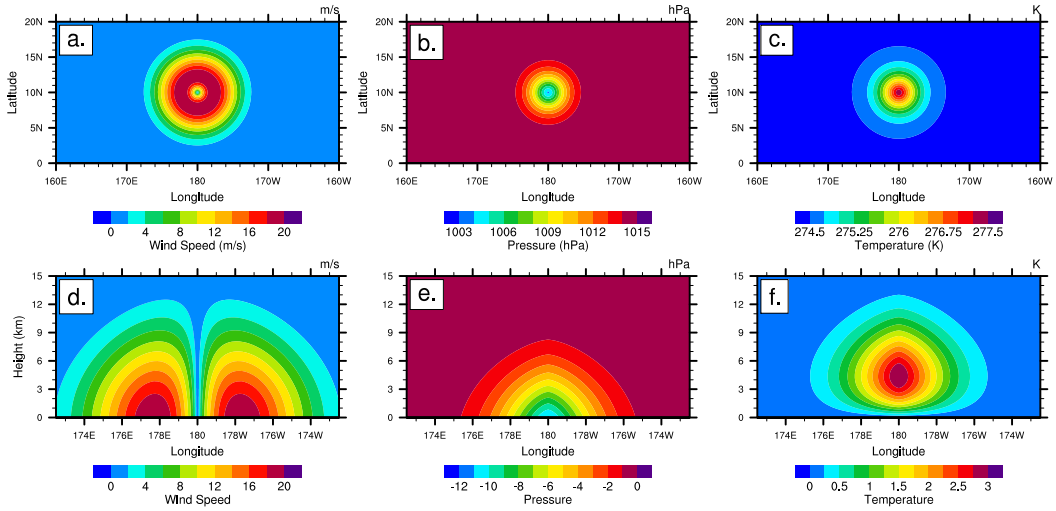


Figure 4.1: Horizontal cross sections of the (a) initial wind speed at a height of 100 m, (b) surface pressure and (c) temperature at a height of 4.35 km. Initial longitude-height cross sections of the (d) wind speed, (e) pressure perturbation and (f) temperature perturbation though the center latitude of the vortex at 10°N. The maximum wind speed is 20 m $s^{-1}$ with an RMW of 250 km.

horizontal resolution of 1.0°, 0.5° and 0.25°. These 13 simulations at each resolution for each CAM version are separated into four different sets:

1. The first set is the unperturbed control case. The initial data are identical to the idealized initial conditions described in section 4.3.1 (*Reed and Jablonowski*, 2011a).

2. The next set consists of eight simulations. They are initialized with the control vortex that is then overlaid with random small-amplitude perturbations of the initial zonal and meridional wind velocities. The random perturbations are implemented globally and lie within the range of ±2% of the initial wind speed at any given location. This accounts for a change in the zonal and meridional wind velocities of at most ±0.4 m $s^{-1}$.

3. The third set of runs are two simulations in which the longitudinal position of the center of the unperturbed control vortex is shifted by $\Delta\lambda/2$ and $\Delta\lambda/4$.

This shift in the initial location of the vortex produces small variations in all initial fields, since they are analytically evaluated at the grid point locations and the center of the vortex now no longer coincides with a CAM grid point. This mimics the uncertainty related to the choice of the computational grid as different models on e.g. cubed-sphere or icosahedral meshes utilize very different grid point distributions. Note, that the latitudinal position of the vortex stays the same to guarantee identical Coriolis forces at the beginning of the forecast. The longitudinal shift acts as another metric to understanding the initial-data uncertainty.

4. The final set evaluates the parameter uncertainty. It consists of two simulations that start from the initial control vortex but utilize different physical constants in CAM. In the first simulation the physical constant for the gravity is switched from the CAM default (9.80616 m $s^{-2}$) to the aqua-planet default (9.79764 m $s^{-2}$). In the second simulation the model parameter for the radius of the Earth is switched from the CAM default ($6.37122 \times 10^6$ m) to the aqua-planet default ($6.371 \times 10^6$ m). These differences represent less than a $9.0 \times 10^{-2}$% and $3.5 \times 10^{-3}$% change in the physical constants for the gravity and the Earth's radius, respectively.

The differences between the simulations at different horizontal resolutions within the same version of CAM and the differences amongst the simulations of varying CAM versions shed light on the structural uncertainty of the idealized tropical cyclone experiments.

## 4.4 Evolution of the control vortex

In this section we provide the results for the CAM 4 L26 and CAM 5 L30 simulations in aqua-planet mode for the control case. First, the 10-day evolution of the

initial vortex into a tropical cyclone is investigated at the highest horizontal resolution 0.25°. Next, we provide a comparison of the control case at the three resolutions 1.0°, 0.5° and 0.25°. This investigation provides a basis for understanding the way in which the initial vortex develops into a tropical cyclone and how the choice of the horizontal resolution and the CAM version impacts this evolution.

### 4.4.1 Tropical cyclone evolution at 0.25°

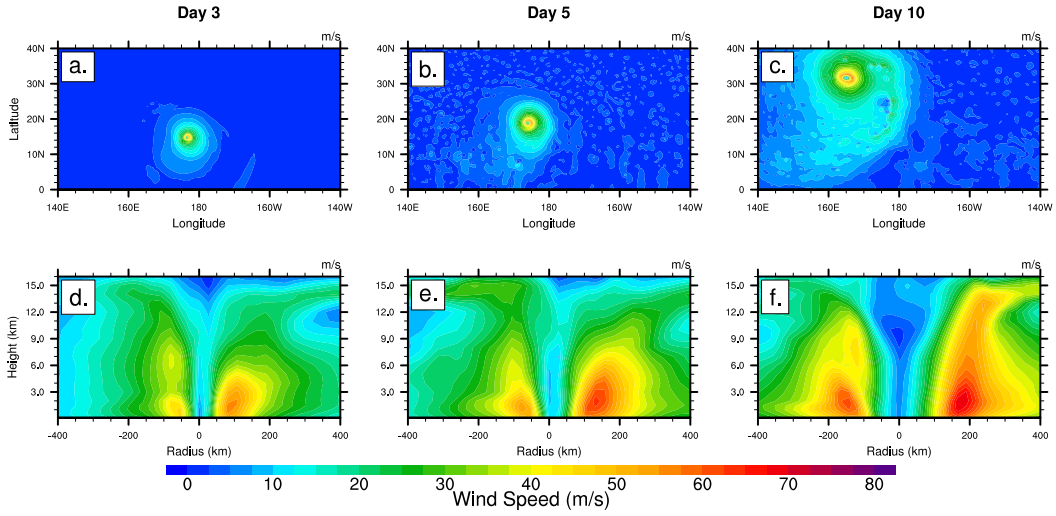


Figure 4.2: Snapshots of the tropical cyclone-like vortex at day 3 (left), 5 (middle) and day 10 (right) at the resolution 0.25° L26 for CAM 4 physics. Top row (a-c): horizontal cross section of the wind speed at a height of 100 m. Bottom row (d-f): longitude-height cross section of the wind speed through the center latitude of the vortex as a function of the radius from the vortex center. The initial maximum wind is 20 m $s^{-1}$ with an RMW of 250 km. The center position is (165.0°E, 31.5°N) at day 10.

The evolution of the unperturbed control vortex in CAM 4 L26 is explored at the horizontal grid spacing $\Delta\lambda = \Delta\varphi$ =0.25° to verify its tropical cyclone-like characteristics. Figure 4.2 shows the development of the wind speed for the control case, with specific snapshots at days 3, 5 and 10 (a snapshot at day 0 is provided in Fig. 4.1(a) and Fig. 4.1(d)). The top row (a-c) of Fig. 4.2 displays the horizontal cross section of the magnitude of the wind at 100 m. The bottom row (d-f) of Fig. 4.2 shows the longitude-height cross section of the magnitude of the wind through the center

latitude of the vortex. The 100 m wind speed is determined via a linear interpolation using the two surrounding model levels. We define the center of the vortex to be the grid point with the minimum surface pressure. The time series displays the intensification of the vortex from an initial surface vortex to a strong tropical cyclone. Throughout the evolution the vortex experiences the beta-drift towards the north-west (*Holland*, 1983). By day 10 the maximum wind speeds are near the surface (approximately 1 to 2 km in height) and the RMW is roughly 150–200 km. The 100 m maximum wind speed at day 10 of 58.39 m $s^{-1}$ is equivalent to a very strong category-3 hurricane on the Saffir-Simpson scale. During the simulation the cyclone maintains a relatively calm eye. The cyclone has an area of vertical development near the RMW, where the contours of constant wind speed start to slope more outward at higher altitudes (above 9 km). The cyclone is a warm-core vortex (not shown).

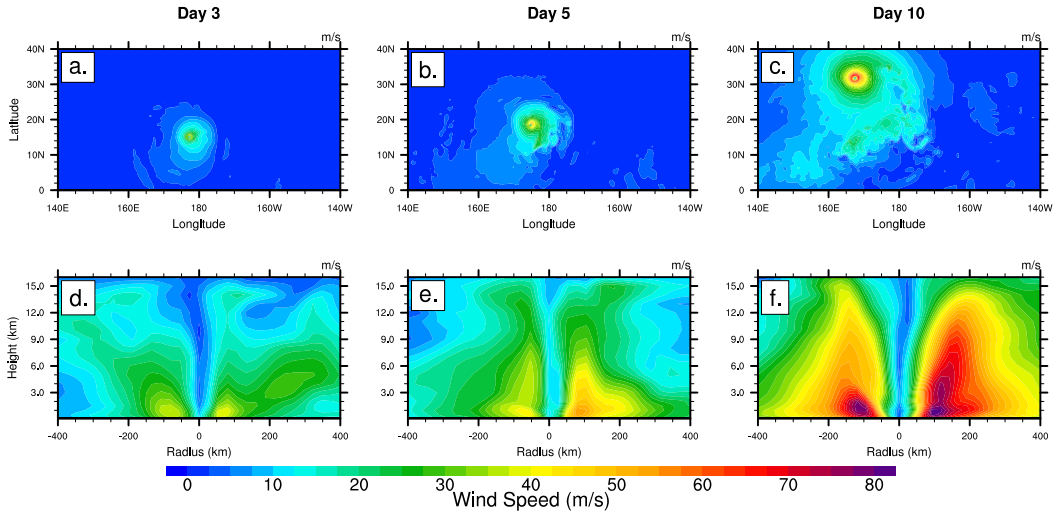


Figure 4.3: Same as Fig. 4.2, but for CAM 5 physics with L30. The center position is (167.5°E, 31.75°N) at day 10.

The evolution of the initial vortex is also investigated for the CAM 5 L30 control case simulation. Figure 4.3 is the same as Fig. 4.2, but for the CAM 5 0.25° simulation. By day 10 the maximum wind speeds are nearer to the surface than those in the CAM 4 simulation, at a height of roughly 0.5 to 1.5 km. This height of the maximum wind speeds in CAM 5 is comparable to observations of 0.5 to 1.0 km discussed in *Bell*

*and Montgomery* (2008) for Hurricane Isabel in 2003, and may be more realistic than CAM 4. The RMW is roughly 100 km and the maximum wind speeds within the CAM 5 storms are noticeably stronger throughout the storm. The 100 m maximum wind speed at day 10 is 66.96 m $s^{-1}$ and equates to a strong category-4 hurricane on the Saffir-Simpson scale. The differences in the RMW, maximum wind speed and height of the maximum wind speed are likely linked to the thermodynamic structure of the storms. As shown later, the relative humidity profiles in the eyewall differ for CAM 4 and CAM 5.

Despite the CAM 5 storm becoming more intense than its CAM 4 equivalent by day 10, at days 3 and 5 the CAM 5 storm is overall weaker and less organized. This is evidenced by weaker wind speeds and less pronounced vertical development of the storm at days 3 and 5. This suggests that the exact path of development from the initial vortex into a tropical cyclone is specific to the choice of the CAM version. This is further evidenced by the fact that between days 1 and 2 a mid-level vortex forms and intensifies in CAM 5 (not shown), very similar to the cyclone development using a higher resolution limited-area model approach shown in *Nolan* (2007). The formation of the mid-level vortex before the smaller-scale, near-surface vortex shown in Fig. 4.3(d) is not observed in CAM 4 and seems to delay the intensification of the storm in CAM 5 when compared to CAM 4. Such differences among model versions have also been observed by other studies such as *Reed and Jablonowski* (2011b). Similar to the CAM 4 simulation the CAM 5 cyclone maintains a relatively calm eye during the length of the 10-day simulation. Also, the background environment of the CAM 5 control simulation appears to be much calmer than that of the CAM 4 simulation and may provide insight as to why the two CAM versions are simulating different intensities. This could be a result of the different boundary layer and shallow convection parameterizations that likely have a profound impact on the vertical mixing and the wind speeds at the lower levels of the troposphere. We note again

that the surface layer and deep convection parameterizations are identical in both CAM versions.

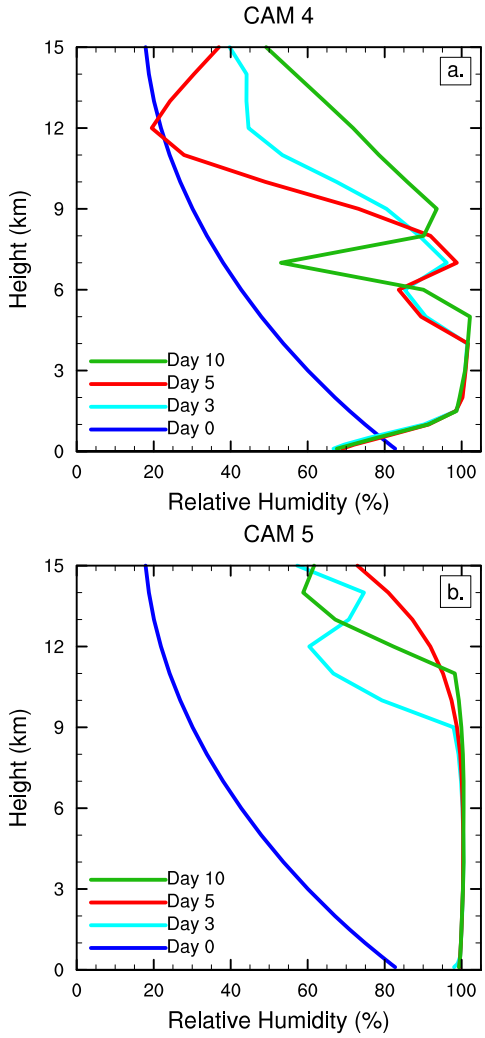


Figure 4.4: Relative humidity profiles at the location of 100 m wind maximum at days 0, 3, 5 and 10 for the control case simulation at the resolution 0.25° for (a) CAM 4 and (b) CAM 5.

Figure 4.4 shows the evolution of the vertical relative humidity profile at the location of the 100 m wind maximum at days 0, 3, 5 and 10 for (a) CAM 4 and (b) CAM 5 at the horizontal resolution of 0.25°. It is apparent from both the CAM 4 and CAM 5 simulations that the development of the vortex into a tropical cyclone coincides with a moistening of the troposphere, displayed as the relative humidity. However, there are distinct differences between the CAM 4 and CAM 5 simulations.

By days 5 and 10 almost the entire tropospheric profile up to 11 km in height is saturated or near saturation in the CAM 5 simulation. In contrast, the CAM 4 simulation only saturates the middle troposphere at heights of roughly 1.5 to 5 km by days 5 and 10. In fact, near the surface the relative humidity values at days 3, 5 and 10 are actually less than the initial values (day 0) in the CAM 4 run. These low relative humidity values in CAM 4 differ from observations of Hurricane Isabel in 2003. In *Montgomery et al.* (2006) it is shown that the lower troposphere (0 to 2 km) of Hurricane Isabel, an intense storm, is nearly saturated with fairly constant relative humidity values greater than 90% throughout the eyewall in this region. The relative humidity profile for the CAM 5 simulation follows more closely the observed profile in *Montgomery et al.* (2006) in the lower troposphere. It is expected that the differences shown in Fig. 4.4 are related to the differences in the wind structure discussed earlier, namely that the CAM 4 simulation is weaker with the region of maximum wind speeds being slightly higher than in the CAM 5 simulation.

The differences in the relative humidity profiles suggest that the different boundary layer and shallow convection schemes, as well as the corresponding differences in the vertical resolution, play a large role in the differences in intensity of the storm from CAM 4 to CAM 5, as these schemes are crucial to the moisture content in the troposphere (especially at lower levels). These processes are known to be important for the evolution of tropical cyclones in limited-area hurricane models (*Smith*, 2000; *Hill and Lackmann*, 2009a). We also recognize that tropical cyclones are sensitive to other physical parameterizations such as the microphysics and precipitation schemes (*Rogers et al.*, 2007) since an important source of energy for the evolution and maintenance of a tropical cyclone is the latent heat released by condensation. However, thorough analyses of the exact triggers of the structural uncertainties in the physical parameterizations (as in e.g. *Reed and Jablonowski* (2011b)) are beyond the scope of this paper and will the subject of future research. This paper is mainly focused on

the quantification of uncertainty as displayed by the two default versions of CAM at varying resolutions.

### 4.4.2 Resolution comparison

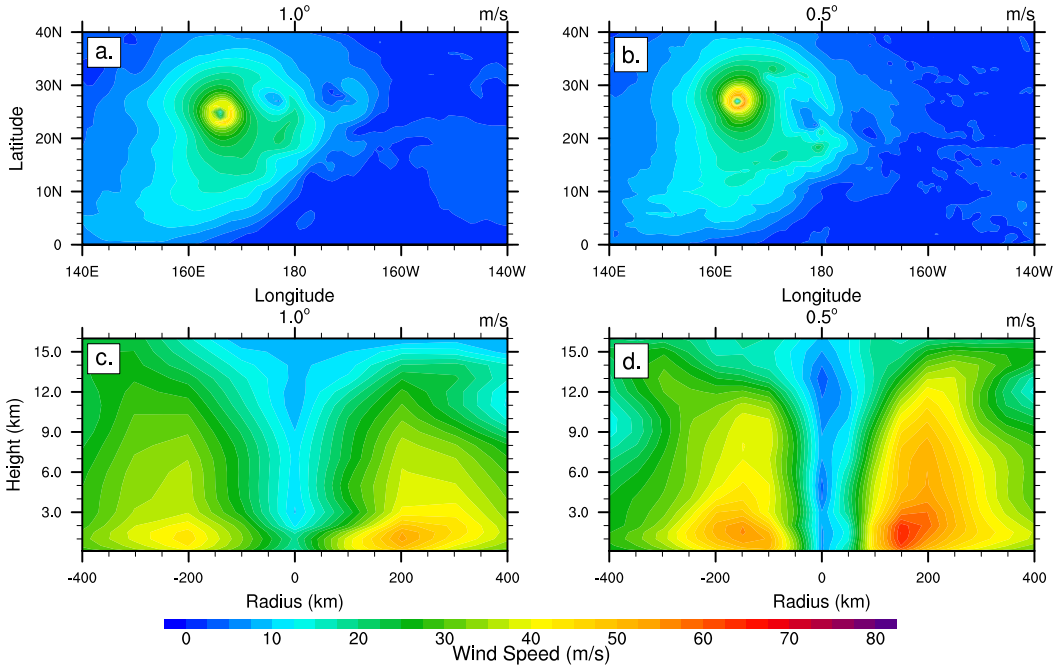


Figure 4.5: Snapshot of the tropical cyclone-like vortex at day 10 at the resolutions of 1.0° and 0.5° L26 for CAM 4 physics. Top row (a-b): horizontal cross section of the wind speed at a height of 100 m. Bottom row (c-d): longitude-height cross section of the wind speed through the center latitude of the vortex as a function of the radius from the vortex center. The center of the storm is located at (166°E, 25°N) and (164°E, 27°N) for the 1.0° and 0.5° simulations, respectively.

The impact of the horizontal resolutions on the intensity and structure of the control tropical cyclone simulation is investigated. Figure 4.5 displays the wind speed at day 10 for the CAM 4 1.0° and 0.5° L26 simulations. The top row (a,b) of Fig. 4.5 displays the horizontal cross sections of the magnitude of the wind at 100 m. The bottom row (c,d) of Fig. 4.5 shows the longitude-height cross sections of the magnitude of the wind through the center latitude of the vortex. As the resolution increases the storm becomes more organized, as evidenced by a more clearly defined eye and vertical

development of the storm. The storm also becomes more intense with larger wind speeds throughout the storm at increasing resolution. At the higher resolutions the storm starts to develop more fine-scale structures. This can be seen in Fig. 4.5(b) and in Fig. 4.2(c). While a tropical cyclone of the intensity of 46.12 m $s^{-1}$ develops in the 1.0° simulation, the storm is rather large in size, with an RMW of approximately 200 km.

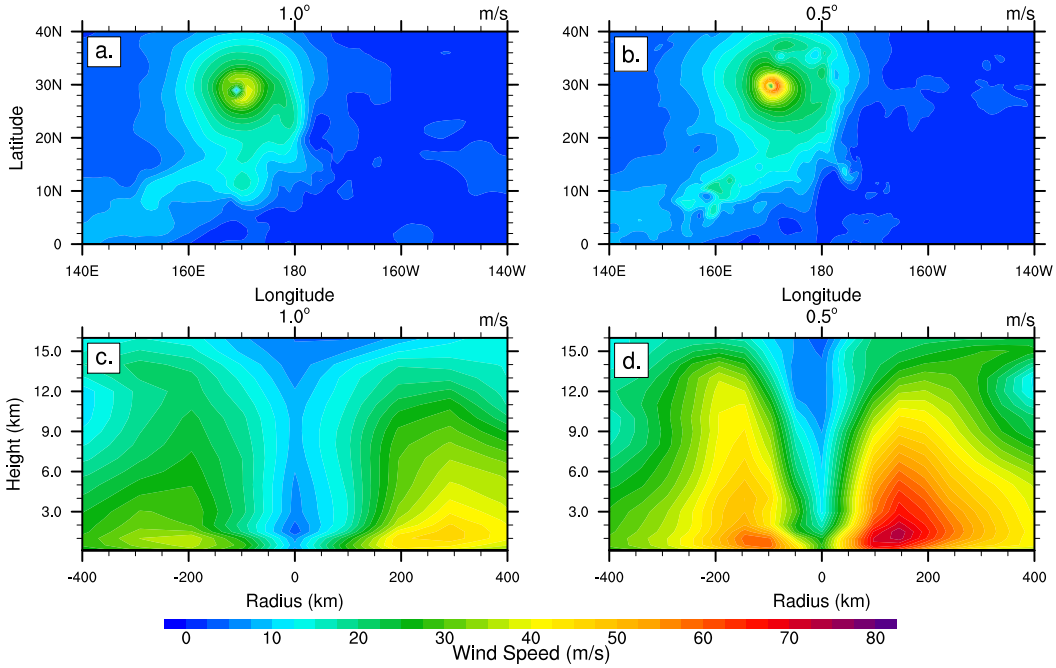


Figure 4.6: Same as Fig. 4.5, but for CAM 5 physics with L30. The center of the storm is located at (169°E, 29°N) and (170.5°E, 29.5°N) for the 1.0° and 0.5° simulations, respectively.

Figure 4.6 displays the wind speed at day 10 for the CAM 5 L30 simulations at 1.0° and 0.5°. As with CAM 4, Fig. 4.6 along with Fig. 4.3(c) show that the storm becomes more intense as the resolution increases, with larger wind speeds throughout the storm. Similar to the 0.25° resolution case the 0.5° CAM 5 control simulation is stronger than the CAM 4 equivalent. However, at 1.0° the maximum wind speed at 100 m is about 39.0 m $s^{-1}$ and the CAM 4 simulation is more intense. The RMW also appears to decrease with increasing resolution, while in the CAM 4 simulations the 0.5° and 0.25° have similar RMWs. Again a potential explanation of the differences

between the CAM 4 and CAM 5 becomes apparent in Fig. 4.6(d) near the top of the boundary layer. At day 10 the CAM 5 storm exhibits a sharper vertical gradient in the wind speed at a height of 2-3 km near the center of the storm (eyewall) where contours of constant wind speed rapidly slope radially outward toward the RMW. The CAM 4 simulation (Fig. 4.5(d)) produces a storm that has a smoother vertical transition of the wind speed in this region. These differences could be influenced by the differences in the boundary layer and shallow convection parameterization used in CAM 4 and CAM 5.

## 4.5 Ensemble simulations

This section presents the results of the 13 ensemble simulations for both CAM 4 and CAM 5 at each resolution. The results provide an understanding and quantification of the initial-data, parameter and structural uncertainties. The investigation also sheds light on the robustness of the results of the control case simulations discussed in Section 4.4. Figure 4.7 displays the time evolution of the maximum 100 m wind speed of the CAM 4 L26 ensemble runs and the control case at the horizontal resolutions (a) 1.0°, (b) 0.5° and (c) 0.25°. The control case is represented by the bold blue line, the eight runs with random perturbations to the initial wind speeds are represented by the red lines, the two runs with a variation of the initial longitude of the initial vortex are displayed as green lines and the two runs with changes in the model parameters are shown as black lines for each resolution. From Fig. 4.7 it is evident that there is a noticeable spread in the simulations. Figure 4.7 provides a sense of the randomness among the individual ensemble simulations and suggests that there is no clear distinction between the initial-data and parameter uncertainty. The deviations of these time series from the control run are of similar magnitude. Figure 4.7 also sheds light on the robustness and structural uncertainty of the control case in CAM 4 and its dependence on the resolution. The state that is produced

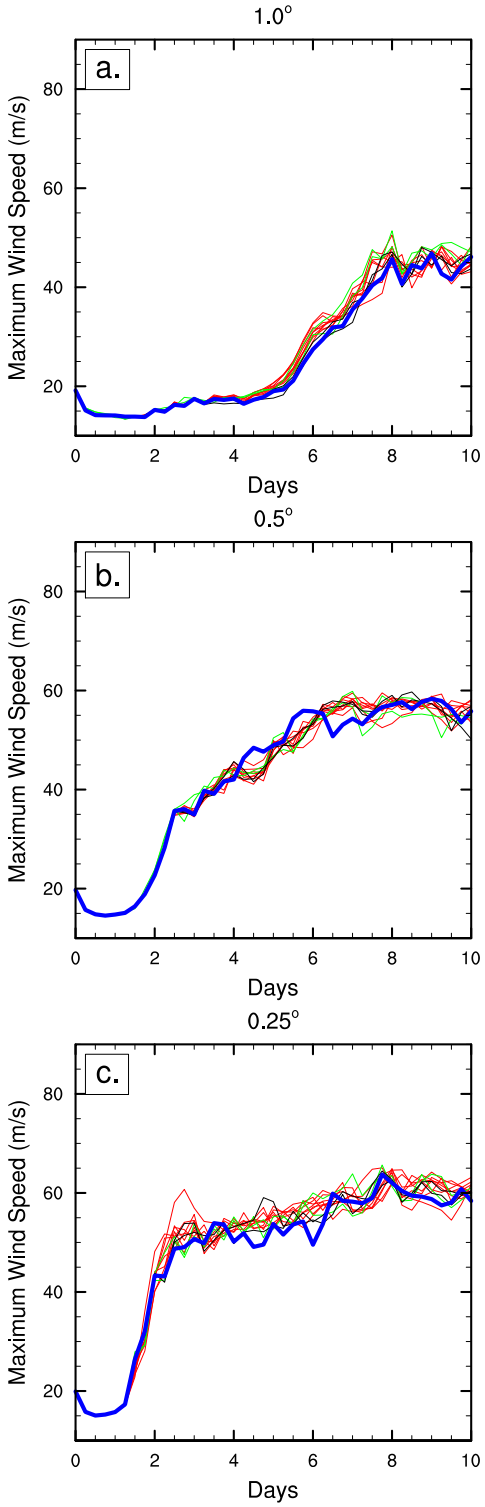


Figure 4.7: Time evolution of the maximum wind speed at 100 m of the ensemble simulations with CAM 4 at (a) 1.0°, (b) 0.5° and (c) 0.25°. The bold blue line represents the control case, the red lines represent the eight random runs with perturbations to the initial zonal and meridional wind speeds, the green lines represent the two runs with the shift in the initial center longitude of the vortex and the black lines represents the runs with differences in the model parameters.

by day 10 is significantly different depending on the horizontal resolution, especially at the 1.0° and 0.5° resolutions. However, the day-10 low-level wind speeds in the 0.25° simulations are only about 5 m $s^{-1}$ larger than the wind speeds in the 0.5° model runs, and the maximum intensities at both resolutions seem to have reached a plateau at days 7-10. This maybe can be interpreted as a sign of convergence in CAM 4. However, computationally-intensive higher-resolution simulations would be needed to confirm this assertion.

As the horizontal CAM 4 resolution increases from 1.0° to 0.25° the spread in the maximum 100 m wind speed occurs earlier in the simulation. In agreement with the results in Section 4.4 of the control case, Fig. 4.7 also shows that as the resolution increases so does the maximum wind speed at 100 m. Table 4.1 lists the maximum wind speed (MWS) at 100 m of the control simulation at day 10 for each resolution for both CAM 4 and CAM 5, as well as other ensemble characteristics such as the maximum absolute spread among the ensemble members, the root-mean-square deviations (RMSD) of 12 ensemble members (sets 2-4) to the control simulation at day 10, and the maximum RMSD during the 10-day simulation. The maximum absolute spread in the 100 m wind speed, defined as the maximum difference between two ensemble simulations during any one time in the simulations, occurs at the highest resolution of 0.25°. At all CAM 4 resolutions the absolute spread of the maximum low-level wind speed at day 10 is approximately 4–8 m $s^{-1}$ (Fig. 4.7). The maximum spread listed in Table 4.1 generally occurs earlier than day 10, mostly during the extreme intensification phase of the storm.

The corresponding CAM 5 L30 ensemble results are shown in Fig. 4.8. The figure again confirms that the noticeable spread in the 100 m wind speeds at a single resolution is unbiased and does not show a distinction between the initial-data and parameter uncertainty runs. The maximum spread in the maximum low-level wind speed occurs at the highest horizontal resolution 0.25°. At day 10 the CAM 5 1.0°

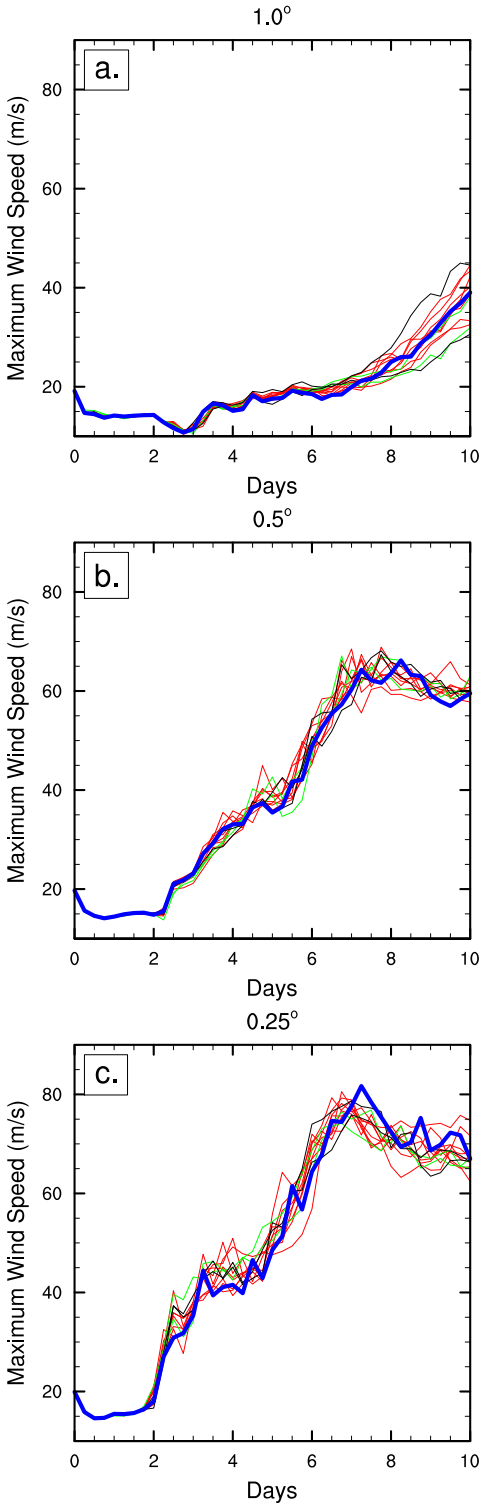


Figure 4.8: Same as Fig. 4.7, but for CAM 5 physics.

Table 4.1: Various ensemble characteristics for the maximum wind speed (MWS) at 100 m for the CAM 4 and CAM 5 simulations at 1.0°, 0.5° and 0.25°: MWS at day 10, maximum absolute spread among all ensemble members, root-mean-square deviations (RMSD) of 12 ensemble members (sets 2-4) to the control simulation at day 10, and the maximum RMSD during the 10-day simulation. All values have units of m $s^{-1}$.

CAM 4

| | Control MWS at day 10 | Max spread | RMSD at day 10 | Max RMSD |
|---|---|---|---|---|
| 1.0° | 46.12 | 10.09 | 1.79 | 4.38 |
| 0.5° | 55.82 | 8.81 | 2.13 | 5.60 |
| 0.25° | 58.39 | 13.75 | 2.64 | 7.51 |

CAM 5

| | Control MWS at day 10 | Max spread | RMSD at day 10 | Max RMSD |
|---|---|---|---|---|
| 1.0° | 39.02 | 15.51 | 4.90 | 4.90 |
| 0.5° | 59.53 | 11.85 | 1.67 | 5.40 |
| 0.25° | 66.96 | 17.17 | 3.03 | 7.66 |

ensemble simulations seem to have the greatest spread of approximately 14 m $s^{-1}$, while the 0.5° ensemble simulations exhibit a considerably smaller spread. Most likely this is due to the fact that the storms at 1.0° often do not fully develop during the 10-day simulations, and the small perturbations seem to tip the scales quite significantly. Therefore, the CAM 5 1.0° simulations are highly uncertain, and the control case does not seem to be a reliable representative of the evolution of the storm. As seen before, the higher-resolution CAM 5 simulations produce storms with higher maximum low-level wind speeds. The wind speeds are also more intense as the corresponding wind speeds in CAM 4 at 0.5° and 0.25°. In contrast to CAM 4 though, the wind speeds in CAM 5 do not tend to converge with increasing resolution. They also do not seem to oscillate steadily about a plateau around day 10. The maximum intensities in the 0.5° and 0.25° simulations reach their peaks earlier in the simulation around day 7 and seem to slowly decay afterwards.

Figure 4.9 represents the spread in the ensemble simulations of CAM 4 and CAM 5 for all resolutions in a different way. The evolution of the (a,b) minimum surface

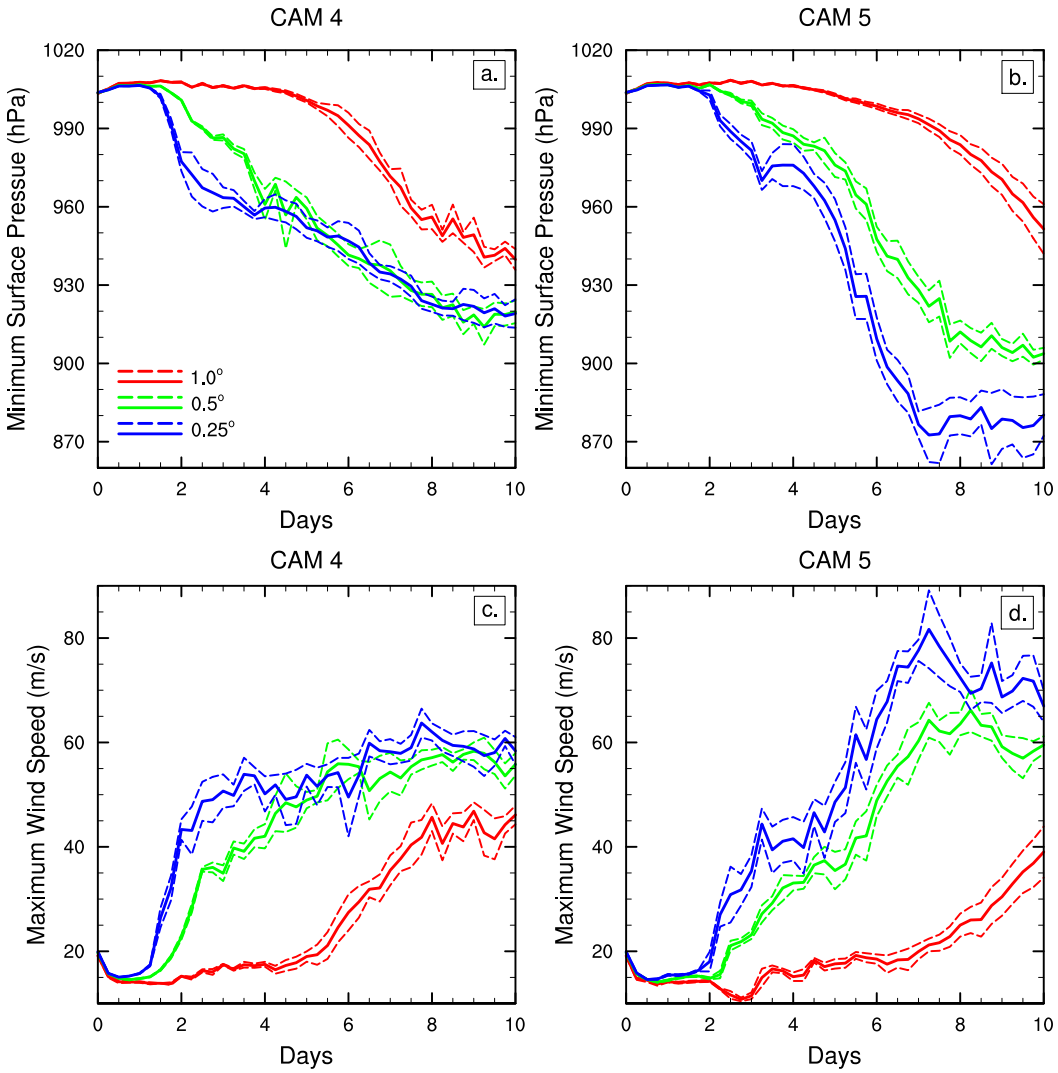


Figure 4.9: Time evolution of the minimum surface pressure (top row) and maximum wind speed at 100 m (bottom row) of the control case at the horizontal resolutions of 1.0° (red), 0.5° (green) and 0.25° (blue) with CAM 4 and CAM 5. The solid line represents the control case and the dashed lines represent that the variance as determined by the ensemble RMSD.

pressure and (c,d) the maximum 100 m wind speed for the control case are shown as the solid line and the dashed lines represent the ensemble RMSD from the control case at any given time. Figure 4.9 provides insight into the expected variance and thereby the uncertainty estimate of the control case simulation with respect to the initial-data and parameter uncertainties. As time progresses the uncertainties in the initial conditions and model parameters produce a spread, as represented by the ensemble RSMD, in the evolutions of the storms on the order of about 4-10 m $s^{-1}$ in the low-level wind speeds and about 4-15 hPa in the minimum surface pressures. The maximum spreads are even slightly higher. In both the CAM 4 and CAM 5 plots the initial noticeable deviations of the minimum surface pressure occur earlier in the simulation as the resolution increases from 1.0° to 0.25° (Figs. 4.9(a,b)). This is also true for the onset of the spread of the maximum 100 m wind speeds (Figs. 4.9(c,d)).

Figure 4.9 sheds light on the differences between the CAM 4 and CAM 5 simulations at the varying resolutions and, therefore, the structural uncertainty. When comparing the evolution of the minimum surface pressures (Figs. 4.9(a,b)) it is evident that the choice of the model version has a profound impact on the results. We observe that the structural uncertainty due to different physical parameterizations is of larger magnitude than other uncertainties discussed in this study. As shown in Section 4.4 the intensity of the CAM 5 storm is stronger than the CAM 4 storm at identical resolutions, except at 1.0°. This is evident by the much deeper minimum surface pressures by day 10 of the ensemble runs at 0.5° and 0.25° with CAM 5. This is also evident in the plots of the maximum 100 m wind speed (Figs. 4.9(c,d)). The differences in the CAM 4 and CAM 5 storm intensity are likely a result of the different boundary layer, shallow convection and other parameterizations as argued in Section 4.4.

Table 4.2 presents the minimum surface pressure of the control simulation at day 10 for each resolution and model version, in addition to other ensemble characteristics.

Table 4.2: Same ensemble characteristics as in Table 4.1 but now listed for the minimum surface pressure (MSP) of the CAM 4 and CAM 5 simulations at 1.0°, 0.5° and 0.25°. All values have units of hPa.

CAM 4

| | Control MSP at day 10 | Max spread | RMSD at day 10 | Max RMSD |
|---|---|---|---|---|
| 1.0° | 939.79 | 18.23 | 4.01 | 7.12 |
| 0.5° | 919.74 | 17.00 | 4.30 | 12.81 |
| 0.25° | 919.11 | 24.48 | 5.46 | 8.44 |

CAM 5

| | Control MSP at day 10 | Max spread | RMSD at day 10 | Max RMSD |
|---|---|---|---|---|
| 1.0° | 951.47 | 29.51 | 9.53 | 9.53 |
| 0.5° | 902.72 | 20.68 | 2.24 | 7.17 |
| 0.25° | 880.24 | 31.03 | 7.97 | 13.67 |

The results in Fig. 4.9 and Table 4.2 depict that the minimum surface pressure at day 10 in the CAM 5 control simulation at 0.25° is extremely low, and compares to some of the lowest surface pressures ever recorded within an observed tropical cyclone. This extreme intensity could be a result of the fact that the 1.0° physics tuning parameters are used at all horizontal resolutions in this study and there is no retuning at the higher resolutions. In addition, the idealized initial conditions place the vortex in a very moist and favorable background with no initial wind shear. The high intensity could therefore be fostered by the warm SST conditions and the abundance of sensible and latent heat at the surface. However, these extreme intensities are not observed in the CAM 4 simulations that experience the identical SST forcing. This provides hints that these structural differences and extreme intensities are likely an artifact of the CAM 5 model physics and the complex nonlinear interactions between the dynamical core and the physics parameterizations. One might argue that the intensities in the CAM 4 simulations might be more plausible. However, since no analytical solution exists, we cannot conclusively judge whether the CAM 4 or CAM 5 simulations are more realistic since extreme storms are indeed possible in this idealized environment according to the maximum intensity theory by *Emanuel* (1988). A more profound

judgement will rely on further intercomparisons with other models or other model variants.

From Tables 4.1 and 4.2 it is apparent that the largest spread in the ensemble for the minimum surface pressure and the maximum wind speed for both CAM versions occurs at the highest horizontal resolution. There seems to be little relation between the RMSD at day 10, the maximum RMSD throughout the 10-day simulation, and the model resolution for both CAM 4 and CAM 5. In addition, the ensemble RMSD is of the same order for the CAM 4 simulations as it is for the CAM 5 simulations.

Figure 4.9 also provides insight into the convergence-with-resolution characteristics. As mentioned before for CAM 4, the simulations appear to be similar at day 10 at 0.5° and 0.25°. This is suggested by the overlapping ensemble variance, represented as the RMSD, that occurs midway through the 10-day simulation. This result is not a characteristic of the CAM 5 simulations. In Fig. 4.9(b,d) there is no evidence of convergence as the resolution increases and the model produces completely different states without overlapping RMSD by day 10, regardless of the resolution. Clearly the choice of the CAM version, and therefore the model physics suite, has a significant impact on the intensification of the tropical cyclone as the dynamical core has remained the same in both versions.

## 4.6 Conclusions

An analytic tropical cyclone test case was implemented in order to assess the uncertainty of deterministic 10-day simulations using NCAR's CAM. At horizontal resolutions of 1.0°, 0.5° and 0.25° the initially weak vortex developed into a tropical cyclone using CAM 4 L26 and CAM 5 L30. The CAM 5 control vortex simulations at the horizontal resolutions of 0.5° and 0.25° produce stronger storms by day 10 when compared to the equivalent CAM 4 control cases. However, the CAM 4 control simulation generates a stronger storm than CAM 5 at 1.0°. The CAM 5 storms

also develop different vertical structures near the eyewall at the top of the boundary layer and significantly different vertical relative humidity profiles at the RMW in comparison to CAM 4. While there are intensity and structural differences between the two CAM variants, both produce storms with tropical cyclone-like characteristics, such as a warm core. Thus the idealized vortex initialization technique can be used as a tool to test and evaluate the uncertainty of tropical cyclone-like storms within CAM or other GCMs.

Through a series of 78 model ensemble simulations three different forms of uncertainty are assessed, including the initial-data, parameter and structural uncertainties. Each ensemble at each resolution consists of 13 different simulations that include the control case. Ten ensemble members provide small-amplitude perturbations to the initial control vortex and two simulations assess the impact of altered model parameters. In particular, the physical constants for the gravity and the radius of the Earth are slightly modified. The ensemble simulations reveal the significant variations in the evolution of the tropical cyclone. Using common metrics of minimum surface pressure and maximum low-level wind speed it is shown that there is no systematic difference in the ensemble simulations when comparing the initial-data and parameter uncertainties. The majority of the uncertainty depends on two main factors: the horizontal resolution and the version of CAM. The uncertainty in the simulation results, as measured by the ensemble RMSD from the control simulation, is on the order of 1-5 m $s^{-1}$ and 2-10 hPa for the maximum wind speed and for the minimum surface pressure at day 10, respectively. However, the maximum RMSD and absolute spread are slightly bigger and often occur before model day 10 during the rapid intensification phases. In general, the ensemble simulations shed light on the variance in the control case simulation and on the robustness of such simulations in CAM. It is important that this variance is taken into account when comparing and contrasting results of the tropical cyclone test case in different models in the future. The aim of the study

was to quantify the uncertainty estimate for a particular tropical storm in CAM with special focus on the initial-data, parameter and structural model uncertainties. The latter arose from two different physical parameterization suites and different spatial resolutions. However, this uncertainty estimate might still underestimate a possible ensemble spread since other structural model uncertainties such as the choice of a different dynamical core have not been included in this assessment yet.

The ensemble simulations using both CAM 4 and CAM 5 have significantly different physics parameterizations suites. This provides a unique opportunity to understand the impact of the structural changes on the evolution of the vortex. As the control case simulations demonstrated, the choice of CAM 4 or CAM 5 has a dominant impact on the intensity of the resulting tropical cyclone. The CAM 4 simulations indicate that the model might tend to converge with increasing horizontal resolution. The CAM 5 simulations show no signs of convergence and produce storms at day 10 that have near-record intensities at 0.25°. Although the CAM 5 0.25° minimum surface pressure values (with an ensemble range between 860-890 hPa) are extreme in comparison to real tropical cyclones, we cannot conclusively judge whether the CAM 4 or CAM 5 simulations are more plausible. This will require further model intercomparisons and possibly perturbed-parameter ensemble simulations with retuned empirical parameters in the physical parameterizations. However, comparisons to tropical cyclone observations might suggest that CAM 5 has more realistic vertical relative humidity and wind profiles at low levels.

It is concluded that the structural uncertainty is much larger than the initial-data and parameter uncertainty in this study. Both the initial-data and parameter uncertainty are of similar magnitude. The profound differences in the evolution of the tropical cyclone between the variants of CAM are due to the differences in the physical parameterizations, most likely those of the boundary layer and shallow convection. Such parameterizations are important in the development of tropical cyclones

in atmospheric models. We expect that similar uncertainty ranges at similar resolutions are possible when using the full CESM modeling framework for realistic tropical cyclone studies.

High-resolution GCMs are likely to become the tool of choice for simulating tropical cyclones. However, it remains unclear whether the GCM model designs are adequate to reliably simulate such intense storms. This paper has provided an initial look at how model uncertainty can impact such simulations. Future work using similar techniques will investigate the influence of various dynamical cores on the development of tropical cyclones, as this provides another component of structural uncertainty. In addition, the effect of other physical parameterization suites and the role of the physics-dynamics coupling will be explored.

# CHAPTER V

# Tropical cyclones in the spectral element configuration of the Community Atmosphere Model

## 5.1 Introduction

The simulation of tropical cyclones using general circulation models (GCMs) is a rapidly growing field and it is expected that next–generation GCMs utilizing quasi–uniform meshes will aid in this expansion. Examples of modeling efforts that utilize icosahedral, or geodesic, meshes to simulate tropical cyclones are *Fudeyasu et al.* (2008) and *Yamada et al.* (2010) which employ the Nonhydrostatic ICosahedral Atmospheric Model (NICAM) (*Tomita and Satoh*, 2004). The Geophysical Fluid Dynamics Laboratory (GFDL) finite–volume cubed-sphere model (*Donner et al.*, 2011) has been used for tropical cyclone climatology studies (*Zhao et al.*, 2009). In addition, the GFDL cubed-sphere model has been utilized for experiments of the inter–annual variability of tropical cyclone activity (*Chen and Lin*, 2011). These quasi–uniform mesh GCM simulations are typically run at horizontal resolutions of 50 km or less, with the NICAM simulations often run at non–hydrostatic scales of less than 10 km. Additionally, climatological GCM studies of tropical cyclones have been performed with conventional latitude–longitude meshes (i.e. *Oouchi et al.* (2006) and *Wehner*

*et al.* (2010)).

While GCM studies have shown skill in the ability to simulate tropical cyclones both in climatological and shorter–term studies, there is still concern on the reliability of GCMs for tropical cyclone assessments. The impact of GCM design choices of numerical schemes, mesh, diffusion properties and physical parameterizations on simulated storms remains unclear. Idealized studies by *Reed and Jablonowski* (2011b,c) have investigated the impact of different physical parameterization suites, as well as variations in the convection scheme, on the simulation of tropical cyclones in the Community Atmosphere Model (CAM) with the finite–volume (FV) dynamical core. The development of CAM is lead by the National Center for Atmospheric Research (NCAR). The current version of CAM, version 5, now includes a next–generation spectral element (SE) dynamical core that utilizes a cubed–sphere mesh. SE provides enhanced parallel scalability, making it a viable choice for massively parallel modern computer architectures. The goal of this paper is to evaluate the potential of CAM 5 SE to simulate tropical cyclones using an idealized initialization technique presented in *Reed and Jablonowski* (2011a). Specifically, this study will investigate the impact of resolution and uncertainty on tropical cyclone simulations. In addition, the paper explores the sensitivity of the simulated storms to the physics time step. Such a series of tests is an important step in understanding how the physics component of the GCM influences the development and intensity of the simulated tropical cyclones at untested, high horizontal resolutions with CAM 5 SE.

The paper is structured as follows. Section 5.2 provides a description of both the model and simulation design used for this study. The results are presented in Section 5.3, including a discussion of the impact of horizontal resolution, initial–data uncertainty and the physics time step. Section 5.4 discusses the conclusions and future research.

## 5.2 Methods

### 5.2.1 Model

The model used for this study is CAM 5, documented in *Neale et al.* (2010b), in combination with the SE dynamical core. The SE core is implemented on a cubed–sphere grid and is a dynamical core option included in CAM 5. The model design is documented in *Taylor and Fournier* (2010) and *Dennis et al.* (2011). SE utilizes a continuous Galerkin method in the horizontal directions and polynomials of degree 3 are selected to provide a fourth-order accurate horizontal discretization. The SE package includes a horizontal diffusion scheme based on fourth-order hyper-diffusion with an additional second-order dissipation near the model top. The model is run with the full physics parameterization suite and with the aqua–planet setup as proposed by *Neale and Hoskins* (2000), but with globally constant sea surface temperatures of 29°C.

The CAM 5 physics package utilizes deep and shallow convective parameterizations, as well as a moist boundary layer turbulence scheme. These are in addition to the parameterizations of cloud microphysics, cloud macrophysics, orographic gravity wave drag, the radiative effects of aerosols and parameterizations of shortwave and longwave radiation. The CAM 5 version used here contains a so–called Bulk Aerosol Model that utilizes prescribed aerosols. All simulations apply an identical physics tuning parameter set from CAM 5 climate simulations with the default FV dynamical core at a resolution of 1.0°. Our variant of CAM 5 is a recent configuration (CAM 5.0.51 from April 2011) that closely resembles CAM 5.1 released in June 2011.

### 5.2.2 Simulation design

The tropical cyclone simulations are initialized by an analytic technique described in detail in *Reed and Jablonowski* (2011a). The initialization of the vortex is built

upon prescribed 3D moisture, pressure, temperature and velocity fields that are embedded into tropical environmental conditions. For all simulations we initialize the model with a single, initially weak, warm–core vortex. The control vortex has a radius of maximum wind (RMW) of about 250 km and a 20 m $s^{-1}$ maximum initial wind speed located at the surface. The vortex is in hydrostatic and gradient–wind balance in an axisymmetric form.

Table 5.1: Horizontal grid resolutions, time steps and diffusion coefficients for the SE dynamical core in CAM 5. The physics time step $\triangle t$, the number of subcycles $m$ and the subcycled time step ( $\triangle\tau = \triangle t/m$) are provided.

| Resolution $n_e$ | No. of grid columns ncol | Grid distance at equator (km) | Subcycled time step $\triangle\tau$ (s) | Number of subcycles $m$ (#) | Physics time step $\triangle t$ (s) | Diffusion coefficient $K_4$ ($m^4$ $s^{-1}$) |
|---|---|---|---|---|---|---|
| 30 | 48,602 | 111 | 360 | 5 | 1800 | $1.0 \times 10^{15}$ |
| 60 | 194,402 | 55 | 180 | 5 | 900 | $1.0 \times 10^{14}$ |
| 120 | 777,602 | 28 | 75 | 6 | 450 | $1.0 \times 10^{13}$ |

CAM 5 SE is run with the default 30 vertical levels and at horizontal resolutions $n_e = 30$, 60 and 120, where each cube-face has a grid of $n_e \times n_e$ elements. Including the degrees of freedom within each element, these resolutions correspond to average equatorial grid spacings of roughly 111 km, 55 km and 28 km, respectively. Various settings for each resolution are provided in Table 5.1, including the diffusion coefficient $K_4$ and time steps. At each resolution there is the control simulation (following exactly *Reed and Jablonowski* (2011a)) and eight additional ensemble simulations where the control vortex is overlaid with random small–amplitude perturbations of the initial zonal and meridional wind velocities. The random perturbations are implemented globally and lie within the range of 2% of the initial wind speed at any given location.

At the highest resolution ($n_e = 120$) additional simulations are performed with the control vortex to test the impact of the CAM 5 physics time step $\triangle t$ on the evolution of the tropical cyclone, mainly the extreme intensities simulated (shown in Section 5.3).

Recent work by *Williamson* (2011) indicates that the effectiveness of CAM 4 physical parameterizations (especially the convection schemes), when run at shorter physics time steps, are limited by the explicit time scales in which the schemes are formulated. In this study the physics time step is decreased with increasing resolution, a common practice for resolution studies. A series of tests are performed by multiplying the physics time step by a factor of two and four. These tests will be referred to as $\triangle t =$ 900 s, and $\triangle t = 1800$ s, respectively. Note, the $\triangle t = 1800$ s case provides a unique study as this is the $\triangle t$ of the FV 1.0° tuning set. These tests require the setting of the number of subcycles (i.e. the number of times the dynamical core is called each physics time step) to $m = 12$ and $m = 24$ for the $\triangle t = 900$ s and $\triangle t = 1800$ s cases, respectively. This ensures that the dynamics time step remains the same.

## 5.3 Results and discussion

### 5.3.1 Resolution dependence

Figure 5.1 displays the wind speed at day 10 for the CAM 5 SE simulations using SE at $n_e = 30$, 60 and 120. The right column of Fig. 5.1 displays the horizontal cross sections of the magnitude of the wind at 100 m. The left column of Fig. 5.1 shows the longitude–height cross sections of the magnitude of the wind through the center latitude of the vortex. Note, the center of the vortex is defined to be the grid point with the minimum surface pressure. At all resolutions, the initial vortex develops into a tropical cyclone–like vortex with a maximum wind speed near the surface at the RMW, a near–calm eye region and a warm core (not shown). In addition, at each resolution the height of the absolute maximum wind speed is approximately 1 km, which corresponds well with observations of 0.5 to 1.0 km for Hurricane Isabel in 2003 as shown in *Bell and Montgomery* (2008). Figure 5.1 shows that as the resolution increases, the storm becomes more intense and more compact by day 10,

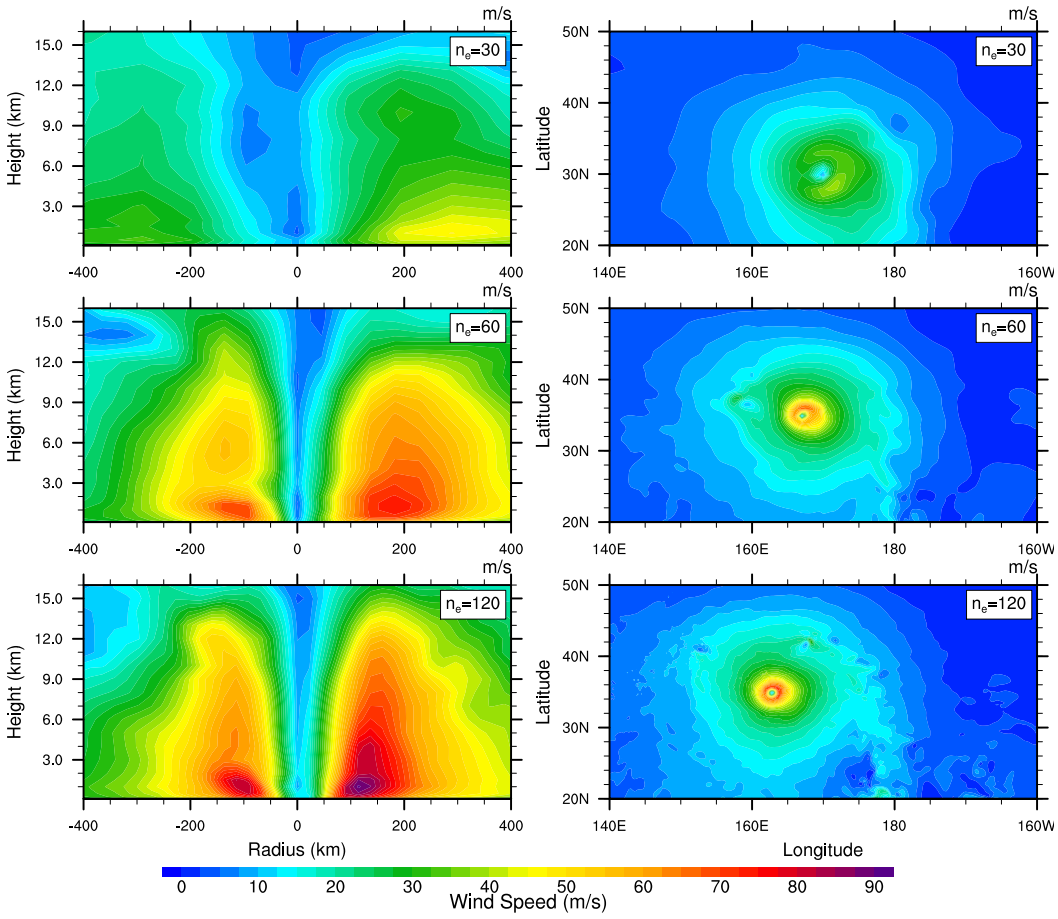


Figure 5.1: Snapshot of the tropical cyclone–like vortex at day 10 for CAM 5 SE at each horizontal resolution (as labeled). Left column: longitude–height cross section of the wind speed through the center latitude of the vortex as a function of the radius from the vortex center. Right column: horizontal cross section of the wind speed at a height of 100 m.

as evidenced by the smaller RMW. At the higher resolutions, the simulations show more small–scale features. At the highest resolution ($n_e = 120$), the cyclone becomes very strong with a maximum wind speed at 100 m of 73.18 m $s^{-1}$, corresponding to a category 5 hurricane on the Saffir–Simpson scale. Even at the highest resolution the RMW (roughly 100–150 km) is still large compared to observations, suggesting that even higher resolutions are required to simulate hurricanes adequately in GCMs.

Figure 5.2 displays the ensemble spread of CAM 5 SE for all resolutions. The evolution of the (a) minimum surface pressure and (b) the maximum 100 m wind speed

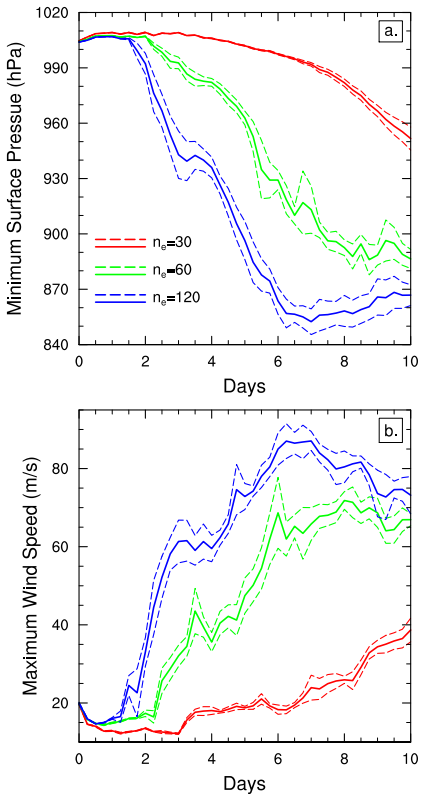


Figure 5.2: Time evolution of the (a.) minimum surface pressure and (b.) maximum wind speed at 100 m of the tropical cyclone at the horizontal resolutions of $n_e = 30$ (red), 60 (green) and 120 (blue) with CAM 5 SE. The solid line represents the control case and the dashed lines represents the variance as determined by the ensemble RMSD.

for the control vortex are shown as the solid line and the dashed lines represent the ensemble root–mean–square deviation (RMSD) from the control vortex case. Figure 5.2 provides valuable insight into the expected variance and thereby the uncertainty estimate of the control case simulation with respect to the initial–data uncertainty. As the initial vortex develops into a tropical cyclone uncertainties in the initial conditions produce a spread, as represented by the ensemble RSMD, in the evolutions of the storms on the order of about 1–5 m $s^{-1}$ in the low–level wind speeds and about 5–7 hPa in the minimum surface pressures at day 10. The maximum RMSD often occurs earlier in the evolution and is on the order of 3–9 m $s^{-1}$ and 6–17 hPa for the maximum wind speed and minimum surface pressure, respectively. As the resolution

increases the deviations in the wind speeds and surface pressure occur earlier in the simulations, likely linked to the earlier onset of intensification of the cyclone. In general, the absolute spread in the ensemble simulation becomes larger with increasing resolution.

Again, from Fig. 5.2 it is evident that as the resolution increases the maximum wind speed increases and the minimum surface pressure decreases. The lowest resolution simulations ($n_e = 30$) appear to never fully develop over the ten simulation days. In addition, there is little hint of convergence in intensity of the cyclone with resolution. The $n_e = 120$ ensemble simulations appear to reach extremely low minimum surface pressures at days 6–8 in the range of 845 to 865 hPa. Such minimum pressures are extreme and lower than those observed in nature. While these low pressures may partially be a result of the favorable, idealized conditions of the study, they are still concerning.

### 5.3.2 Sensitivity to physics time step

Physics parameterization suites are known to impact the evolution and intensity of tropical cyclones in GCMs (*Reed and Jablonowski*, 2011b,c). *Li et al.* (2011) has shown that the physics time step has a strong impact on the simulation of precipitation extremes in CAM 3. Furthermore, *Williamson* (2011) has called into question the fidelity of convective parameterizations in CAM 4 when run at shorter physics time steps. Therefore, the extremely low minimum surface pressures seen in Fig. 5.2 at the $n_e = 120$ resolution are investigated by altering the physics time step. Figure 5.3 displays the longitude–height cross sections of the magnitude of the wind through the center latitude of the vortex at day 10 at $n_e = 120$ for the tests in which the physics time step is increased to $\triangle t = 900$ s and $\triangle t = 1800$ s. From Fig. 5.3 it is apparent that as the physics time step is increased by a factor of two and four the simulated tropical cyclone becomes weaker at day 10 (compared to Fig. 5.1), as seen

in the wind speed. However, despite the change in intensity the structure, including a relatively calm eye and the location of the RMW, remains approximately the same. This suggests that resolution and model mesh are most influential on the size and structure of the storm, while the physics forcing plays a crucial role in determining the intensity of the cyclone.

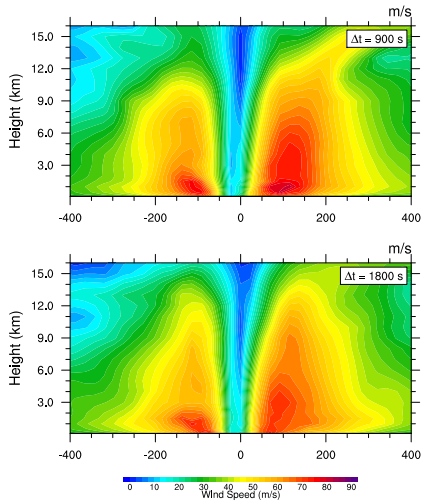


Figure 5.3: Snapshot of the longitude–height cross section of the wind speed through the center latitude of the tropical cyclone as a function of the radius from the vortex center at day 10. Results at $n_e = 120$ resolution for the $\triangle t =$ 900 s and $\triangle t = 1800$ s simulations with CAM 5 SE (as labeled).

Figure 5.4 provides insight into the impact of the physics on the evolution of the tropical cyclone minimum surface pressure and absolute maximum wind speed. From Fig. 5.4 it is apparent that the absolute minimum surface pressure for the $\triangle t =$ 900 s simulation does not vary significantly from the default $\triangle t = 450$ s simulation throughout the evolution of the storm, and appears to be within the initial–data uncertainty range. However, the $\triangle t = 1800$ s simulation does differ from the other two time step cases, especially earlier in the evolution of the storm where it is outside the uncertainty range. This suggests that the path to intensification is slightly different. These differences are more prominent in the evolution of the absolute maximum wind speed. Again, Fig. 5.4 shows that the $\triangle t = 450$ s and $\triangle t = 900$ s are rather similar, while the $\triangle t = 1800$ s simulation produces significantly reduced wind speeds. For the

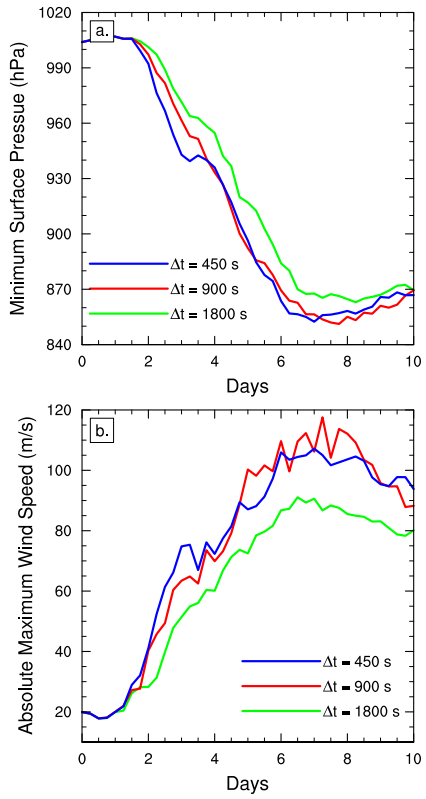


Figure 5.4: Time evolution of the (a.) minimum surface pressure and (b.) absolute maximum wind speed of the default ($\triangle t = 450$ s), $\triangle t = 900$ s and $\triangle t = 1800$ s simulations of CAM 5 SE at the horizontal resolution of $n_e = 120$.

$\triangle t = 450$ s and $\triangle t = 900$ s cases the absolute maximum wind speed reaches 105-115 m s$^{-1}$. In contrast, the $\triangle t = 1800$ s simulation peaks around 90 m s$^{-1}$. While such an intensity is still rather extreme, the intensity of such a tropical cyclone is more realistic. In addition, there is a slight delay in the onset of the intensification process with increased physics time step, but nothing near the differences seen with changes in resolution (Fig. 5.2).

Following *Williamson* (2011), we note that in CAM 5 the deep convection scheme is implemented as a relaxation, with a relaxation timescale of 1 hour. The tendency terms from the convection scheme continuously nudge the model towards a convectively stable state with the given timescale. Such a process should be relatively insensitive to the physics time step, and converge as the time step goes to zero. On the other hand, the CAM 5 large-scale condensation is implemented as a hard ad-

justment, which if represented as a tendency is equivalent to a relaxation with the timescale equal to the physics time step. Thus as $\triangle t$ is decreased, the large-scale condensation timescale becomes proportionally faster. In *Williamson* (2011), it was shown that when the large-scale condensation timescale is smaller than the convective timescales (in CAM 4 physics), intense grid point storms develop, fed by unphysically large latent heating due to interaction with the large-scale condensation. Similar results are seen here with CAM 5. Examining the convective and large-scale precipitation (not shown), we observe that as physics time step is increased, the convective precipitation increases, while the large–scale precipitation decreases. These processes likely contribute to the decreased intensity of the $\triangle t = 1800$ s storm.

## 5.4 Conclusion

An analytic tropical cyclone test case was implemented in order to understand the ability of the CAM 5 next–generation SE GCM to simulate tropical cyclones. CAM 5 SE was tested at the horizontal resolutions $n_e = 30$, 60 and 120 and in all cases a tropical cyclone developed during the 10–day idealized simulation. In general, the tropical cyclone becomes more compact, more intense and intensifies earlier with increasing resolution. In addition, as the resolution increases the ensemble spread, due to the initial–data uncertainty, increases and the onset of the spread occurs earlier in the simulation. At the highest resolution, $n_e = 120$, the tropical cyclone becomes extremely strong, with minimum surface pressure in the range of 845 to 865 hPa. These unrealistic pressures can be related to the dynamical SE component of the GCM, the interaction with the physics suite or the idealized nature of the simulations.

A sensitivity study at $n_e = 120$ in which the physics time step is increased by a factor of two and four provides more insight into the extreme intensities of the simulated tropical cyclone. As the physics time step is lengthened to $\triangle t = 1800$ s the

intensity of the storm is reduced, while the overall structure remains the same. This suggests that the interaction with the physics suite is contributing to the extreme intensities at the $n_e = 120$ resolution in a similar manner discussed in *Williamson* (2011). In addition, the choice of model grid and resolution significantly influences the onset of intensification, structure and size of the resulting tropical cyclone. One caveat is that the physics tuning parameters used for this study are based on the FV 1.0° version of CAM 5, as there are limited tuning sets available.

As advances in computer architectures lead to new design choices, such as high–resolution quasi–uniform meshes, in the development of GCM dynamical cores it is important that these models be tested for their reliability in the simulation of smaller–scale atmospheric phenomena. The next-generation CAM 5 SE model has been shown to be successful in the simulation of tropical cyclones at high–resolutions, yet it remains unclear how the physics parameterization suite will perform with these new techniques. Much research needs to be done to ensure that parameterizations of the future are not only modified for high–resolution GCMs, but are also built with consideration for simulating extreme events, such as tropical cyclones. Future work will investigate the ability of variable resolution meshes, including those with adaptive mesh refinement, in GCMs to simulate tropical cyclones. In addition, the sensitivity of the tropical cyclone simulations to the choice of physics–dynamics coupling will be explored.

# CHAPTER VI

# Idealized tropical cyclone simulations of intermediate complexity: A test case for AGCMs

## 6.1 Introduction

The testing of atmospheric general circulation models (AGCMs) is an important component of continued model evaluation and improvement. Tests help reveal the impact of an individual AGCM's design on the model representation of the atmospheric circulation and climate. In the absence of simple analytic solutions, AGCMs are often evaluated by model intercomparisons like the Atmospheric Model Intercomparison Project (AMIP) (*Gates*, 1992; *Gates et al.*, 1999). Such AMIP studies typically require AGCM simulations on the order of decades and are forced with prescribed, observation-based boundary data to investigate systematic errors of AGCMs. AMIP simulations are traditionally compared to global re-analysis data and observations, and to other AMIP runs from different AGCMs. However, identifying the reasons for model errors in these simulations still proves to be difficult due to the inherent complexity of AGCMs with full physical parameterization suites, complex boundary interactions, a land-sea mask and topography. Most often, the evaluation and interpretation of the results depend on the intuition and experience of the model development team.

Simpler model assessments can assist in identifying the causes and effects of the AGCM design choices more clearly. Here, we are particularly interested in the impact of the dynamical core on AGCM simulations while acknowledging that there are many other testbeds for physical parameterizations like the single column modeling approach (*Betts and Miller*, 1986; *Randall et al.*, 1996). The dynamical core is the central fluid flow component of an AGCM. It not only determines the choice of the fluid flow equations, but also the numerical technique, computational grid, grid staggering options, and dissipation mechanisms. The latter are intended to mimic unresolved subgrid-scale processes and might also be paramount to keep the numerical scheme of the dynamical core stable (*Jablonowski and Williamson*, 2011). The impact of the modeling choices on the circulation in the presence of moisture and physical parameterizations is highly nonlinear and not well understood. The impact is especially difficult to evaluate in isolation in complex full-physics simulations which motivates a simpler setup.

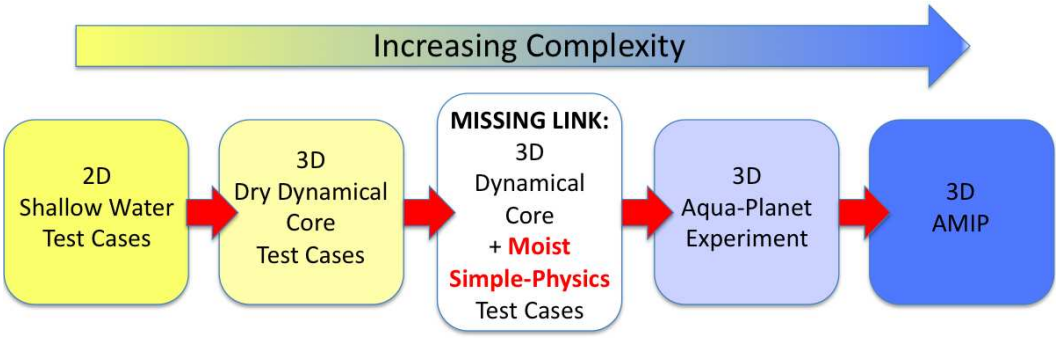


Figure 6.1: Diagram of the hierarchy of techniques for AGCM intercomparison and evaluation, emphasizing the need for intermediate complexity test cases.

Figure 6.1 displays the test hierarchy that is typically employed during the development phases of a dry dynamical core, and the coupled moist dynamics-physics AGCM at an advanced stage. The figure highlights the increases in complexity of the evaluation hierarchy from left to right. Typically, dynamical cores are first designed as 2D shallow water models on the sphere, which are the least complex models while

capturing main aspects of the atmospheric flow, like large-scale Rossby waves. The design of 2D shallow water models necessitates choices for the horizontal and temporal numerical discretizations that inherently incorporate the grid and its staggering option, as well as the horizontal diffusion and filtering operations if required. Such 2D models are typically evaluated with the shallow water test suite by *Williamson et al.* (1992) or the barotropic instability test suggested by *Galewsky et al.* (2004). Shallow water tests are most often run for 5-15 simulation days, and thereby classify as deterministic test cases.

The second more complex class of dry dynamical core test cases depicted in Fig. 6.1 includes the vertical dimension. Either hydrostatic or non-hydrostatic, and shallow-atmosphere or deep-atmosphere designs are feasible (see *White et al.* (2005) for an overview of the equation sets). 3D test cases like the baroclinic instability test case by *Jablonowski and Williamson* (2006a), *Lauritzen et al.* (2010) or *Polvani et al.* (2004), the 3D Rossby Haurwitz wave (*Monaco and Williams*, 1975; *Giraldo and Rosmond*, 2004) or the test suite by *Jablonowski et al.* (2008) are often used to assess the sensitivity of the dynamical core to the horizontal and vertical grid spacings, the impact of the computational grid, or the effects of the dissipation mechanisms. These aforementioned dynamical core tests are short deterministic test cases that can also assess the impact of idealized topography on the circulation. In addition, *Held and Suarez* (1994) and *Boer and Denis* (1997) suggested idealized evaluations of the model climate by introducing two simplified forcing mechanisms which serve as a "physical parameterization" package for the dynamical core. These forcing functions comprise a prescribed temperature relaxation and boundary layer friction that are applied during long-term (≈1200-day) simulations on a flat and dry Earth. Typically, time-mean zonal-mean flow fields are analyzed to evaluate the mean climatic state and its variability, and differences amongst models can be, at least partly, traced back to differences in the dynamical cores. However, the spatial and temporal averaging of

the model data smoothes out all small-scale features which makes it more difficult to isolate causes and effects in contrast to deterministic dynamical core evaluations.

The *Held and Suarez* (1994) climate assessments build bridges between the isolated dynamical core tests and full-physics experiments. But they neglect the highly nonlinear feedbacks between the dynamical core and physical parameterizations that are triggered by moisture processes. The latter are captured by aqua-planet experiments (APE, fourth box from the left in Fig. 6.1) as suggested by *Neale and Hoskins* (2000). APE studies are full-physics simulations that are forced with analytically prescribed sea surface temperatures (SSTs) on a flat and ocean-covered Earth. They thereby reduce the complexity of the boundary conditions while allowing the interaction of the dynamical core with the physical parameterizations. Typical APE studies are focused on the evaluation of the climatic state. They require long model integrations over several years as discussed by *Williamson* (2008b) or *Mishra et al.* (2011), and are generally compared to aqua-planet experiments of other AGCMs. In addition, short deterministic aqua-planet studies are feasible, as e.g. shown in the topical cyclone studies by *Reed and Jablonowski* (2011a,b,c).

The fifth and most complex category in Fig. 6.1 includes the AMIP studies mentioned earlier. They utilize spatially and temporally varying boundary conditions, as well as a realistic land-sea mask and topography. AMIP studies are typically conducted at a late stage of the dynamical core development cycle, before the atmospheric component is fully coupled to interactive ocean and ice models.

The jump in complexity between dry dynamical core test cases and APE and AMIP studies is quite substantial. The middle box of Fig. 6.1 accents the missing link between the dry and moist paradigms in the test hierarchy. We suggest that moist test cases of intermediate complexity can fill this void, and give an easier access to an improved understanding of the dynamics-physics interplay. This is especially true, if the new test case can mimic at least some of the behavior of complex full-

physics simulations. The purpose of this paper is to suggest such a test case of intermediate complexity, and to demonstrate its characteristics with the help of an idealized tropical cyclone (*Reed and Jablonowski*, 2011a). Our study is motivated by the observation that the representation of the idealized tropical cyclones in full-physics aqua-planet studies is highly sensitive to the choice of the AGCM dynamical core. This raises the question whether the key dynamics-physics interactions can already be captured by simplified physical forcing mechanisms and whether the outcomes resemble, to some degree, the full-physics studies. The characteristics of the test case are shown for four hydrostatic dynamical cores that are part of the Community Atmosphere Model CAM version 5 (CAM 5, *Neale et al.* (2010b)) developed at the National Center for Atmospheric Research (NCAR). These are the current CAM 5 default finite-volume (FV) model, the spectral element (SE) model that is sometimes also called the Higher Order Method Modeling Environment (HOMME), as well as the Eulerian (EUL) and semi-Lagrangian (SLD) spectral transform dynamical cores.

Specifically, we propose pairing the AGCM dynamical cores with simple moist physical parameterizations to test the evolution of a single, idealized, initially weak vortex into a tropical cyclone over ten simulation days. This test requires the definition of the initial conditions, as explained in detail in *Reed and Jablonowski* (2011a), and the definition of the reduced moist parameterization suite (called "simple-physics" hereafter), described in this paper. The initial conditions are analytic, allowing for an easy implementation on any computational grid. The simple-physics suite contains all necessary drivers for tropical cyclones, including large-scale condensation, surface fluxes and boundary layer turbulence. We note that the implementation of reduced physics packages within AGCMs has been introduced before (e.g. by *Molteni* (2002) and *Frierson et al.* (2006)), and the resulting models are sometimes characterized as Earth System Models of Intermediate Complexity (EMICs). The latter also include simplified ocean, ice and land models that are most often run at low resolutions over

many decades (*Claussen et al.*, 2002). However, there are two main differences to such earlier studies. First, we provide the complete description of the simple-physics package, its implementation and the physics-dynamics coupling strategy, which is paramount for model intercomparisons. Second, the simple-physics package described here is even more simplified than other comparable approaches, e.g. we leave out a radiative transfer scheme which can be justified for short deterministic model runs. The tropical cyclone serves as an example scenario. However, the simple-physics test paradigm is universal and and can also be applied to other flow fields.

The paper is organized as follows. The simple-physics suite is introduced in detail in section 6.2. Section 6.3 briefly reviews the design of NCAR's four CAM 5 dynamical cores and their horizontal grid spacings. The APE simulation results for each dynamical core with the full CAM 5 physics suite are presented in section 6.4. These full-physics simulations serve as a motivation for the more simplified physics assessments. The simple-physics experiments with each of the CAM 5 dynamical cores are then presented in section 6.5, along with an assessment of the model uncertainty. Section 6.6 summarizes our conclusions and outlines potential future research. A description of the hybrid vertical coordinate of the model CAM 5 and the details about the implementation of the simple-physics suite are provided in the appendices.

## 6.2 Introduction of the simple-physics parameterization suite

This section introduces the components of the simplified physical parameterization package called simple-physics. It contains selected physical processes that are important driving mechanisms for tropical cyclones such as

1. Large-scale condensation defined to occur when the atmosphere becomes saturated.

2. Surface fluxes of horizontal momentum, evaporation (specific humidity) and

sensible heat (temperature) from the ocean surface to the lower atmosphere.

3. Boundary layer turbulence of horizontal momentum, temperature and specific humidity.

Each component is explained in detail below to foster model intercomparisons. The simple-physics package assumes an ocean-covered (aqua-planet) Earth with a uniform SST of 29 °C. This temperature matches the SST of the initial conditions that trigger a spin-up of a tropical cyclone as described in *Reed and Jablonowski* (2011a). However, the simple-physics package is not limited to the tropical cyclone study used here for demonstration purposes. It can also be employed to explore other flow phenomena such as rainfall patterns in the presence of idealized mountains in the midlatitudes. The latter can be built upon test case 5-0-0 described in *Jablonowski et al.* (2008) with an adjusted SST which matches the initial surface temperature of this test case.

### 6.2.1 Large-scale condensation

The first component of the simple-physics package is the parameterization of large-scale condensation, and follows the approach used by many AGCMs, like the Integrated Forecasting System (IFS) of the European Centre for Medium-Range Weather Forecasts (*Tiedtke*, 1987). The large-scale condensation scheme does not include a cloud stage. No condensate is carried and the excess moisture is removed instantaneously without re-evaporation at lower levels. The model equations for the time rate of change of temperature $T$ and specific humidity $q$ due to condensation are

$$\frac{\partial T}{\partial t} = \frac{L}{c_p} C \tag{6.1}$$

$$\frac{\partial q}{\partial t} = -C, \tag{6.2}$$

where $L$ is the latent heat of vaporization at 0 °C ($= 2.5 \times 10^6$ J kg$^{-1}$) and $c_p$ is the specific heat of dry air ($= 1004.64$ J kg$^{-1}$ K$^{-1}$). The condensation rate $C$ is the rate

at which the saturation specific humidity $q_{sat}$ changes with time $t$

$$C = \frac{\mathrm{d}q_{sat}}{\mathrm{d}t}. \tag{6.3}$$

If the air is found to be supersaturated (that is $q > q_{sat}(T, p)$, where $p$ is pressure) $T$ and $q$ need to be adjusted to their saturation values, which will lead to the updated values $T^{n+1}$ and $q^{n+1}$ at the future time level $n + 1$

$$T^{n+1} = T + \triangle T \tag{6.4}$$

$$q^{n+1} = q + \triangle q. \tag{6.5}$$

The time index of the $T$ and $q$ values on the right hand side (RHS) of these equations depends upon the AGCM design which might enforce constraints on the suitable physics-dynamics coupling strategy. Two coupling strategies are common which are called process-split and time-split (*Williamson*, 2002). In models with process-split physics-dynamics coupling $T$ and $q$ represent either the values at the current time level ($n$) for two-time-level schemes or the values at the previous time level ($n - 1$) for three-time-level schemes, like e.g. the leapfrog method used in CAM 5 EUL (*Neale et al.*, 2010b). In time-split models, the values of $T$ and $q$ are already partially updated by the time tendencies of the dynamical core before physical forcings are invoked. We leave the specific choice of the physics-dynamics coupling to the modeling group. However, in case no prior constraints exist we recommend the time-split approach. Note, pressure $p$ is assumed to be time-invariant during individual physics parameterizations. This is a common assumption in AGCMs since the moist pressure is typically adjusted exactly once at the very end of the physics suite as further outlined in section 6.2.4.

The correction factors $\triangle T$ and $\triangle q$ are given by

$$\triangle T = -\frac{L}{c_p}\triangle q \tag{6.6}$$

$$\triangle q = q_{sat}(T^{n+1}, p) - q. \tag{6.7}$$

Here $q_{sat}(T^{n+1}, p)$ is approximated by a first-order Taylor series

$$q_{sat}(T^{n+1}, p) \cong q_{sat}(T, p) + \frac{\mathrm{d}q_{sat}(T, p)}{\mathrm{d}T}\triangle T. \tag{6.8}$$

The derivative of $q_{sat}(T, p)$ with respect to $T$ appears as a total derivative since $p$ remains unchanged during the physics time step. The forms of $T^{n+1}$ and $q^{n+1}$ are then represented by

$$T^{n+1} = T + \frac{L}{c_p}\left(\frac{q - q_{sat}(T, p)}{1 + \frac{L}{c_p}\frac{\mathrm{d}q_{sat}(T,p)}{\mathrm{d}T}}\right) \tag{6.9}$$

$$q^{n+1} = q - \frac{q - q_{sat}(T, p)}{1 + \frac{L}{c_p}\frac{\mathrm{d}q_{sat}(T,p)}{\mathrm{d}T}}. \tag{6.10}$$

This leads to the expression of the condensation rate for models with two-time-level schemes

$$C = \frac{1}{\triangle t}\left(\frac{q - q_{sat}(T, p)}{1 + \frac{L}{c_p}\frac{\mathrm{d}q_{sat}(T,p)}{\mathrm{d}T}}\right) \tag{6.11}$$

where $\triangle t$ symbolizes the discrete physics time step. Note that the physics time step may be different from the dynamics or tracer advection time steps as it is the case in the model CAM 5 FV (*Neale et al.*, 2010b). In models with a three-time-level leapfrog scheme, $\triangle t$ needs to be replaced with $2\triangle t$.

We now need to define the derivative of the saturated specific humidity with respect to temperature under the assumption of constant pressure. From *Holton*

(2004) we approximate this to be

$$\frac{\mathrm{d}q_{sat}(T,p)}{\mathrm{d}T} \approx \frac{\varepsilon}{p}\frac{\mathrm{d}e_s(T)}{\mathrm{d}T} = \frac{Lq_{sat}(T,p)}{R_\nu T^2} \tag{6.12}$$

where $e_s$ is the saturation vapor pressure, $R_\nu$ is the gas constant for water vapor ($= 461.5$ J kg$^{-1}$ K$^{-1}$) and $\varepsilon$ is the ratio of the gas constant for dry air $R_d$ ($= 287.04$ J kg$^{-1}$ K$^{-1}$) to that for water vapor ($\varepsilon = 0.622$). We approximate the saturation specific humidity by utilizing the Clausius-Clapeyron equation for the saturation vapor pressure in the form

$$q_{sat}(T,p) \approx \varepsilon\frac{e_s(T)}{p} \approx \frac{\varepsilon}{p}e_0^* e^{-(L/R_\nu)[(1/T)-(1/T_0)]} \tag{6.13}$$

where $e_0^*$ ($= 610.78$ Pa) is the saturation vapor pressure at $T_0 = 273.16$ K. This formulation was also used in *Frierson et al.* (2006) for idealized model simulations. As mentioned before, it is assumed that all of the condensed water vapor immediately falls out as precipitation without re-evaporation. The large-scale precipitation rate $P_{ls}$ is therefore given as

$$P_{ls} = \frac{1}{\rho_{water}}\int_0^\infty C\rho\mathrm{d}z = \frac{1}{\rho_{water}g}\int_0^{p_s} C\mathrm{d}p \tag{6.14}$$

where the hydrostatic relation is used to eliminate the air density $\rho$, $\rho_{water} = 1000$ kg m$^{-3}$ is the density of water, $g = 9.80616$ m s$^{-2}$ is the gravity and $p_s$ is the surface pressure. The units of $P_{ls}$ are meters of water per second (m$_{H_2O}$ s$^{-1}$). The quantity $P_{ls}$ can be used as a diagnostic quantity.

### 6.2.2 Surface fluxes

The second component of the simple-physics package is the parameterization of the interaction of the atmosphere with the ocean surface. These fluxes also deter-

mine the eddy diffusivities for the boundary layer parameterization as explained in section 6.2.3. To parameterize the surface fluxes that impact the zonal velocity $u$, the meridional velocity $v$, temperature and moisture we start with the time rate of change equations

$$\frac{\partial u}{\partial t} = -\frac{1}{\rho}\frac{\partial \rho\, \overline{w'u'}}{\partial z} \tag{6.15}$$

$$\frac{\partial v}{\partial t} = -\frac{1}{\rho}\frac{\partial \rho\, \overline{w'v'}}{\partial z} \tag{6.16}$$

$$\frac{\partial T}{\partial t} = -\frac{1}{\rho}\frac{\partial \rho\, \overline{w'T'}}{\partial z} \tag{6.17}$$

$$\frac{\partial q}{\partial t} = -\frac{1}{\rho}\frac{\partial \rho\, \overline{w'q'}}{\partial z}. \tag{6.18}$$

Here $u'$, $v'$, $w'$, $T'$ and $q'$ symbolize the deviations of the zonal velocity, meridional velocity, vertical velocity, temperature and specific humidity from their time averages, repectively. A time average is indicated by an overbar. For non-hydrostatic models the time rate of change equations for the vertical velocity $\frac{\partial w}{\partial t}$ should be set to zero.

The eddy turbulence surface momentum fluxes on the RHS of Eqs. (6.15) and (6.16) are approximated by the bulk aerodynamic formulae in kinematic units

$$(\overline{w'u'})_s = -C_d|\vec{v}_a|u_a \tag{6.19}$$

$$(\overline{w'v'})_s = -C_d|\vec{v}_a|v_a, \tag{6.20}$$

where the subscript $s$ denotes a surface flux. $|\vec{v}_a|$ is the wind speed of the horizontal wind ($|\vec{v}_a| = \sqrt{u_a^2 + v_a^2}$) at the lowermost model level, and $u_a$ and $v_a$ are the zonal and meridional wind components, respectively. This formulation of the surface fluxes implies that the wind velocities at the height of the ocean surface $z_0 = 0$ m are zero ($u_s = v_s = 0$ m s$^{-1}$), thereby forcing the stress to vanish at $z_0$. Here the drag

coefficient, $C_d$, depends on the magnitude of the wind at the lowermost model level

$$\begin{aligned} C_d &= C_{d0} + C_{d1}|\vec{v}_a| \quad \text{for } |\vec{v}_a| < 20 \text{ m s}^{-1} \\ C_d &= 0.002 \qquad\qquad\quad \text{for } |\vec{v}_a| \geq 20 \text{ m s}^{-1}, \end{aligned} \tag{6.21}$$

where $C_{d0}$ and $C_{d1}$ are defined in *Smith and Vogl* (2008) to be $7.0 \times 10^{-4}$ and $6.5 \times 10^{-5}$ s m$^{-1}$, respectively, as derived from *Black et al.* (2007).

Evaporation occurs at the surface and is similarly described by the kinematic eddy flux of water vapor. It is expressed via the bulk formula for latent heat

$$(\overline{w'q'})_s = C_E|\vec{v}_a|(q_{sat,s} - q_a), \tag{6.22}$$

where $q_a$ is the specific humidty of the lowermost model level and $C_E$ is the bulk transfer coefficient for water vapor. $q_{sat,s}$ is the saturation specific humidity (Eq. (6.13)) computed with the SST value, which is 302.15 K for the tropical cyclone test case, and the surface pressure (*Hasse and Smith*, 1997). The kinematic eddy sensible heat flux at the surface is defined by the bulk formula

$$(\overline{w'T'})_s = C_H|\vec{v}_a|(T_s - T_a), \tag{6.23}$$

where $C_H$ is the bulk heat transfer coefficient, $T_a$ is the temperature of the lowermost model level and $T_s$ is the surface temperature, with $T_s$ taken to be the SST. For both evaporation and sensible heat the bulk coefficient is set to a constant, $C_E = C_H = 0.0011$, as suggested by *Garratt* (1992), *Hasse and Smith* (1997), and *Smith and Vogl* (2008) for ocean surfaces. All fluxes are specified in kinematic units which are m$^2$ s$^{-2}$ for the momentum fluxes, K m s$^{-1}$ for the sensible heat flux and (kg$_{vapor}$ kg$_{air}^{-1}$) (m s$^{-1}$) for the evaporation flux. If required, energy-based physical units (W m$^{-2}$) can be recovered if the horizontal momentum fluxes (Eqs. (6.19) and (6.20)) are multiplied by the density at the lowermost model level $\rho_a$, the latent heat flux

(Eq. (6.22)) is multiplied by $\rho_a c_p$, and the sensible heat flux (Eq. (6.23)) is multiplied by $\rho_a L$. However, the implementation presented here utilizes kinematic fluxes. A positive flux denotes an upward transfer from the ocean surface into the atmosphere.

The surface fluxes (Eqs. (6.15) - (6.18)) are used to calculate the respective time tendencies of the state variables $u$, $v$, $q$ and $T$ at the lowermost model level. The spatially discretized form yields

$$\frac{\partial u_a}{\partial t} = -\frac{1}{\rho_a}\frac{\rho_a\,(\overline{w'u'})_a - \rho_s\,(\overline{w'u'})_s}{z_a - z_0} \tag{6.24}$$

$$\frac{\partial v_a}{\partial t} = -\frac{1}{\rho_a}\frac{\rho_a\,(\overline{w'v'})_a - \rho_s\,(\overline{w'v'})_s}{z_a - z_0} \tag{6.25}$$

$$\frac{\partial T_a}{\partial t} = -\frac{1}{\rho_a}\frac{\rho_a\,(\overline{w'T'})_a - \rho_s\,(\overline{w'T'})_s}{z_a - z_0} \tag{6.26}$$

$$\frac{\partial q_a}{\partial t} = -\frac{1}{\rho_a}\frac{\rho_a\,(\overline{w'q'})_a - \rho_s\,(\overline{w'q'})_s}{z_a - z_0}. \tag{6.27}$$

Again, the subscripts $s$ and $a$ represent the quantities at the surface and lowermost model level, repectively. $z_a$ is defined as the height (in m) of the lowermost full model level and can be expressed with the help of the hydrostatic equation in terms of pressure

$$z_a = \frac{R_d T_{\nu,a}}{g}\frac{(\ln p_- - \ln p_s)}{2}, \tag{6.28}$$

where $T_{\nu,a} = T_a(1 + 0.608 q_a)$ is the virtual temperature at the lowermost full model level and $p_-$ is the edge pressure at the model level interface between the lowest and second lowest full model levels. This notation and all previous and following equations assume that the temperature, horizontal wind components and the specific humidity in the physical parameterization package are co-located in both the vertical and horizontal directions, as it is the case for the Lorenz grid (*Lorenz*, 1960) and Arakawa-A grid (*Arakawa and Lamb*, 1977). Most often, AGCMs utilize such a co-located, possibly interpolated, grid in the physical parameterization suite, regardless

of the staggering option in the dynamical core. If other vertical or horizontal grid staggering options are utilized in the physics package, the exact forms of the surface flux and boundary layer equations need to be adjusted accordingly.

All eddy fluxes at the lowermost model level (e.g. $(\overline{w'u'})_a$) are now set to zero, as all turbulent contributions from above the lowermost model level are accounted for in the boundary layer scheme described later in section 6.2.3. This results in the following form of the surface fluxes and illustrates how they impact the time tendencies at the lowest model level

$$\frac{\partial u_a}{\partial t} = -\frac{1}{\rho_a}\frac{-\rho_s\ (\overline{w'u'})_s}{z_a} \tag{6.29}$$

$$\frac{\partial v_a}{\partial t} = -\frac{1}{\rho_a}\frac{-\rho_s\ (\overline{w'v'})_s}{z_a} \tag{6.30}$$

$$\frac{\partial T_a}{\partial t} = -\frac{1}{\rho_a}\frac{-\rho_s\ (\overline{w'T'})_s}{z_a} \tag{6.31}$$

$$\frac{\partial q_a}{\partial t} = -\frac{1}{\rho_a}\frac{-\rho_s\ (\overline{w'q'})_s}{z_a}. \tag{6.32}$$

$\rho_s$ is the density at the surface, which for simplicity is assumed to be equal to $\rho_a$ due to the typically chosen proximity of the lowermost model level to the surface. Therefore, we let the terms cancel. In our CAM 5 tropical cyclone tests presented later in sections 6.4 and 6.5 with a hybrid $\sigma$-pressure vertical coordinate (see Appendix A and *Simmons and Burridge* (1981)), the height position of the lowermost full model level is about $z_a = 70$ m. We define this height as the approximate height of the surface layer. Since the strength of the surface forcing is impacted by this choice, we encourage the users of this test case to pick about the same height position for their lowermost full model level. In any case, the approximate position of $z_a$ needs to be documented.

The final form of the surface fluxes is

$$\frac{\partial u_a}{\partial t} = -\frac{C_d|\vec{v}_a|u_a}{z_a} \tag{6.33}$$

$$\frac{\partial v_a}{\partial t} = -\frac{C_d|\vec{v}_a|v_a}{z_a} \tag{6.34}$$

$$\frac{\partial T_a}{\partial t} = \frac{C_H|\vec{v}_a|(T_s - T_a)}{z_a} \tag{6.35}$$

$$\frac{\partial q_a}{\partial t} = \frac{C_E|\vec{v}_a|(q_{sat,s} - q_a)}{z_a}. \tag{6.36}$$

We again note that the wind at the surface is taken to be zero and therefore does not appear explicitly in Eqs. (6.33) and (6.34). All time derivatives of the surface fluxes are discretized in a semi-implicit way to avoid numerical instabilities, which is detailed in Appendix B.

The final form of the surface fluxes will vary for models with other choices of prognostic variables. For example, if potential temperature $\Theta_a$ is used Eq. (6.35) takes the form

$$\frac{\partial \Theta_a}{\partial t} = \frac{C_H|\vec{v}_a|(T_s - T_a)}{z_a}\left(\frac{p_{00}}{p_a}\right)^{R_d/c_p} \tag{6.37}$$

where $p_{00} = 10^5$ Pa is a reference pressure. This conversion uses the assumption that the pressure is time-invariant when individual physics parameterizations are applied. This is a common assumption in AGCMs since the moist pressure is typically adjusted exactly once at the very end of the physics suite as further outlined in section 6.2.4. For other choices of prognostic variables like $(\rho u)_a$, $(\rho v)_a$, $(\rho\Theta)_a$ and $(\rho q)_a$ the right-hand-side of Eqs. (6.33), (6.34), (6.37) and (6.36) would need to be multiplied by $\rho_a$.

### 6.2.3 Boundary layer diffusion

The final component of the simple-physics package is the parametrization of a simple diffusive boundary layer. Potential temperature, as opposed to temperature, is used in the boundary layer parameterization because the vertical profile of the potential temperature is a suitable indicator of static stability. The base equation set for the boundary layer diffusion is described by Eqs. (6.15)-(6.18). However, the time rate of change equation of potential temperature $\Theta$ replaces the temperature tendency in Eq. (6.17). It yields

$$\frac{\partial \Theta}{\partial t} = -\frac{1}{\rho}\frac{\partial \rho \, \overline{w'\Theta'}}{\partial z}. \tag{6.38}$$

The potential temperature tendency can be converted back to a temperature $T$ tendency of the following form

$$\frac{\partial T}{\partial t} = -\frac{1}{\rho}\left(\frac{p}{p_{00}}\right)^{R_d/c_p}\frac{\partial \rho \, \overline{w'\Theta'}}{\partial z}. \tag{6.39}$$

Again, this conversion assumes that the pressure is time-invariant during the application of the diffusion. The partial derivatives with respect to height in this and all following equations can also be converted to pressure-based derivatives using the hydrostatic approximation. This is explained in detail in Appendix C.

Boundary layers in rotating flows have special characteristics, as seen with Ekman theory. First-order approximations to the representation of boundary layers within hurricanes have been found to resemble Ekman-like profiles, where turbulent mixing is characterized by a constant vertical eddy diffusivity $K_m$ (see *Bode and Smith* (1975)).

Such turbulent mixing is characterized as

$$\overline{w'u'} = -K_m \frac{\partial u}{\partial z} \tag{6.40}$$

$$\overline{w'v'} = -K_m \frac{\partial v}{\partial z} \tag{6.41}$$

$$\overline{w'\Theta'} = -K_E \frac{\partial \Theta}{\partial z} \tag{6.42}$$

$$\overline{w'q'} = -K_E \frac{\partial q}{\partial z}, \tag{6.43}$$

where $K_m$ is the eddy diffusivity coefficient for momentum and $K_E$ is the eddy diffusivity coefficient for energy, which is most often set equal to that for water vapor.

Similar to *Bode and Smith* (1975) we match the eddy diffusivity to the wind stress sublayer which we calculated earlier to be the surface momentum flux at the lowermost model level. Therefore to first-order, we approximate $K_m$ from the following formulation of the vertical turbulent flux of zonal momentum $\overline{w'u'}$ and demand that it matches $(\overline{w'u'})_s$ at the lowermost layer

$$(\overline{w'u'})_s = -K_m \frac{\partial u}{\partial z}. \tag{6.44}$$

At the lowermost model level this corresponds to the expression

$$-C_d|\vec{v}_a|u_a = -K_m \frac{u_a}{\triangle z} \tag{6.45}$$

in the discretized form, where $\triangle z$ is the height difference between $z_a$ and $z_0$, and therefore $\triangle z = z_a$ (e.g. see Eq. (6.28)). As before, we recommend selecting the lowermost full model level at a height of about 70 m to allow for intercomparisons to the results presented later. One last time we utilize the lower boundary condition that the wind velocities at the height of the ocean surface $z_0$ are zero. For simplicity the boundary layer is defined to be all levels with pressure values greater than $p_{top} = 850$ hPa (corresponding to a boundary layer height of approximately 1-1.5 km). Solving

Eq. (6.45) for $K_m$ and tapering the eddy diffusivity to zero above $p_{top}$ gives

$$\begin{aligned} K_m &= C_d|\vec{v}_a|z_a && \text{for } p > p_{top} \\ K_m &= C_d|\vec{v}_a|z_a \exp\left(-\left[\tfrac{p_{top}-p}{p_{strato}}\right]^2\right) && \text{for } p \leq p_{top}. \end{aligned} \tag{6.46}$$

where we let $K_m$ go to zero to ensure a smooth transition above the boundary layer. Here the constant $p_{strato}$ determines the rate of decrease and is set to 100 hPa. This choice of $p_{strato}$ lets $K_m$ decrease by a factor of ten at the 700 hPa level. Similarly, $K_E$ is defined by

$$\begin{aligned} K_E &= C_E|\vec{v}_a|z_a && \text{for } p > p_{top} \\ K_E &= C_E|\vec{v}_a|z_a \exp\left(-\left[\tfrac{p_{top}-p}{p_{strato}}\right]^2\right) && \text{for } p \leq p_{top}. \end{aligned} \tag{6.47}$$

These eddy diffusivities, and therefore the turbulent mixing, varies in space and time depending upon the magnitude of the horizontal wind $|\vec{v}_a|$ and the height $z_a$ of the lowermost model level. This method reflects a simplified first-order coupling of the boundary layer diffusion to the dynamic conditions while omitting more complicated mechanisms such as the dependence of the eddy diffusivities on static stability indicators like Richardon numbers. This simplification of the boundary layer diffusivities is a deliberate choice. The boundary layer scheme is implemented with a partially implicit temporal discretization to avoid numerical instabillties. The details are explained in Appendix C.

### 6.2.4 Coupling of the simple-physics processes

The simple-physics suite is invoked with the state variables $u, v, q, T$ from the dynamical core. These might already be partially updated (time-split) or might not be updated (process-split) with the time tendencies from the dynamical core. This physics-dynamics coupling choice depends upon possible constraints imposed by the

dynamical core as outlined in section 6.2.1 or *Williamson* (2002). However, within the simple-physics parameterization suite all processes are coupled via time-splitting. With time-split coupling the individual physical parameterizations are applied sequentially and each component is based on the updated state provided by the previous process. The components are time-split in the following order:

1. The large-scale condensation scheme loops over all vertical levels at each horizontal grid point. It readily updates $T$ and $q$ throughout the vertical column using Eqs. (6.9)-(6.10).

2. Next, the updated $T, q$ state variables and $u, v$ wind components are used in the implementation of the surface fluxes. These variables are updated at the lowermost full model level according to Eqs. (B.3)-(B.6).

3. All state variables throughout the column are then updated with the boundary layer scheme and supplied back to the dynamical core for the calculations of the next time step. The boundary layer updates are described by Eqs. (C.15), (C.21), (C.28) and (C.31).

At the end of the simple-physics suite care needs to be taken to ensure that the model conserves the total dry air mass or its analog, the global average of the dry surface pressure. This is especially true if the moist surface pressure is predicted in the dynamical core, as it is the case in CAM 5. The adjustment can take place in either the dynamical core or at the end of the physics package which again depends on the AGCM design. Most often, AGCMs already provide a mechanism to ensure that the total dry air mass is conserved, such as global mass fixers or explicit dry air adjustment routines as discussed in e.g. *Neale et al.* (2010b). If not, such a mechanism needs to be supplied. If the total amount of dry air needs to be prescribed, the initial conditions as provided in *Reed and Jablonowski* (2011a) contain a globally averaged dry surface pressure of about 1010 hPa.

### 6.2.5 Additional design choices

As mentioned before, we recommend placing the lowermost full model level at a height of about 70 m to allow for straightforward comparisons to the example calculation presented later. Additional parameterizations, including convection or a radiative transfer routine, are not included in the simple-physics package to ensure its reduced complexity. Radiation is excluded since it is not one of the main drivers for tropical cyclogenesis in our short ten-day simulations. In addition, both shallow and deep convection are not included as large-scale condensation appears to be a sufficient driver for the idealized tropical cyclone at high horizontal resolutions. While it is may be presumed that convection is necessary for the simulation of tropical cyclones, this is not the case. *Rosenthal* (1978) demonstrated that a hydrostatic model, with 20 km horizontal resolution, could simulate tropical cyclone development successfully with only large-scale condensation. Furthermore, the boundary layer scheme does not utilize sophisticated turbulence closure techniques with atmospheric stability constraints. This again ensures the simplicity of the boundary layer diffusion.

The simple-physics package is only recommended for short deterministic studies. For long-term simulations beyond e.g. 30 days, extensions such as a Newtonian temperature relaxation mechanism should be included to mimic the radiative transfer. The simple-physics package can readily be coupled to different dynamical cores to test the impact of the fluid flow package on the simulation. Another benefit of simple-physics is that each individual parameterization can be easily turned off and on, allowing for the examination of the role of each physical process. The simple-physics package thereby provides a tool for process and sensitivity studies, especially with respect to varying physics parameterizations or coefficients.

## 6.3 Description of the CAM 5 dynamical cores

The idealized tropical cyclone test case with the simple-physics suite is coupled to the four hydrostatic dynamical cores that are options in NCAR's CAM 5 model. The dynamical cores include the FV dynamical core, the SE model, and the spectral transform EUL and SLD dynamics packages (*Neale et al.*, 2010b). These four dynamical cores are used to demonstrate the characteristics of the test case and reveal the impact of the dynamical core on the simulations. Below, we provide a brief overview of each dynamical core, and the utilized grid spacings between 156 km and 28 km, their corresponding dynamics and physics time steps, and the resolution-dependent diffusion coefficients. All CAM 5 simulations use the standard 30 vertical levels (L30) with the terrain-following hybrid $\sigma$-pressure coordinate $\eta$. The model top is placed at $\approx$ 2 hPa. Details about the $\eta$ coordinate and its hybrid coefficients for L30 are listed in Appendix A.

### 6.3.1 Finite–Volume (FV)

The FV dynamical core is the default dynamical core in CAM versions 4 (*Neale et al.*, 2010a), 5 and 5.1 (*Neale et al.*, 2010b). The dynamical core is defined on a regular latitude–longitude grid that includes both pole points. The prognostic variables are staggered as in the Arakawa-D grid. The mass-conservative FV dynamical core in flux-form is built upon a 2D shallow water approach in the horizontal plane (*Lin and Rood*, 1996, 1997). The vertical discretization follows a "Lagrangian control-volume" principle, which is based on a terrain-following "floating" Lagrangian coordinate system and a fixed "Eulerian" reference frame. In particular, the vertically-stacked volumes are allowed to float for a duration of several dynamics time steps before they are mapped back monotonically and conservatively to a fixed hybrid reference system (*Lin*, 2004). The advection algorithm makes use of the monotonic third-order Piecewise Parabolic Method (PPM, *Colella and Woodward* (1984)) with an explicit

time-stepping scheme. The algorithm also includes limiters that inherently damp grid-scale noise in the potential temperature and vorticity field. The divergent modes are controlled through explicit fourth-order horizontal divergence damping which is explained in *Whitehead et al.* (2011). The model is further stabilized via a Fast Fourier Transform (FFT) filter that is used in the zonal direction poleward of about 40° N/S. The dynamics and physics packages are coupled via a time-split approach.

In our study the FV dynamical core is run at the horizontal resolutions $\triangle\varphi \times \triangle\lambda$ as listed in Table 6.1, where $\triangle\varphi$ and $\triangle\lambda$ represent the latitudinal and longitudinal grid spacings in degrees, respectively. Table 6.1 also provides the approximate physical grid distances $\triangle x, \triangle y$ in the equatorial region. The time steps are represented as the subcycled dynamics time steps $\triangle\tau$ and the physics time steps $\triangle t$. The physics time step is the time interval with which the physical parameterizations are called. The FV vertical remapping algorithm is invoked every $m = 10$ subcycled dynamics time steps.

Table 6.1: Horizontal grid resolutions and time steps for the FV dynamical core in CAM 5. The number of latitudes (lat) includes both pole points. The subcycled dynamics time step $\triangle\tau = \triangle t/m$ with $m = 10$ is listed, in addition to the physics time step $\triangle t$.

| Resolution $\triangle\varphi \times \triangle\lambda$ | No. of grid points lat × lon | Grid distance at equator $\triangle x, \triangle y$ (km) | Subcycled dynamics time step $\triangle\tau$ (s) | Physics time step $\triangle t$ (s) |
|---|---|---|---|---|
| 1.0° × 1.0° | 181 × 360 | 111 | 180 | 1800 |
| 0.5° × 0.5° | 361 × 720 | 55 | 90 | 900 |
| 0.25° × 0.25° | 721 × 1440 | 28 | 45 | 450 |

### 6.3.2 Spectral Element (SE)

The SE dynamical core is anticipated to become the default dynamical core in the future CAM release CAM 5.2. The model development and detailed design are documented in *Taylor et al.* (2007, 2008), *Taylor and Fournier* (2010), *Taylor* (2011)

and *Dennis et al.* (2011). SE utilizes an explicit Runge-Kutta time stepping approach and a continuous Galerkin spectral finite element method in the horizontal directions. The latter is described in *Taylor et al.* (1997) and *Fournier et al.* (2004). The horizontal discretization is built upon unstructured quadrilaterals (a cubed-sphere mesh). In our study we select third-order polynomials that provide a fourth-order accurate horizontal discretization. These polynomials make use of $4 \times 4$ Gauss-Lobatto-Legendre (GLL) quadrature points within each spectral element.

The SE dynamical core shares some properties with the Eulerian spectral model described below. They utilize the same hybrid vertical coordinate and vertical finite-difference discretization, the horizontal diffusion scheme is based on fourth-order hyper-diffusion, and a second-order dissipation provides a sponge at the model top. The main differences are that SE uses the vector-invariant form of the momentum equations instead of the vorticity-divergence formulation as in EUL, and advects the surface pressure instead of its logarithm in order to conserve mass and energy in the dynamics package.

The physics-dynamics and tracer coupling strategy follows a hybrid paradigm. This means that the physics and dynamics packages are coupled via a process-split approach, whereas the tracer advection (e.g. for the moisture variable $q$) is coupled to the dynamics via time-splitting. The tracer transport scheme is built upon the same spectral element method in the horizontal, and utilizes a remapping algorithm in the vertical direction. A positive-definite constraint is applied to ensure a positive tracer mass. An offline remapping scheme called Geometrically Exact Conservative Remapping (GECoRe), explained in *Ullrich et al.* (2009), is used to map the model variables from the SE cubed-sphere grid to a regular latitude-longitude grid for all analyses in this study.

The horizontal resolutions, time steps and fourth-order $K_4$ diffusion coefficients for the SE dynamical are shown in Table 6.2. The resolution is defined as the number

of spectral elements $n_e$ along the edge of each cube face. These elements are further subdivided by the GLL quadrature points. A depiction of the grid and the location of the four GLL points in each element are e.g. shown in *Dennis et al.* (2011). The time steps in Table 6.2 are represented as the subcycled dynamics time steps and the physics time steps. The number of subcycles for the SE dynamical core depends on the resolution because of stability constraints. The $\nabla^2$ horizontal diffusion coefficient $K_2$ in the sponge layer in the topmost three vertical levels is 2.5 $\times 10^5$ m$^2$ s$^{-1}$ at all resolutions.

Table 6.2: Horizontal grid resolutions, time steps and fourth-order diffusion coefficients $K_4$ for the SE dynamical core in CAM 5. The subcycled dynamics time steps $\triangle\tau = \triangle t/m$, the number of subcycles $m$ and the physics time steps $\triangle t$ are listed.

| Resolution $n_e$ | Number of grid columns | Grid distance at equator (km) | Subcycled time step $\triangle\tau$ (s) | Number of subcycles $m$ | Physics time step $\triangle t$ (s) | Diffusion coefficient $K_4$ (m$^4$ s$^{-1}$) |
|---|---|---|---|---|---|---|
| 30 | 48,602 | 111 | 360 | 5 | 1800 | 1.0 $\times 10^{15}$ |
| 60 | 194,402 | 55 | 180 | 5 | 900 | 1.0 $\times 10^{14}$ |
| 120 | 777,602 | 28 | 75 | 6 | 450 | 1.0 $\times 10^{13}$ |

### 6.3.3 Eulerian Spectral Transform (EUL)

The EUL spectral transform model in vorticity-divergence form is based on the traditional three-time-level, semi-implicit spectral transform approximations applied on a quadratically unaliased Gaussian transform grid with triangular truncation (*Machenhauer*, 1979). The model was the default dynamical core in CAM version 3.1 and is now optional in CAM 4 and CAM 5. EUL includes the fourth-order ($\nabla^4$) hyper-diffusion in the horizontal directions to control the fluid flow at the smallest resolved scales. The $K_4$ diffusion coefficients are empirically chosen for each resolution to yield a reasonably straight tail for the kinetic energy spectra in model runs with parameterized physics (*Boville*, 1991). The model also includes a second-order $\nabla^2$

horizontal sponge-layer diffusion at the top three levels of the model to damp upward propagating waves. The temperature equation comprises a frictional heating term that takes the heating due to the explicit momentum diffusion into account. The Eulerian dynamical core applies an *a posteriori* mass fixer at every time step. The three-time-level leapfrog method includes a time filter to control the 2 $\triangle t$ computational modes of the time stepping scheme. No global energy fixer is utilized. The physics and dynamics packages are coupled via a process-split approach. EUL utilizes a monotonic semi-Lagrangian tracer transport scheme.

Table 6.3 lists the horizontal resolutions, time steps and $\nabla^4$ diffusion coefficients $K_4$ for the EUL dynamical core. The triangular truncation is abbreviated by T and is followed by the maximum resolvable wave number. The time step displays the dynamics time step. A subcycling mechanism for the dynamical core is optional in EUL, and is not invoked here. We call the physics package with the same $\triangle t$ frequency. However, due to the use of the leapfrog method the actual physics tendencies are applied for the duration of a $2\triangle t$ time interval since the previous $(n-1)$ time level is advanced to the future time level $(n+1)$ with the physics forcing evaluated at time level $n$. The base value of the $\nabla^2$ horizontal diffusion coefficient $K_2$ at the third level below the model top is set to 2.5 $\times 10^5$ m$^2$ s$^{-1}$ for all resolutions. This $K_2$ coefficient is doubled at the second level below the model top, and doubled again at the topmost level.

Table 6.3: Horizontal grid resolutions, time steps and fourth-order diffusion coefficients $K_4$ for the EUL dynamical core in CAM 5.

| Spectral resolution | No. of grid points lat $\times$ lon | Grid distance at equator (km) | Time step $\triangle t$ (s) | Diffusion coefficient $K_4$ (m$^4$ s$^{-1}$) |
|---|---|---|---|---|
| T85 | 128 $\times$ 256 | 156 | 600 | 1.0 $\times 10^{15}$ |
| T170 | 256 $\times$ 512 | 78 | 300 | 1.5 $\times 10^{14}$ |
| T340 | 512 $\times$ 1024 | 39 | 150 | 1.5 $\times 10^{13}$ |

### 6.3.4 Semi–Lagrangian Spectral Transform (SLD)

Another optional dynamical core in CAM 5 is the SLD spectral transform model. The dynamical core is based on two-time-level, semi-implicit semi-Lagrangian spectral transform approximations with quasi-cubic Lagrangian polynomial interpolants. A related three-time-level version of this dynamical core has been described in *Williamson and Olson* (1994). The SLD dynamical core is based on the same terrain following vertical coordinate as EUL and uses semi-Lagrangian advection in all directions. In the horizontal a triangular truncation is adopted with a quadratically unaliased Gaussian transform grid. SLD also includes the same horizontal $\nabla^4$ hyper-diffusion and $\nabla^2$ diffusion mechanisms as EUL. The $\nabla^2$ horizontal diffusion again serves as a sponge in the three top model levels. As in EUL, the energy lost by the explicitly added diffusion processes acts as a frictional heating term. An *a posteriori* mass fixer is invoked at every time step. Note that the semi-Lagrangian dynamical core applies a decentering technique to damp the noise induced by orographic resonance (see *Jablonowski and Williamson* (2011) for a review). The default CAM 5 decentering parameter is set to $\epsilon = 0.2$. No global energy fixer is applied. The physics and dynamics packages are coupled via a process-split approach.

The SLD dynamical core utilizes the same resolutions that are used for the EUL model (see Table 6.3). However, the time steps $\triangle t$ are three times the corresponding EUL values in Table 6.3. The dynamics and physics time steps are identical. The SLD dynamical core uses the same diffusion coefficients, $K_4$ and $K_2$, as the EUL package.

## 6.4 Motivation: Tropical cyclones in CAM 5 full-physics simulations

This section presents snapshots of CAM 5 full-physics simulations with each dynamical core to motivate the simulations and analysis of the simple-physics setup. A detailed description of the CAM 5 physics suite can be found in *Neale et al.* (2010b). The initial conditions that trigger the evolution of an idealized tropical cyclone are discussed in Chapter II. As shown below, the choice of the dynamical core has a strong impact on the 10-day simulations of the tropical storm despite the use of the identical physics package. This triggers the question whether the differences can be attributed to the characteristics of the dynamical cores, and whether the results with simpler physical forcings can replicate at least some of the differences. If yes, it might provide a pathway for an improved understanding of the highly nonlinear physics-dynamics interplay. The latter is difficult to disentangle in complex full-physics experiments. Previous high-resolution simulations with CAM 5 have shown that FV simulates intense tropical cyclones with many realistic features (*Reed and Jablonowski*, 2011c). Therefore, we suggest that the CAM 5 model experiments presented here and in section 6.5 provide a suitable basis for a dynamical core intercomparison, and challenge our understanding of both the full- and simple-physics simulations.

Figure 6.2 displays the wind speed at day 10 for the CAM 5 simulations using FV at 0.25°, SE at $n_e = 120$, EUL at T340 and SLD at T340. The left column of Fig. 6.2 shows the longitude-height cross sections of the magnitude of the wind through the center latitude of the vortex. The right column of Fig. 6.2 displays the horizontal cross sections of the magnitude of the wind at 100 m. The center of the vortex is defined to be the grid point with the minimum surface pressure. At day 10 the storm resembles a tropical cyclone with maximum wind speeds near the surface, a relatively calm eye and a warm-core (not shown) for each CAM 5 dynamical core. However, there

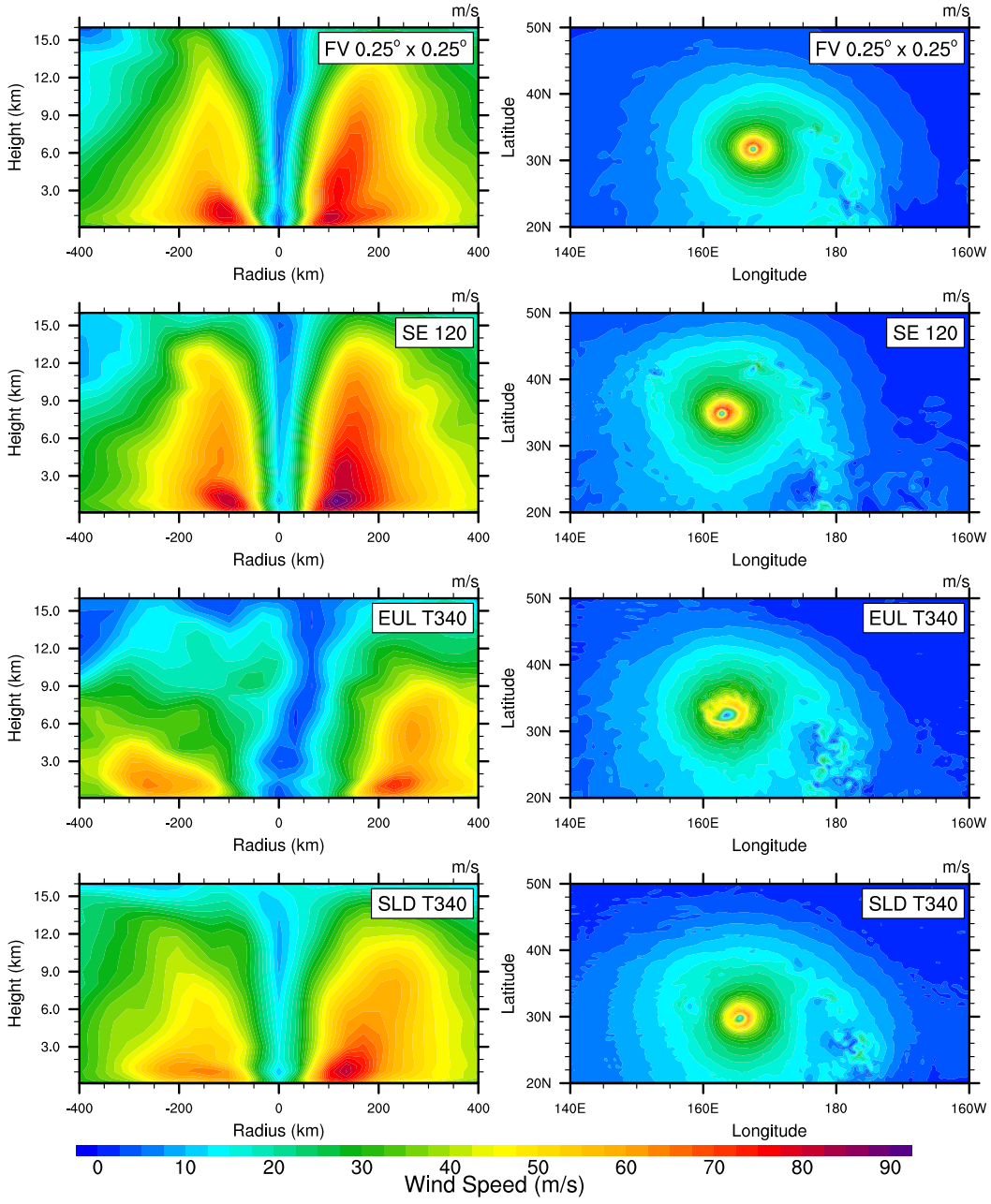


Figure 6.2: Snapshot of the tropical cyclone at day 10 for each dynamical core (FV, SE, EUL and SLD) with full CAM 5 physics at the highest respective resolution and L30 used for this study (as labeled). Left column: longitude-height cross section of the wind speed through the center latitude of the vortex as a function of the radius from the vortex center. Right column: horizontal cross section of the wind speed at a height of 100 m.

is large variance amongst the dynamical cores in the cyclone intensity, the radius of maximum wind (RMW) and overall organization. In general, the FV and SE models produce a stronger storm with a smaller RMW when compared to the EUL and SLD dynamics packages. In addition, the SE package seems to produce more small-scale features when compared to FV as suggested by FV's slightly smoother contour lines. We speculate that this might be attributable to SE's higher-order (fourth-order) numerical scheme in the horizontal directions that has the potential to provide a higher nominal resolution and sharper gradients than FV. The EUL T340 dynamical core appears to simulate the weakest, least organized storm of the four dynamical cores at these high horizontal resolutions. Its RMW is the widest among the four models. There are also differences in the location of the center of the storm by day 10. This is attributed to the variance in the storm intensity and its impact on the storm's motion, which is impacted by the beta-drift effect.

The time evolution of the minimum surface pressure in the CAM 5 full-physics simulations is provided in Figure 6.3. Each dynamical core is run at the resolutions provided in Tables 6.1-6.3. From Figure 6.3 it is evident that as the horizontal resolution increases within each dynamical core the intensity of the simulated tropical cyclone increases. In all dynamical cores but EUL, there appears to be no hint of convergence of the storm intensity with increasing resolution. The EUL package might tend towards a converged simulation as the simulation at T170 and T340 approach the same minimum surface pressure at day 10. However, while the two simulations appear to reach similar values at day 10 the path to development varies. This is evidenced by the fact that the EUL T340 simulation starts to intensify earlier in the simulation than the EUL T170 simulation. In addition, all four dynamical cores show an earlier onset of intensification with increasing resolution.

Again, Figure 6.3 demonstrates that at the highest resolutions, the FV and SE dynamical cores produce stronger cyclones at day 10 than the EUL and SLD dynamics

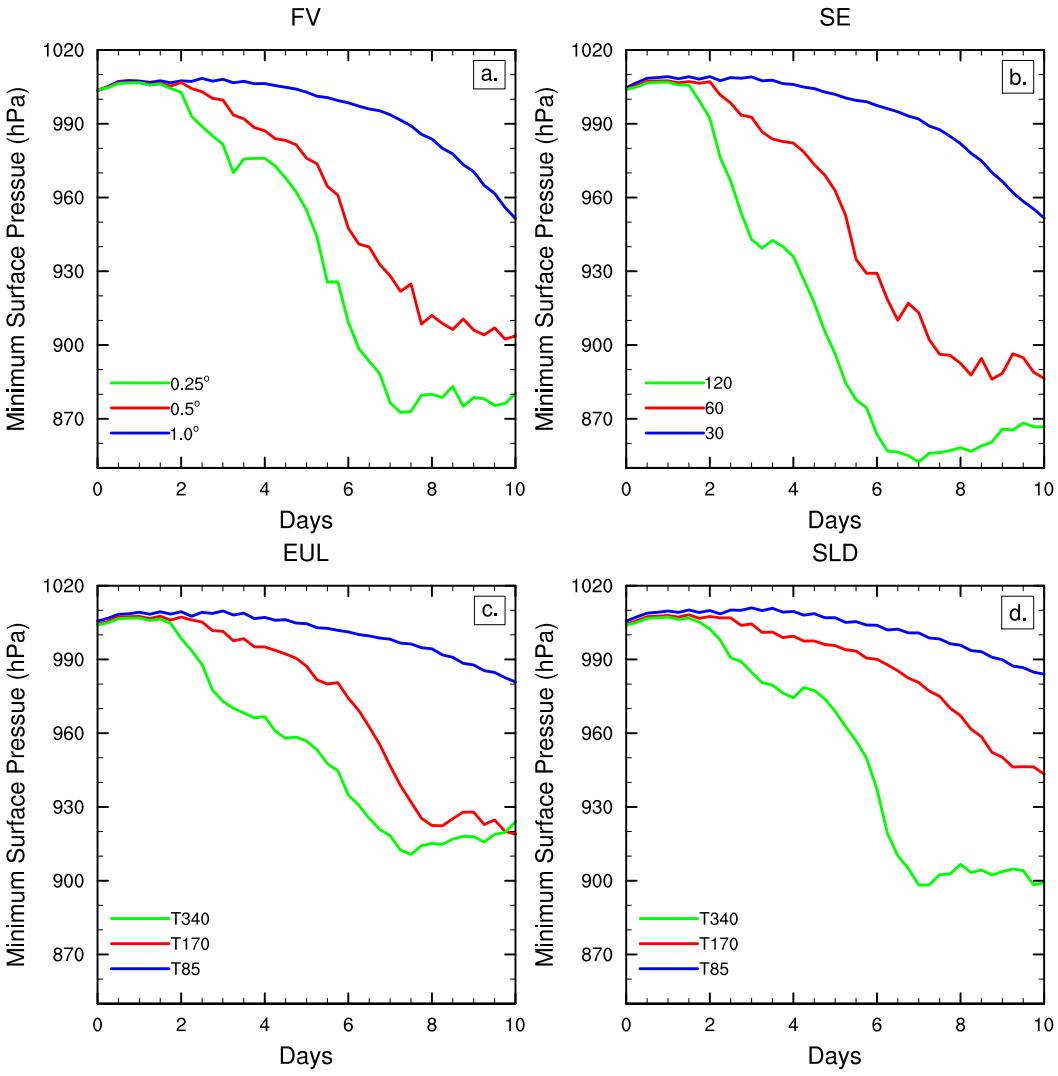


Figure 6.3: Time evolution of the minimum surface pressure of the tropical cyclone with full CAM 5 physics and the (a) FV, (b) SE, (c) EUL and (d) SLD dynamical cores. These L30 simulations use the horizontal resolutions provided in Tables 6.1-6.3.

packages. In general, the SE model produces the most intense tropical cyclones by day 10, and may approach unphysical minimum surface pressures at the resolution $n_e = 120$ when compared to observations. For example, the minimum surface pressure in the SE $n_e = 120$ run drops to values around 852 hPa at day 7 which are rather extreme. The lowest resolution simulations with each dynamics package all fail to completely develop over 10 simulation days, but again the FV and SE simulations develop further, as evidenced by lower surface pressures. It appears that the FV and SE dynamical cores require less horizontal resolution to simulate tropical cyclones with similar intensity to the EUL and SLD dynamical cores at higher resolutions. As an example the FV 0.5° and SE $n_e = 60$ simulations, that have grid spacings of approximately 55 km at the equator, produce similar storm intensities to the EUL T340 and SLD T340 simulations with roughly 39 km grid spacings at the equator. This is further shown in Table 6.4 which provides the day 10 values of the minimum surface pressure (MSP), maximum wind speed at 100 m, and center location of the tropical cyclone for all dynamical core simulations. We hypothesize that the stronger intensity of the storms could be related to the local spatial discretization techniques in the FV and SE dynamics packages, that are likely to represent locally strong gradients more reliably in contrast to the global spectral transform method in EUL and SLD.

## 6.5 Simple-physics simulations

This section presents the idealized tropical cyclone simulations of all four CAM 5 dynamical cores when coupled to the simple-physics suite. The purpose of the section is threefold. First, we assess the evolution of the tropical cyclone in FV and briefly describe the general characteristics of the simulation in section 6.5.1. The main aspects to consider are whether the simple-physics processes provide a suitable forcing to drive the intensification of the initial storm, and whether the tropical storm exhibits realistic features like a calm eye or slanted eye wall. Second, we

Table 6.4: Various statistics, including minimum surface pressure (MSP), maximum wind speed (MWS) at 100 m, and center location, of the tropical cyclone at day 10 for the simulations using full CAM 5 physics with each dynamical core and resolution with L30.

| Model | Resolution | MSP (hPa) | MWS (m $s^{-1}$) | Location |
|---|---|---|---|---|
| FV | 1.0° × 1.0° | 951.47 | 39.02 | (169°E, 29°N) |
| | 0.5° × 0.5° | 903.72 | 59.53 | (170.5°E, 29.5°N) |
| | 0.25° × 0.25° | 880.24 | 66.96 | (167.5°E, 31.75°N) |
| SE | 30 | 951.66 | 38.68 | (170°E, 29.83°N) |
| | 60 | 886.42 | 66.92 | (167°E, 34.90°N) |
| | 120 | 866.81 | 73.18 | (162.75°E, 34.95°N) |
| EUL | T85 | 980.88 | 28.22 | (170.16°E, 30.12°N) |
| | T170 | 918.94 | 53.22 | (163.83°E, 29.82°N) |
| | T340 | 923.96 | 54.62 | (163.48°E, 32.49°N) |
| SLD | T85 | 983.98 | 22.89 | (170.16°E, 28.72°N) |
| | T170 | 943.34 | 41.49 | (167.34°E, 29.82°N) |
| | T340 | 899.15 | 63.52 | (165.59°E, 30.03°N) |

provide snapshots of the dynamical core intercomparison with FV, SE, EUL and SLD in section 6.5.2. This reveals the impact of the dynamical core on the simplified simulations, and also assesses the convergence-with-resolution characteristics. The overarching question is whether such simple-physics experiments can help shed light on physics-dynamics interactions and whether there are similarities to full-physics runs. Third, we estimate the uncertainty of the simulations via a perturbed initial-data ensemble approach with FV (section 6.5.3). The latter provides insight into the robustness of the tropical cyclone simulations and the simple-physics test scenario.

Throughout the section, comparisons to the CAM 5 full-physics simulations are made. However, we do not expect to replicate the full-physics simulations, which is of course not feasible. Rather, we are interested in the general behavior of the four dynamical cores, and whether some of the sensitivities seen in full-physics simulations are present in simpler experiments. The aim is to test whether the simple-physics forcing is a suitable tool for model evaluations of intermediate complexity, and to provide an estimate of the robustness of the test case.

### 6.5.1 Evolution of the FV tropical cyclone at 0.25°

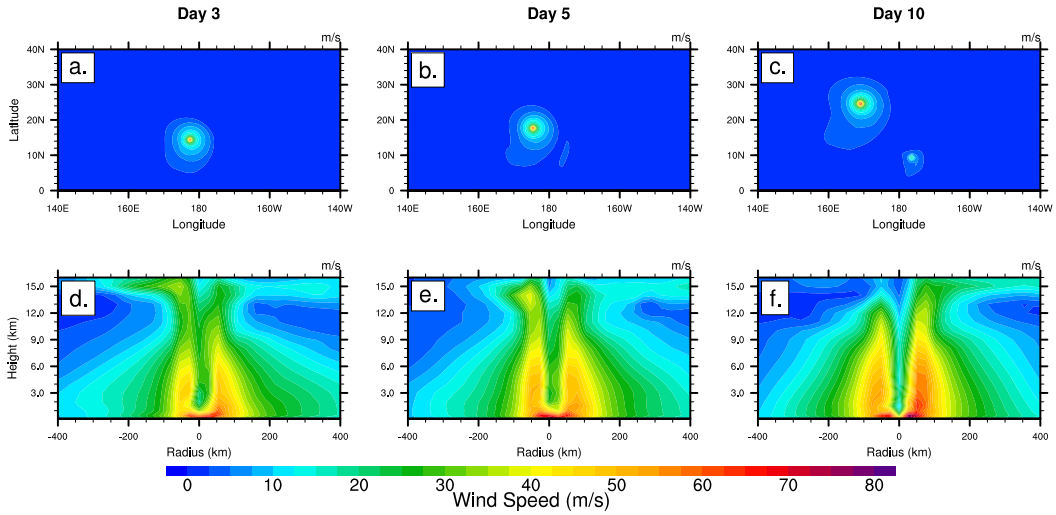


Figure 6.4: Snapshots of the tropical cyclone at day 3 (left), 5 (middle) and day 10 (right) with CAM 5 FV at the resolution 0.25° L30 for simple-physics. Top row (a-c): horizontal cross section of the wind speed at a height of 100 m. Bottom row (d-f): longitude-height cross section of the wind speed through the center latitude of the vortex as a function of the radius from the vortex center.

Figure 6.4 shows the development of the wind speed from the initial vortex for the FV 0.25° simple-physics simulation, with specific snapshots at days 3, 5 and 10. The top row (a-c) of Fig. 6.4 displays the horizontal cross section of the magnitude of the wind at 100 m. The bottom row (d-f) of Fig. 6.4 shows the longitude-height cross section of the magnitude of the wind through the center latitude of the vortex. Figure 6.4 offers a direct comparison to the evolution of the tropical cyclone with full CAM 5 physics as shown in *Reed and Jablonowski* (2011c) and Fig. 6.2 (top row). From Fig. 6.4 it is evident that the initial vortex has developed into a strong cyclone by day 3. The storm is compact and has a defined calm eye region, especially at upper levels, and has a maximum wind speed at 100 m of 73.34 m $s^{-1}$ by day 10 (as listed later in Table 6.5). Figure 6.4 shows that the maximum wind speed occurs near the surface at the RMW, which is characteristic of tropical cyclones. In addition, the cyclone is a warm-core system (not shown).

When compared to the development of the CAM 5 full-physics storm in *Reed and Jablonowski* (2011c) (their Fig. 3), the simple-physics simulation is more compact, as indicated by a smaller RMW and reduced horizontal extent of the storm. This is most likely a result of the simplicity of the simple-physics package. However, the simple-physics simulation still produces an intense cyclone. The results suggest that the simple-physics suite provides suitable forcing mechanisms for the tropical cyclone, and thereby qualifies as an evaluation technique of intermediate complexity.

### 6.5.2 Dynamical core intercomparison

Figure 6.5, like Fig. 6.2, displays the wind speed at day 10, but now as simple-physics simulations using FV at 0.25°, SE at $n_e = 120$, EUL at T340 and SLD at T340. A quick comparison of the results in Fig. 6.5 to those in Fig. 6.2 shows a substantial difference between the simple-physics and CAM 5 full-physics simulations. Such differences include variations in the intensity, structure and size of the storm at day 10 for each dynamical core. In particular, all simple-physics storms are weaker than the full-physics storms, and their horizontal extent is smaller. As mentioned before these differences are expected and not the focus of the discussion here. For example, *Reed and Jablonowski* (2011b,c) already highlighted that structural differences of models, such as different physical parameterization suites, produce substantial variance in the evolution of the initial vortex into a tropical cyclone over ten simulation days.

Of particular interest here is whether there are similarities in the general characteristics of the storm when comparing the simple-physics and full-physics results of all dynamical cores. Figure 6.5 reveals such similarities. For example, the simple-physics simulations at the highest resolution with the FV and SE models produce more intense storms with smaller RMW in comparison to the cyclones in the EUL and SLD experiments. The RMW is always the widest in EUL as also shown later for other resolutions. In addition, the SE dynamical core produces the strongest storm

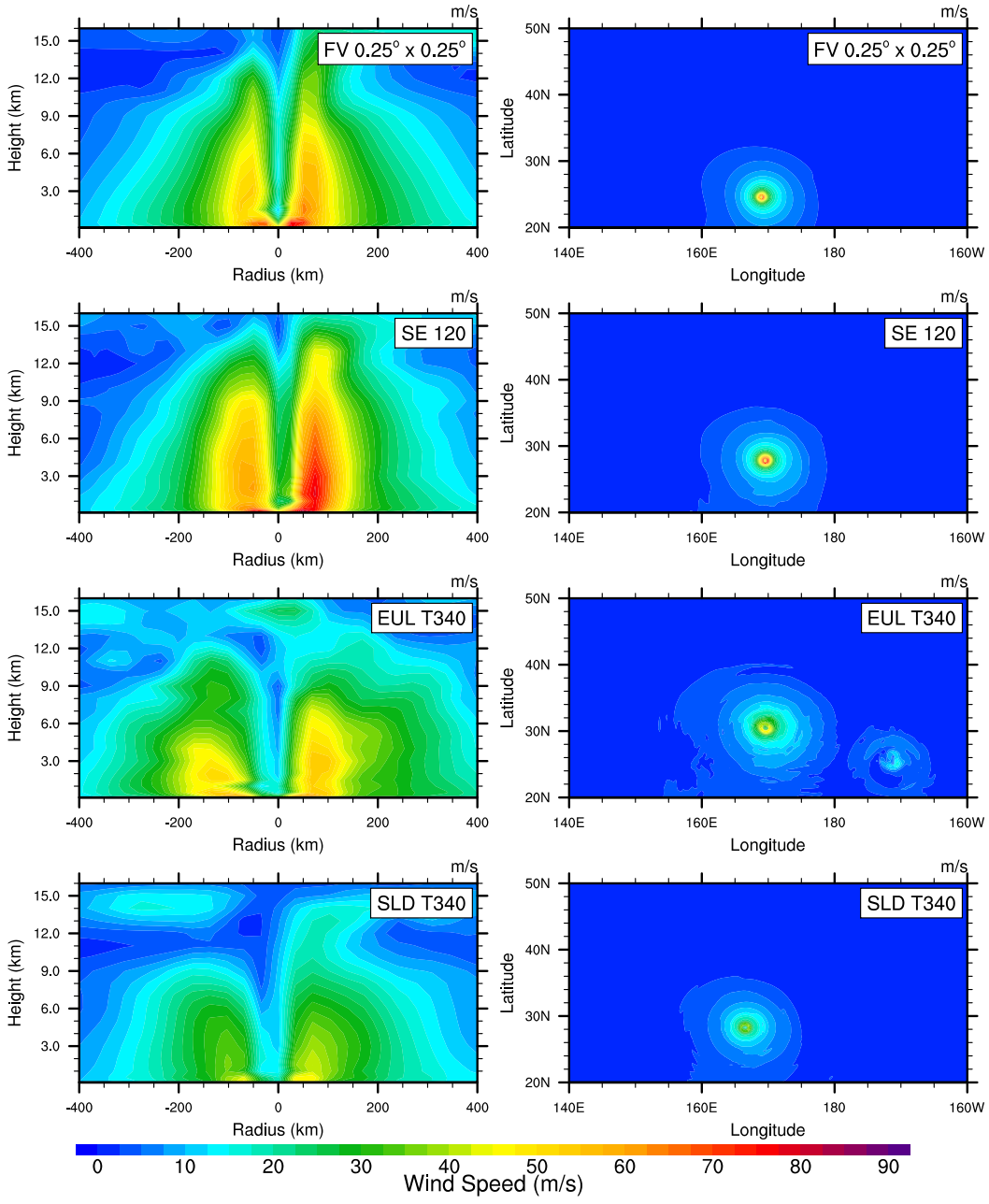


Figure 6.5: Same as Fig. 6.2 but for the simple-physics simulations.

by day 10, as seen by the maximum wind speed. When comparing the characteristics of the wind speeds in the vertical direction in Figs. 6.5 and 6.2, it is evident that the strong winds in the FV and SE models reach higher up into the atmosphere in both the simple-physics and full-physics experiments, despite the identical vertical grid and number of levels in all models.

Figure 6.6 presents the time evolution of the minimum surface pressure for each dynamical core and resolution with simple-physics, and can be compared to the characteristics of the full-physics runs in Fig. 6.3. Generally speaking, the storms in FV and SE at all "equivalent" resolutions, according to the climate analysis by *Williamson* (2008a) (e.g. 0.25° and T340 are equivalent), are stronger than the storms in EUL and SLD. The SE package consistently produces more intense tropical cyclones. In addition, EUL generates stronger storms than SLD, except this similarity does not hold at the highest T340 resolution in the full-physics simulation. This general behavior could be related to the diffusion characteristics of the dynamical cores, since SLD is likely affected by enhanced numerical diffusion due to the semi-Lagrangian interpolations and its decentering mechanism. However, more in-depth analyses are necessary to test this hypothesis. As an aside, we note that the simple-physics simulations contain more temporal variations in the storm intensity in comparison to full-physics runs, as seen by the evolution of the minimum surface pressure in Fig. 6.6. It is likely that these variations are partially a result of the reduced nature of the precipitation processes in simple-physics since the large-scale condensation parameterization is either active or not depending on supersaturation.

Figure 6.6 shows that for each dynamics package as the resolution increases so does the intensity of the storm. This is furthermore evidenced by the day-10 maximum wind speed at 100 m and minimum surface pressure values provided in Table 6.5. When compared to Table 6.4, the maximum wind speeds at 100 m in Table 6.5 are often of the same order despite larger values for the minimum surface pressure. This

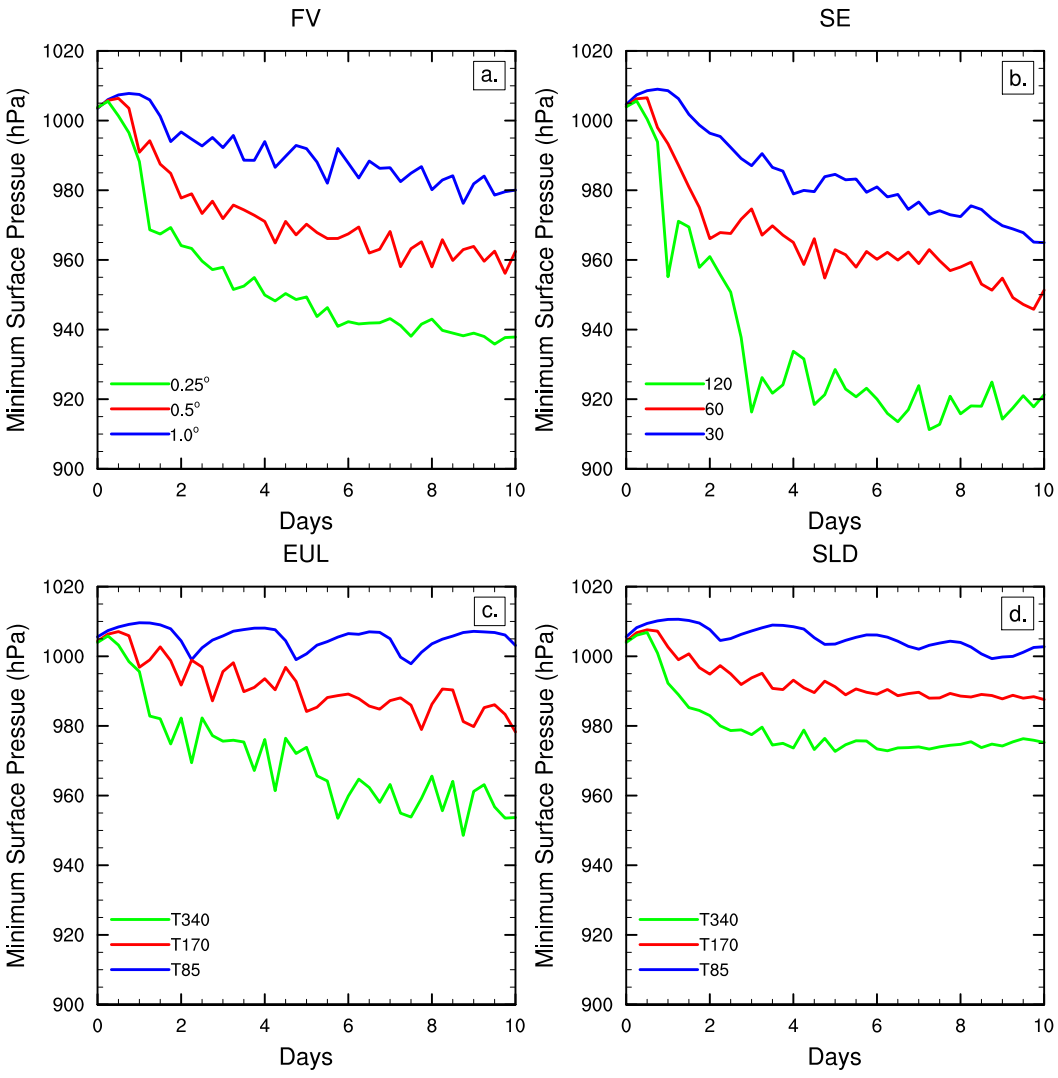


Figure 6.6: Same as Fig. 6.3 but for the simple-physics simulations.

can be attributed to differences in the storm's structure, mainly the location of the RMW and the lower height of the wind maximum in the simple-physics experiments. The lower height of the maximum wind speed thereby impacts the interpolated wind speeds at 100 m. In addition, Fig. 6.6 displays that the onset of the intensification, shown by the deepening of the minimum surface pressure, occurs sooner as the resolution increases within each dynamical core. There is no sign of convergence with resolution for any of the dynamical cores with simple-physics. The latter two aspects are also present in the full-physics simulations. Figure 6.6 appears to provide additional evidence that smaller grid spacings are required for the EUL and SLD models to produce comparable results to the FV and SE packages. For example, the EUL and SLD T170 simulation produce similar intensities by day 10 as the FV 1.0° and SE $n_e = 30$ simulations. Again, we speculate that this general characteristic might be related to the very different nature of the numerical discretizations. Both the FV and SE models utilize a local discretization technique in the horizontal directions which might be more favorable for the representation and intensification of such a localized storm in comparison to the global spectral method in EUL and SLD.

Table 6.5: Same with Table 6.4 but for the simulations using simple-physics with each dynamical core and resolution.

| Model | Resolution | MSP (hPa) | MWS (m $s^{-1}$) | Location |
|---|---|---|---|---|
| FV | 1.0° × 1.0° | 980.04 | 30.77 | (170°E, 25°N) |
| | 0.5° × 0.5° | 962.45 | 42.87 | (169°E, 24.5°N) |
| | 0.25° × 0.25° | 937.86 | 73.34 | (169°E, 24.5°N) |
| SE | 30 | 964.95 | 42.97 | (167°E, 33.81°N) |
| | 60 | 951.22 | 50.11 | (168.5°E, 30.41°N) |
| | 120 | 921.29 | 76.61 | (169.5°E, 27.71°N) |
| EUL | T85 | 1003.10 | 15.0 | (168.75°E, 24.51°N) |
| | T170 | 978.28 | 33.40 | (172.27°E, 27.02°N) |
| | T340 | 953.71 | 48.36 | (169.80°E, 30.38°N) |
| SLD | T85 | 1002.75 | 14.29 | (170.16°E, 27.31°N) |
| | T170 | 987.58 | 25.32 | (168.05°E, 27.72°N) |
| | T340 | 975.24 | 38.22 | (166.64°E, 28.27°N) |

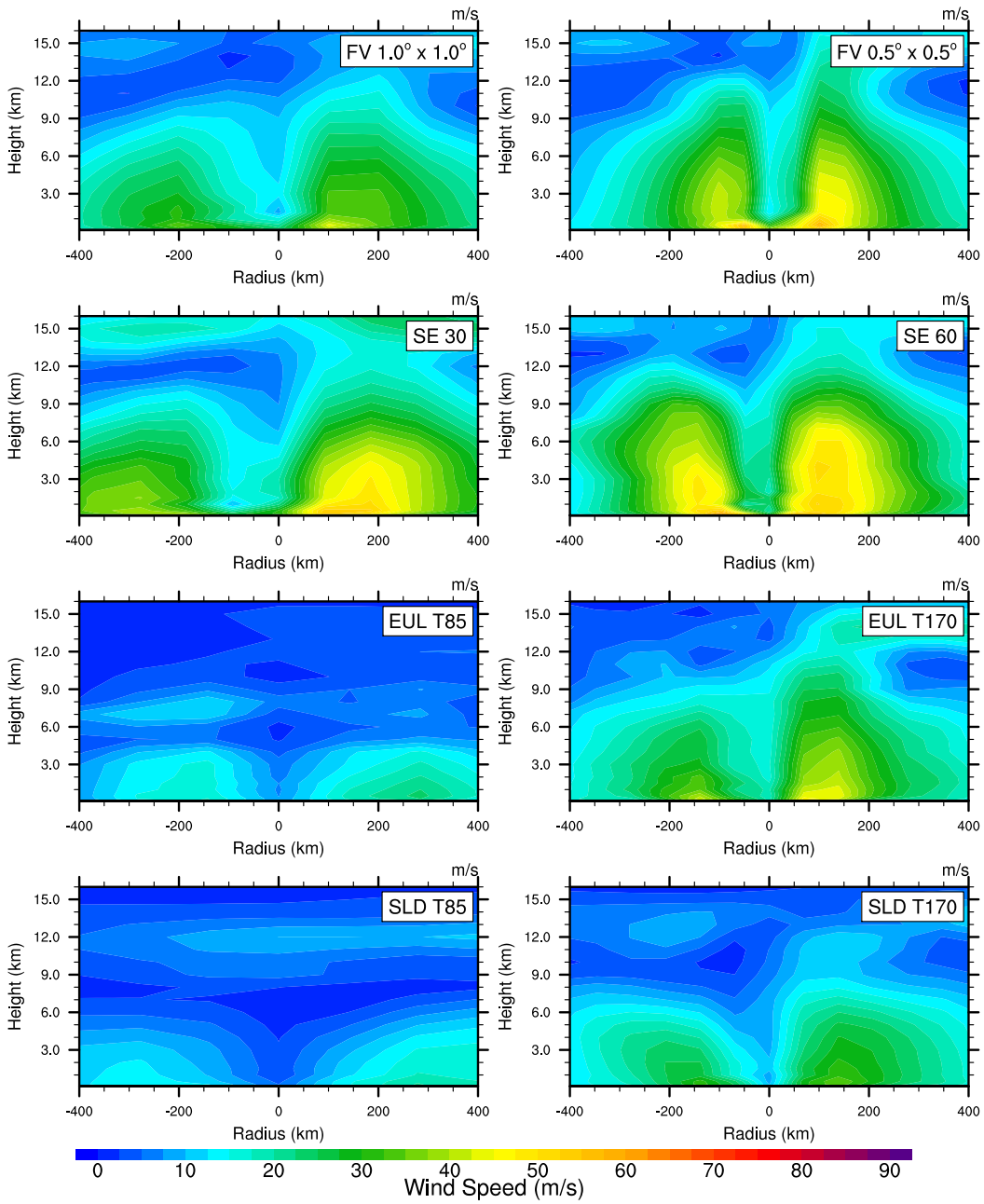


Figure 6.7: Snapshot of the tropical cyclone at day 10 for FV, SE, EUL and SLD with simple-physics at the remaining horizontal resolutions (as labeled, with L30) not shown in Fig. 6.5. The results are displayed as a longitude-height cross section of the wind speed through the center latitude of the vortex as a function of the radius from the vortex center.

To complete the overall assessment Fig. 6.7 displays the day-10 longitude-height cross sections of the wind speed at the lower resolutions not shown in Fig. 6.5 for all four dynamical cores. When comparing the results in Fig. 6.7 with the right column of Fig. 6.5 is is evident that as the horizontal resolution increases the simulated storm becomes more intense and compact. Again, when comparing dynamical cores, but now the storm structure, it appears that the EUL and SLD T170 simulations are similar to the FV 1.0° and SE $n_e = 30$ simulations and the EUL and SLD T340 simulations are similar to the FV 0.5° and SE $n_e = 60$ simulations. This is consistent with the results seen earlier in Fig. 6.6. Note, in agreement with Fig. 6.6, the EUL and SLD T85 simulations fail to develop in the 10-day simulation. This is in contrast to CAM 5 full-physics simulations in which the EUL and SLD T85 storms do develop somewhat during the ten simulation days.

In summary, many general characteristics of the simple-physics simulations with all four dynamical cores are consistent with those seen in CAM 5 full-physics experiments. This encourages us to suggest that simple-physics provides a suitable physics parameterization suite to compare the impact of numerical schemes, meshes and diffusion properties on tropical storms or other flow fields.

### 6.5.3 Ensemble simulations

Our final assessment of the simple-physics suite analyzes the spread of the simulations due to small perturbations. Such ensemble runs evaluate the robustness of the unperturbed control simulation presented earlier, and provide valuable information about its uncertainty. This emphasizes that a single deterministic simulation without an uncertainty estimate has only limited significance.

This section presents the results of 11 ensemble simulations with the FV dynamical core with simple-physics. The 11 ensemble simulations consist of the control case with unperturbed initial conditions, eight simulations with random perturbations to the

initial conditions and two simulations in which the longitudinal position of the center of the control vortex is shifted by $\Delta\lambda/2$ and $\Delta\lambda/4$. The eight perturbation simulations are initialized with the control vortex that is overlaid with random small-amplitude perturbations of the initial global zonal and meridional wind velocities. The random perturbations are at most $\pm 0.4$ m s$^{-1}$. The simulations with the shift in the initial location of the vortex center produce small, more systematic variations in all initial fields, since they are analytically evaluated at the grid point locations. In particular, it means that the center of the vortex now no longer coincides with a FV grid point. These shifts thereby mimic the uncertainty related to the choice of the computational grid. This choice of ensemble simulation is consistent to the initial-data uncertainty runs shown in *Reed and Jablonowski* (2011c) for FV simulations with the full CAM 5 physics suite. Note, that the parameter-uncertainty runs in *Reed and Jablonowski* (2011c) are not repeated in this paper, as the study demonstrated that there is no distinction between the initial-data and parameter uncertainty results.

Figure 6.8 displays the time evolution of the maximum 100 m wind speed of the simple-physics ensemble runs with FV at the horizontal resolutions (a) 1.0°, (b) 0.5° and (c) 0.25°. The control case is represented by the bold blue line, the eight runs with random perturbations to the initial wind speeds are represented by the red lines and the two runs with the shift in the initial center longitude of the vortex are represented by the green lines. It is evident from Fig. 6.8 that the spread in the simulations increases with increasing resolution. In fact, at the lowest 1.0° resolution there is almost no spread due the random perturbation simulations and the spread is only due to the simulations with the shift in the initial longitude of the center of the vortex. When compared to the CAM 5 FV simulations in *Reed and Jablonowski* (2011c) (their Fig. 8), the variations in the ensemble simulations with simple-physics are smaller at 1.0° and 0.5°. However, the variance at the horizontal resolution of 0.25° seems to be comparable for the CAM 5 full-physics and simple-physics simulations.

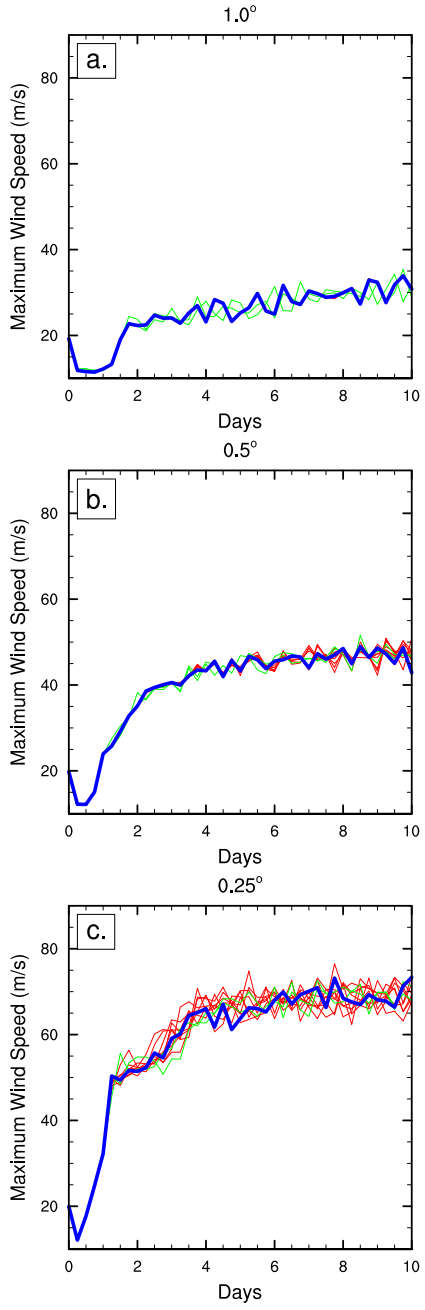


Figure 6.8: Time evolution of the maximum wind speed at 100 m of the ensemble simulations with simple-physics at FV (a) 1.0°, (b) 0.5° and (c) 0.25° with L30. The bold blue line represents the unperturbed control case, the red lines represent the eight runs with random perturbations to the initial zonal and meridional wind speeds and the green lines represent the two runs with the shift in the initial center longitude of the vortex.

In addition, as the resolution increases the onset of the spread occurs earlier in the evolution of the vortex. At the higher resolutions there is no distinction between the two types of initial-data uncertainty.

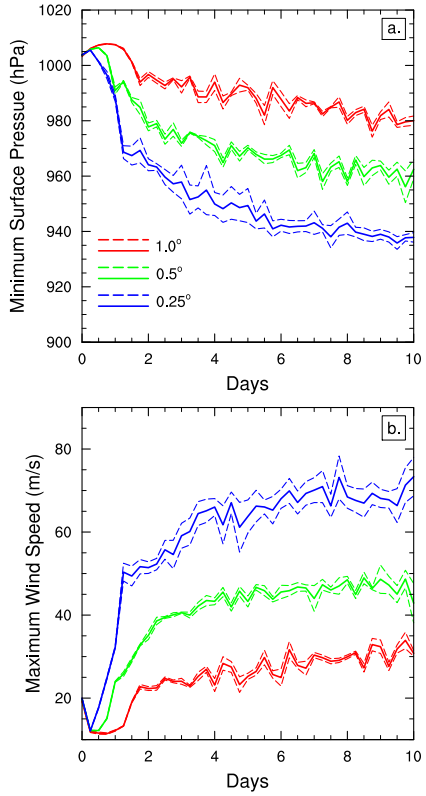


Figure 6.9: Time evolution of the minimum surface pressure (top) and maximum wind speed at 100 m (bottom) of the control case at the horizontal resolutions of the FV 1.0° (red), 0.5° (green) and 0.25° (blue) with simple-physics (L30). The solid line represents the unperturbed control case, the dashed lines represent the variance as determined by the ensemble RMSD.

Figure 6.9 represents the spread in the simple-physics simulations as the root-mean-square deviation (RMSD) of the eight initial-data ensemble simulations from the control simulation. The evolution of the (a) minimum surface pressure and (b) the maximum 100 m wind speed for the control run are shown as the solid line and the dashed lines represent the ensemble RMSD from the control case at any given time. Again, the increase in spread with resolution is obvious in both the minimum surface pressure and the maximum wind speed. From Table 6.6, which shows various

Table 6.6: Various ensemble characteristics for the minimum surface pressure and the maximum wind speed at 100 m for the simple-physics ensemble simulations at 1.0°, 0.5° and 0.25° (L30): maximum absolute spread among all ensemble members, root-mean-square deviations (RMSD) of 10 ensemble members to the control simulation at day 10, and the maximum RMSD during the 10-day simulation.

Minimum surface pressure

| | Max spread | RMSD at day 10 | Max RMSD |
|---|---|---|---|
| $1.0° \times 1.0°$ | 11.05 hPa | 1.68 hPa | 3.46 hPa |
| $0.5° \times 0.5°$ | 8.73 hPa | 3.45 hPa | 5.74 hPa |
| $0.25° \times 0.25°$ | 16.69 hPa | 1.71 hPa | 8.87 hPa |

Maximum wind speed

| | Max spread | RMSD at day 10 | Max RMSD |
|---|---|---|---|
| $1.0° \times 1.0°$ | 7.57 m $s^{-1}$ | 0.70 m $s^{-1}$ | 2.05 m $s^{-1}$ |
| $0.5° \times 0.5°$ | 7.98 m $s^{-1}$ | 4.74 m $s^{-1}$ | 4.74 m $s^{-1}$ |
| $0.25° \times 0.25°$ | 12.13 m $s^{-1}$ | 4.62 m $s^{-1}$ | 5.99 m $s^{-1}$ |

ensemble characteristics, it is evident that the maximum RMSD increases with resolution for both the surface pressure and wind speed. The table also shows that in most cases the absolute spread among the ensemble members increases with resolution as well. We define the absolute spread as the maximum deviation between all ensemble members at any given snapshot in time.

Figure 6.9 provides a sense of the robustness of the control case. At all resolutions, the control case provides a reasonable representation of the tropical cyclone. Therefore, the differences between the dynamical cores discussed in the previous section are valid even when including initial-data uncertainty. The simple-physics experiments produce a smaller ensemble spread, especially at the lower resolutions, than corresponding CAM 5 full-physics simulations. This is likely a result of the reduced complexity of the simple-physics forcing. Based on these ensemble results we again conclude that the simple-physics suite provides a suitable test scenario for dynamical core evaluations with moisture processes.

## 6.6 Summary and conclusions

This paper introduced a reduced-physics parameterization suite for AGCMs that we call "simple-physics". Simple-physics is intended to serve as a test scenario of intermediate complexity in order to build bridges between dry dynamical core assessments and moist full-physics aqua-planet and AMIP studies. Such an intermediate-complexity assessment is a missing link in the current test hierarchy, especially when evaluating the impact of the dynamical core on moist AGCM simulations.

The simplified physics suite includes parameterizations of bulk aerodynamic surface fluxes for moisture, sensible heat and momentum, vertical diffusion in the boundary layer, and large-scale condensation. It thereby contains the important driving mechanisms for tropical cyclones that serve as a specific test case. However, the simple-physics setup can also be used for other flow fields such as the analysis of mountain-induced precipitation patterns. The aims of the paper were threefold. First, we introduced all details of the simple-physics parameterization suite to ensure that it can be implemented in other models. Second, we implemented the simple-physics suite in the four dynamical cores FV, SE, EUL and SLD of NCAR's CAM 5 model, and utilized an idealized tropical cyclone test case to demonstrate the general characteristics of the simple-physics experiments. These simplified simulations were motivated by the observation that the choice of the AGCM dynamical core has a substantial impact on deterministic tropical cyclone simulations with full-physics CAM 5 in aqua-planet mode. The overarching questions were whether there are general similarities between the simple-physics and full-physics tropical cyclone simulations, and if yes whether simple-physics experiments can help shed light on the highly nonlinear physics-dynamics interplay. This might help disentangle the impact of the dynamical core in moist simulations which is difficult to evaluate in isolation in complex full-physics experiments. Third, we estimated the uncertainty of the simulations via a perturbed initial-data ensemble approach. The latter provides insight into the

robustness of the tropical cyclone simulations and the simple-physics test scenario.

As expected, the simple-physics and full-physics tropical cyclone simulations show distinct differences in the structure, intensity and path of the developing storm over the 10-day simulation period. In general, the simple-physics suite produces weaker and smaller storms. These differences are due to the simplicity of the simple-physics suite and not the focus of the discussion here. Rather, the following key results were obtained which focus on the general characteristics and similarities of the simulations with both simple-physics and full-physics.

- At the highest resolutions used in this study, FV at 0.25°, SE at $n_e = 120$, EUL at T340 and SLD at T340, all four dynamical cores produce a tropical cyclone by day 10. However, there are significant differences among them that are triggered by the dynamical core and its physics-dynamics interactions.

- The tropical cyclone in the FV at 0.25° and SE at $n_e = 120$ simulations is stronger and more compact (smaller RMW) by day 10 when compared to the EUL and SLD T340 experiments. The storm in the SE simulations is always the strongest. EUL always shows the widest RMW.

- Within each dynamical core the simulated storm becomes more intense and compact with increasing resolution. There is no sign of convergence. With increasing resolution the intensification of the tropical cyclone occurs earlier in the simulation.

- The uncertainty of the simple-physics simulations is reduced at lower resolutions in comparison to full-physics runs. At high resolutions with about 28-39 km grid spacings the uncertainty is comparable. This is likely an advantage of the simple-physics package and implies that simulations with the control vortex in the dynamical core comparisons are robust.

- The results suggest that EUL and SLD require decreased grid spacings to produce comparable results to lower-resolution experiments with FV and SE.

We suggest that the combination of simple-physics and the analytic vortex initialization technique provides a suitable basis for a test case of intermediate complexity for AGCMs. Such a test case is currently absent in the hierarchy of AGCM evaluations and developments. Using the unique framework of CAM 5 with its four dynamical cores this study has shown that the test case might be a suitable candidate for dynamical core intercomparisons.

In addition, previous studies have shown that tropical cyclones are very sensitive to physics parameterizations which makes intercomparisons of simulations with different physics packages difficult. The test case presented here allows for simplified process studies within the physics suite. For example, the sensitivity of the results to the surface flux formulation or its coefficients can easily be tested. The physics forcings can also be easily replaced by different mechanisms. This may prove to be useful for intercomparisons of AGCMs across the community, as the physics parameterization suites often vary greatly amongst different models. It may also be of particular importance with respect to the advancements in modern computer architectures that now enable AGCMs to run at higher resolutions than ever before. At these high resolutions in the km range, phenomena like tropical cyclones will likely become resolved features. As a result, it is important that the ability of such AGCMs to simulate tropical cyclones be tested during the development and evaluation stages. The test case introduced here might therefore prove to be useful in this manner.

Future work will consist of implementing the intermediate-complexity test case into other AGCM frameworks to promote model intercomparisons and in-depth analyses of the causes and effects of the modeling choices on moist simulations. In addition, the use of variable-resolution techniques, such as adaptive mesh refinement, for AGCMs is becoming a novel model design choice. The test case will be used to aid

in the development of such techniques.

# CHAPTER VII

# Conclusions

With the advancement of modern parallel computer architectures, general circulation models (GCMs) are becoming capable of running operationally at higher horizontal resolutions than ever before. At horizontal resolutions of 0.5° (roughly 55 km near the equator) or finer, GCMs have been successful at simulating extreme weather events such as tropical cyclones. Over the coming decade the use of GCMs to simulate such extremes is likely to become even more prominent. Such GCM simulations will be instrumental in understanding the potential societal and economic impacts of extreme weather events and how these impacts will evolve over the coming decades as a result of climate change.

High-resolution GCMs are becoming the tool of choice to evaluate tropical cyclones in current and future climate conditions. This raises questions concerning the fidelity of GCMs for tropical cyclone assessments. In particular, the physical and dynamical components of GCMs need to be carefully evaluated to assess their reliability for tropical cyclone studies. This includes studying the impact of GCM design choices of numerical schemes, grid meshes, diffusion properties and physical parameterizations on simulated storms.

There is no doubt that extreme weather events, such as hurricanes, are among the most destructive and costliest of atmospheric phenomena. Through the use of

high-resolution GCMs, it is possible to gain a better understanding of how well these extreme events can be simulated and what improvements need to be made in GCM development to improve simulation of tropical cyclones.

## 7.1 Summary

The work in this thesis investigates the ability of NCAR's Community Atmosphere Model CAM to simulate tropical cyclones at high resolutions under various model configurations. A vortex initialization technique is used to initiate CAM for a series of process studies that test the reliability of the model's numerical schemes, physical parameterizations and horizontal resolution for the simulation of tropical cyclones.

Chapter II introduces the design of idealized tropical cyclone experiments in GCMs using a vortex initialization that is built upon prescribed 3D fields in an idealized tropical environmental. The evolution of an initially weak, warm-core vortex is investigated over a 10-day time period with varying initial conditions that include variations of the maximum wind speed and radius of maximum wind. Using the finite–volume (FV) dynamical core with CAM 3.1 in an aqua-planet configuration sensitivity studies reveal that the initial wind speed and radius of maximum wind need to lie above a threshold to support the intensification of the analytic initial vortex at horizontal grid spacings of 0.5° and 0.25° (or 55 and 28 km in the equatorial regions). The thresholds lie between 15–20 m $s^{-1}$ with a radius of maximum wind of about 200–250 km. In addition, a convergence study with the grid spacings 1.0°, 0.5°, 0.25° and 0.125° (or 111, 55, 28 and 14 km) shows that the cyclone gets more intense and compact with increasing horizontal resolution. The 0.5°, 0.25° and 0.125° simulations exhibit many tropical cyclone-like characteristics such as a warm core, low-level wind maxima, a slanted eyewall-like vertical structure and a relatively calm eye. The 0.125° simulation even starts to resolve spiral rainbands and reaches maximum wind speeds of about 72–83 m $s^{-1}$ at low levels. These wind speeds are equivalent to a category-5

tropical cyclone on the Saffir-Simpson Hurricane Scale.

Chapter III explores the impact of the physical parameterization suite on the evolution of an idealized tropical cyclone using CAM versions 3.1 and 4. The FV dynamical core with 26 vertical levels in aqua-planet mode is again used to study the evolution of the idealized vortex at horizontal grid spacings of 1.0°, 0.5° and 0.25°. It is revealed in that CAM 4 produces stronger and larger tropical cyclones by day 10 at all resolutions, with a much earlier onset of intensification when compared to CAM 3.1. At the highest resolution CAM 4 also accounts for changes in the storm's vertical structure, such as an increased outward slope of the wind contours with height, when compared to CAM 3.1. An investigation concludes that the new dilute CAPE calculation in CAM 4 is largely responsible for the changes observed in the development, strength and structure of the tropical cyclone.

The impact of the initial-data, parameter and structural model uncertainty on the simulation of the idealized vortex in CAM is investigated in Chapter IV. A total of 78 ensemble simulations are performed at horizontal grid spacings of 1.0°, 0.5° and 0.25° using two versions of the model, CAM 4 and CAM 5. The ensemble members represent simulations with random small-amplitude perturbations of the initial conditions, small shifts in the longitudinal position of the initial vortex and runs with slightly altered model parameters. At all resolutions storms are produced with many tropical cyclone-like characteristics. The CAM 5 simulations exhibit more intense storms than CAM 4 by day 10 at the 0.5° and 0.25° grid spacings, while the CAM 4 storm at 1.0° is stronger. There are also distinct differences in the shapes and vertical profiles of the storms in the two variants of CAM.

The ensemble members show no significant distinction between the initial-data and parameter uncertainty simulations. At day 10 they produce ensemble root-mean-square deviations from an unperturbed control simulation on the order of 1–5 m $s^{-1}$ for the maximum low-level wind speed and 2–10 hPa for the minimum surface

pressure. However, there are large differences between the two CAM versions at identical horizontal resolutions. It suggests that the structural uncertainty due to the different CAM versions is more dominant than the initial-data and parameter uncertainties in this study. The uncertainty among the ensemble members is assessed and quantified.

Chapter V examines idealized tropical cyclones in CAM 5 with the spectral element (SE) dynamical core. CAM 5 SE successfully simulates tropical cyclones from the initial idealized vortex at the grid spacings of roughly 111 km, 55 km and 28 km near the equator. The simulated storms become increasingly intense and compact with increasing resolution. At 28 km resolution the simulated cyclone becomes extremely intense, with minimum surface pressures in the range of 845 to 865 hPa and absolute maximum wind speeds greater than 100 m $s^{-1}$. Additional simulations indicate that the behavior of the physics parameterizations with small time steps contributes to this intensity.

In Chapter VI a test case of intermediate complexity for atmospheric general circulation models (AGCM) is introduced. The test case consists of a simple moist physics suite paired with the evolution of the idealized vortex described in Chapter II. The simple-physics package includes the parameterizations of bulk surface fluxes for moisture, sensible heat and momentum, vertical diffusion in the boundary layer, and large-scale condensation. The impact of the choice of the four dynamical cores that are part of NCAR's hydrostatic Community Atmosphere Model CAM 5 on the evolution of the tropical cyclone is explored. The simulations show that despite the simplicity of the physics forcings the models develop the tropical cyclone at horizontal grid spacings of about 55 km and finer. The simple-physics simulations reveal essential differences in the storm's structure and strength due to the choice of the dynamical core. Similar differences are also seen in complex full-physics aqua-planet experiments with CAM 5 which serve as a motivator for this work. The results suggest that differences

in complex full-physics simulations can be, at least partly, replicated in simplified model setups. The simplified experiments might therefore provide easier access to an improved physical understanding of how the dynamical core and moist physical parameterizations interact. It is concluded that the simple-physics test case has the potential to close the gap between dry dynamical core assessments and full-physics aqua-planet experiments, and can shed light on the role of the dynamical core in the presence of moisture processes.

## 7.2 Accomplishments and highlights of the research project

### 7.2.1 Significance

High-resolution GCMs offer an attractive option for simulating the impact of climate change on tropical cyclone statistics, including storm track, intensity and tropical cyclogenesis. However, there are concerns of the significance of model design choices on the ability of GCMs to simulate tropical cyclones. A novel test of the evolution of an idealized vortex is used to understand the sensitivity to the GCM resolutions, numerics, model meshes and physical parameterizations. Such process studies offer a unique opportunity to interpret how these GCM design choices may impact full tropical cyclone climatologies in high-resolution GCMs.

### 7.2.2 Relevance and future potential

This project has introduced several methods for evaluating the impact of GCM design choices on the ability of the model to simulate tropical cyclones. The techniques, including the vortex initialization and simple-physics package, offer the descriptions needed in order to be easily implemented by other GCM modeling groups. Such an intercomparison of different GCMs would be beneficial to understanding how well multiple GCMs simulate tropical cyclones at adequate resolutions, and what may cause

differences amongst the models. Furthermore, the intercomparison has the potential to aid in the development of new numerical schemes and physical parameterizations that are better suited for the simulation of such extreme storms.

### 7.2.3 Collaboration

This research project has established a collaboration between the University of Michigan (UM), the Computation, Computers, Information and Mathematics Center at the Department of Energy (DOE) Sandia National Laboratories (SNL), the Scientific Computing Group at the DOE Lawrence Berkeley National Laboratory (LBNL) and the National Center for Atmospheric Research (NCAR). The science team supporting this research was composed of Christiane Jablonowski (UM), Richard Rood (UM), Mark Taylor (SNL), Michael Wehner (LBNL) and David Williamson (NCAR).

### 7.2.4 Interdisciplinary research

The techniques and ideas introduced in this research project were developed from the study of atmospheric science and computer science. This research combines the study of atmospheric modeling with new high performance computing techniques and parameterization development. Additional motivation for this research was drawn from the public policy realm, as understanding the potential societal and economic impacts of tropical cyclones and how these impacts will evolve over the coming decades as a result of climate change is extremely important. The success of this research is based on ability to aid in the development of the next-generation of GCMs in the area of policy-relevant science.

## 7.3 Future work

As high-resolution GCMs become increasingly instrumental in evaluations of tropical cyclones in current and future climate conditions, many questions remain. Future

work will include continued assessment of the ability for current and next-generation GCMs to simulate tropical cyclones. This work is a continuation of the doctoral research presented in this thesis that utilizes an idealized vortex initialization technique for GCMs. In particular, this research will investigate how advancements in numerical schemes, model grids, variable resolution techniques and future approaches to non-hydrostatic modeling influence the simulation of tropical cyclones within CAM. This includes continued use of the next-generation SE dynamical core in CAM. Moreover, the impact of advancements of mesh refinement techniques in GCMs on the simulation of tropical cyclones will be evaluated.

In addition, future research will assess the impact of advancements in physical parameterizations on extreme events. As the scales of GCMs become finer it is important that sub-grid scale parameterizations, including cloud microphysics, cloud macrophysics, turbulence, and convection, be tested to ensure they perform reliably during the simulation of extreme events, including tropical cyclones. Furthermore, it is expected that such a research direction can provide significant insight into the development of new state-of-the-art GCM physical parameterizations. Such parameterizations would be developed with the intent to improve the simulation of extreme weather events, a crucial aspect that is largely missing from GCM and physical parameterization development.

Additional research will investigate the impact of climate change on extreme weather events using NCARs CAM 5 at high resolutions. The initial set-up of these simulations is already underway in collaboration with Drs. Michael Wehner and William Collins at LBNL. The experiments will be configured in a manner similar to the Atmospheric Model Intercomparison Project (AMIP) using prescribed sea surface temperatures (SST) and radiative gases (*Gates*, 1992; *Gates et al.*, 1999). The goal is to gain an understanding of how extreme events, such as tropical cyclones, will be modified over the coming decades and century as a result of climate change. CAM 5

will be set up to run with the default FV dynamical core at a horizontal resolution of 0.25°, or roughly 28 km near the equator.

The research will evaluate the effect of climate change on tropical cyclones. The setup of the climate change experiments are as detailed by the U.S. Climate Variability and Predictability Research Program (CLIVAR) Hurricane Working Group, which consists of at least twelve modeling groups from around the world. The research focuses on both climatological and inter-annual variability as it pertains to tropical cyclones. This includes doubled carbon dioxide and increased SST experiments. A tropical cyclone tracking algorithm will be utilized to understand the impact of climate change on tropical cyclone statistics, including tracks, intensity and tropical cyclogenesis. In addition, the simulations will be used to understand how realistic individual simulated tropical cyclones are, and how climate change affects individual characteristics such as size, stages of development and precipitation rates. Such characteristics are often omitted from similar studies because of resolution limitations and this research will offer a first look within CAM 5. Moreover, the research will investigate the impact of climate change on other extreme weather events. The potential to use these simulations for other events, their causes and their societal impacts, are endless. The proposed phenomena to investigate include floods, droughts, tornadoes, mid-latitude storms and atmospheric rivers.

# APPENDICES

# APPENDIX A

# CAM Vertical Coordinate

CAM 5 uses the orography-following hybrid $\sigma$-pressure coordinates as described in *Simmons and Burridge* (1981). The coordinate is a combination of a pure pressure coordination and a $\sigma$-coordinate. The pressure $p$ at a vertical level $\eta$ is given by

$$p(\lambda, \varphi, \eta, t) = a(\eta)p_{00} + b(\eta)p_s(\lambda, \varphi, t). \tag{A.1}$$

Here $\lambda$ and $\varphi$ represent the longitude and latitude, respectively and $t$ is time. The coefficients $a(\eta)$ and $b(\eta)$ are height-dependent and $p_{00}$ is the reference pressure and is set to $10^5$ Pa. For discrete representation the $L$ full model levels are bounded by $L + 1$ interface levels. The interface levels are specified by the half indices $i + \frac{1}{2}$ and the pressure at each interface is given by

$$p_{i+\frac{1}{2}} = a_{i+\frac{1}{2}}p_{00} + b_{i+\frac{1}{2}}p_s, \tag{A.2}$$

where $i = 0, 1, 2, ...L$. Table A.1 provides the hybrid coefficients for the $L$ =30 levels used in CAM 5 at each model level interface. The full model coefficients can be calculated from the linear average of the coefficients at the model interface below and above.

Table A.1: Vertical hybrid coefficients at level interfaces for the CAM 5 30-level setup. The coefficient $a_{i+\frac{1}{2}}$ represents the pure pressure component and $b_{i+\frac{1}{2}}$ denotes the $\sigma$-pressure component, with the subscript $i+\frac{1}{2}$ defining the model interface between two full model levels.

| $i$ | $a_{i+\frac{1}{2}}$ | $b_{i+\frac{1}{2}}$ |
|---|---|---|
| 0 | 0.00225523952394724 | 0. |
| 1 | 0.00503169186413288 | 0. |
| 2 | 0.0101579474285245 | 0. |
| 3 | 0.0185553170740604 | 0. |
| 4 | 0.0306691229343414 | 0. |
| 5 | 0.0458674766123295 | 0. |
| 6 | 0.0633234828710556 | 0. |
| 7 | 0.0807014182209969 | 0. |
| 8 | 0.0949410423636436 | 0. |
| 9 | 0.11169321089983 | 0. |
| 10 | 0.131401270627975 | 0. |
| 11 | 0.154586806893349 | 0. |
| 12 | 0.181863352656364 | 0. |
| 13 | 0.17459799349308 | 0.0393548272550106 |
| 14 | 0.166050657629967 | 0.0856537595391273 |
| 15 | 0.155995160341263 | 0.140122056007385 |
| 16 | 0.14416541159153 | 0.204201176762581 |
| 17 | 0.130248308181763 | 0.279586911201477 |
| 18 | 0.113875567913055 | 0.368274360895157 |
| 19 | 0.0946138575673103 | 0.47261056303978 |
| 20 | 0.0753444507718086 | 0.576988518238068 |
| 21 | 0.0576589405536652 | 0.672786951065063 |
| 22 | 0.0427346378564835 | 0.753628432750702 |
| 23 | 0.0316426791250706 | 0.813710987567902 |
| 24 | 0.0252212174236774 | 0.848494648933411 |
| 25 | 0.0191967375576496 | 0.881127893924713 |
| 26 | 0.0136180268600583 | 0.911346435546875 |
| 27 | 0.00853108894079924 | 0.938901245594025 |
| 28 | 0.00397881818935275 | 0.963559806346893 |
| 29 | 0. | 0.985112190246582 |
| 30 | 0. | 1. |

# APPENDIX B

# Partially implicit implementation of the surface fluxes

The surface fluxes are implemented with a partially implicit time stepping scheme to enhance the numerical stability. Here we use the sensible heat flux of temperature as an example. We start with the time tendency for temperature

$$\frac{\partial T_a}{\partial t} = \frac{C_H|\vec{v}_a|(T_s - T_a)}{z_a}. \tag{B.1}$$

Next, the partial derivative of $T_a$ with respect to $t$ is written as a backward Euler discretization and the right-hand-side is represented in a partially implicit manner.

$$\frac{T_a^{n+1} - T_a^n}{\triangle t} = \frac{C_H|\vec{v}_a^n|(T_s - T_a^{n+1})}{z_a}. \tag{B.2}$$

The superscripts $n$ and $n+1$ represent the current time step (after the update from the large-scale condensation scheme) and the future time step, respectively. Note, that on the right-hand-side of the equation the only variable taken implicitly is $T_a$. $|\vec{v}_a^n|$ is evaluated at the current time step and $C_H$ is constant. The equation can now

be solved for $T_a^{n+1}$

$$T_a^{n+1} = \frac{T_a^n + C_H|\vec{v}_a^n|T_s\frac{\triangle t}{z_a}}{1 + C_H|\vec{v}_a^n|\frac{\triangle t}{z_a}}. \tag{B.3}$$

Similar equations for $u_a$, $v_a$ and $q_a$ can be calculated

$$u_a^{n+1} = \frac{u_a^n}{1 + C_d^n|\vec{v}_a^n|\frac{\triangle t}{z_a}} \tag{B.4}$$

$$v_a^{n+1} = \frac{v_a^n}{1 + C_d^n|\vec{v}_a^n|\frac{\triangle t}{z_a}} \tag{B.5}$$

$$q_a^{n+1} = \frac{q_a^n + C_E|\vec{v}_a^n|q_{sat,s}^n\frac{\triangle t}{z_a}}{1 + C_E|\vec{v}_a^n|\frac{\triangle t}{z_a}}, \tag{B.6}$$

with the time-level dependent coefficient $C_d^n$. Notice that the second term in the numerator of Eq. (B.3) is absent in the case of the zonal and merdional wind. This is because the wind is set to zero at the surface.

# APPENDIX C

# Partially implicit implementation of the boundary layer diffusion

## C.1 Zonal velocity

The boundary layer scheme is implemented as follows. Eq. (6.15) is written as

$$\frac{\partial u}{\partial t} = -\frac{1}{\rho}\frac{\partial F_u}{\partial z}, \tag{C.1}$$

with $F_u = \rho\ \overline{w'u'}$. The formulations for the meridional velocity, temperature and specific humidity equations are analogous. Using the hydrostatic equation the vertical derivative is discretized as

$$-\frac{1}{\rho}\frac{\partial F_u}{\partial z} = g\frac{\partial F_u}{\partial p} = g\frac{F_{u,+} - F_{u,-}}{p_+ - p_-}, \tag{C.2}$$

where the subscripts + and − denote the values at the lower and upper model interfaces, respectively. All equations and vertical discretization described in this study assume a vertical *Lorenz* (1960) staggering of the variables, where $u$, $v$, $T$ and $p$ are co-located at a full model level. In addition, we assume that $p$ can also be evaluated

at the model interfaces $p_+$ and $p_-$. Use of other vertical staggering, such as *Charney and Phillips* (1953) staggering, will require some reformulation of the following equations.

We now define the subscript $k = 1, 2, 3, ..., L$ that denotes the full model level, with $L$ being the total number of full model levels. Here, the index $k$ increases from the model top towards the surface. Then the value of $F_{u,-}$ at the upper interface of the model level $k$ can be calculated using Eq. (6.40)

$$F_{u,-} = \rho \, \overline{w'u'} = -\rho_- K_{m,-} \frac{\partial u}{\partial z}. \tag{C.3}$$

Using the hydrostatic approximation the equation becomes

$$F_{u,-} = g(\rho_-)^2 K_{m,-} \frac{\partial u}{\partial p}. \tag{C.4}$$

The equation is then discretized in the partially implicit form

$$F_{u,-} = g(\rho_-^n)^2 K_{m,-}^n \frac{u_k^{n+1} - u_{k-1}^{n+1}}{p_k^n - p_{k-1}^n}. \tag{C.5}$$

Again, the superscripts $n$ and $n+1$ represent the current time step after the implementation of the surface-fluxes and the future time step, respectively. Note, it is assumed that the pressure does not change in time within the physics parameterizations (typical for GCMs). The upper interface density $\rho_-$ is calculated with the help of the ideal gas law

$$\rho_-^n = \frac{2 \, p_-^n}{R_d \left( T_{k-1}^n + T_k^n \right)} \tag{C.6}$$

where the temperature at the interface is approximated via a linear average. The value for $F_{u,+}$ at the lower interface can be evaluated in a similar way

$$F_{u,+} = g(\rho_+^n)^2 K_{m,+}^n \frac{u_{k+1}^{n+1} - u_k^{n+1}}{p_{k+1}^n - p_k^n}, \tag{C.7}$$

and density $\rho_+$

$$\rho_+^n = \frac{2\, p_+^n}{R_d \left(T_k^n + T_{k+1}^n\right)}. \tag{C.8}$$

The surface fluxes $F_{u,L+}$ are set to zero.

As shown in *Boville and Bretherton* (2003) and *Neale et al.* (2010b) Eqs. (C.2), (C.5) and (C.7) represent a tridiagonal system of the form

$$-A_k^n u_{k+1}^{n+1} + B_k^n u_k^{n+1} - C_k^n u_{k-1}^{n+1} = u_k^n. \tag{C.9}$$

Here, $u_k^n$ represents the variable that has already been updated with the surface flux (at the lowermost model level). The super-diagonal $A_k^n$, diagonal $B_k^n$ and sub-diagonal $C_k^n$ elements (all at time level $n$) are

$$A_k^n = g^2(\rho_+^n)^2 K_{m,+}^n \frac{\triangle t}{(p_{k+1}^n - p_k^n)} \frac{1}{(p_+^n - p_-^n)} \tag{C.10}$$

$$B_k^n = 1 + A_k^n + C_k^n \tag{C.11}$$

$$C_k^n = g^2(\rho_-^n)^2 K_{m,-}^n \frac{\triangle t}{(p_k^n - p_{k-1}^n)} \frac{1}{(p_+^n - p_-^n)}. \tag{C.12}$$

We define the boundary conditions to be

$$A_L^n = 0. \tag{C.13}$$

The boundary condition is zero because the flux from the surface has already been accounted for in the surface flux parameterization. In addition, at the model top, index $k = 1$,

$$C_1^n = 0. \tag{C.14}$$

This ensures that there are no fluxes above the model top.

The solution to Eq. (C.9) is of the form

$$u_k^{n+1} = E_k^n u_{k-1}^{n+1} + F_k^n. \tag{C.15}$$

We now substitute the solution (Eq. (C.15)) into Eq. (C.9)

$$u_k^{n+1} = \frac{C_k^n}{B_k^n - A_k^n E_{k+1}^n} u_{k-1}^{n+1} + \frac{u_k^n + A_k^n F_{k+1}^n}{B_k^n - A_k^n E_{k+1}^n}. \tag{C.16}$$

Therefore $E_k^n$ and $F_k^n$ are found to be

$$E_k^n = \frac{C_k^n}{B_k^n - A_k^n E_{k+1}} \quad \text{for } L \geq k > 1, \tag{C.17}$$

$$F_k^n = \frac{u_k^n + A_k^n F_{k+1}^n}{B_k - A_k^n E_{k+1}^n} \quad \text{for } L \geq k > 1. \tag{C.18}$$

From the boundary conditions

$$E_{L+1}^n = F_{L+1}^n = A_L^n = 0. \tag{C.19}$$

Again the lower boundary conditions are zero since the surface flux is computed in a seperate parameterization. The boundary condition at the top of the model Eq. (C.14) implies the following condition

$$E_1^n = 0. \tag{C.20}$$

This boundary condition at the top of the model is the equivalent to setting the fluxes to zero above the model top. The terms $E_k^n$ and $F_k^n$ can be computed upwards from $k = L$. The final step is to solve Eq. (C.15) downward from the top of the model $k = 1$ to $L$.

## C.2 Meridional velocity

The formulations above, including the boundary conditions, are analogous for the meridional velocity except Eq. (C.15) becomes

$$v_k^{n+1} = E_k^n v_{k-1}^{n+1} + F_k^n. \tag{C.21}$$

The change in formulation requires a change in the calculation of $F_k^n$ for the meridional velocity. Therefore Eq. (C.18) becomes

$$F_k^n = \frac{v_k^n + A_k^n F_{k+1}^n}{B_k - A_k^n E_{k+1}^n} \quad \text{for } L \geq k > 1. \tag{C.22}$$

Except for these two changes the formulation of the boundary layer turbulence for the meridional velocity is identical to that of the zonal velocity explained in detail above.

## C.3 Potential temperature

The implicit implementation of the boundary layer for potential temperature requires more reformulation. Mainly, the calculation of $A_k^n$, $B_k^n$ and $C_k^n$ are all altered as

$$A_k^n = g^2(\rho_+^n)^2 K_{E,+}^n \frac{\triangle t}{(p_{k+1}^n - p_k^n)} \frac{1}{(p_+^n - p_-^n)} \tag{C.23}$$

$$B_k^n = 1 + A_k^n + C_k^n \tag{C.24}$$

$$C_k^n = g^2(\rho_-^n)^2 K_{E,-}^n \frac{\triangle t}{(p_k^n - p_{k-1}^n)} \frac{1}{(p_+^n - p_-^n)}. \tag{C.25}$$

Therefore, for potential temperature $E_k^n$ and $F_k^n$ become

$$E_k^n = \frac{C_k^n}{B_k^n - A_k^n E_{k+1}} \quad \text{for } L \geq k > 1 \tag{C.26}$$

$$F_k^n = \frac{\Theta_k^n + A_k^n F_{k+1}^n}{B_k - A_k^n E_{k+1}^n} \quad \text{for } L \geq k > 1. \tag{C.27}$$

Again, this results in a reformulation of Eq. (C.15) for temperature

$$\Theta_k^{n+1} = E_k^n \Theta_{k-1}^{n+1} + F_k^n, \tag{C.28}$$

which leads to the temperature update

$$T_k^{n+1} = \Theta_k^{n+1} \left( \frac{p_k}{p_{00}} \right)^{R_d/c_p}. \tag{C.29}$$

Note, that the boundary conditions stated in Eq. (C.13) and Eq. (C.14) remain unchanged.

## C.4 Specific humidity

The final component of the boundary layer implementation is the specific humidity $q$ and the formulation follows closely that of the potential temperature. The calculations of $A_k^n$, $B_k^n$, $C_k^n$ and $E_k^n$ are the same as they are for the potential temperature (Eq. (C.23) - (C.26)). However, the formulation of $F_k^n$ (Eq. (C.27)) becomes

$$F_k^n = \frac{q_k^n + A_k^n F_{k+1}^n}{B_k - A_k^n E_{k+1}^n} \quad \text{for } L \geq k > 1. \tag{C.30}$$

Finally, the solution of the tridiagonal system for the specific humidity is

$$q_k^{n+1} = E_k^n q_{k-1}^{n+1} + F_k^n. \tag{C.31}$$

Again the boundary conditions remain the same, as is the case for potential temperature and the zonal and meridional velocities.

# BIBLIOGRAPHY

# BIBLIOGRAPHY


Abarca, S. F., and K. L. Corbosiero (2011), Secondary eyewall formation in WRF simulations of hurricanes Rita and Katrina (2005), *Geophys. Res. Lett.*, *38*, L07802, doi:10.1029/2011GL047015.

Anthes, R. A. (1982), *Tropical cyclones: their evolution, structure and effects*, Amer. Meteor. Soc., 208 pp.

Anthes, R. A., S. L. Rosenthal, and J. W. Trout (1971), Preliminary results from an asymmetric model of the tropical cyclone, *Mon. Wea. Rev.*, *99*, 744–758.

Arakawa, A., and V. R. Lamb (1977), Computational design of the basic dynamical process of the UCLA general circulation model, in *Methods in Computational Physics*, edited by J. Chang, pp. 173–265, Academic Press.

Arakawa, A., J.-H. Jung, and C.-M. Wu (2011), Toward unification of the multiscale modeling of the atmosphere, *Atmos. Chem. Phys.*, *11*, 3731–3742, doi:10.5194/acp-11-3731-2011.

Atlas, R., et al. (2005), Hurricane forecasting with the high-resolution NASA finite volume general circulation model, *Geophys. Res. Lett.*, *32*, L03807, doi: 10.1029/2004GL021513.

Baer, F., H. Wang, J. J. Tribbia, and A. Fournier (2006), Climate modeling with spectral elements, *Mon. Wea. Rev.*, *134*, 3610–3624.

Bell, M. M., and M. T. Montgomery (2008), Observed structure, evolution, and potential intensity of category 5 Hurricane Isabel (2003) from 12 to 14 September, *Mon. Wea. Rev.*, *136*, 2023–2046, doi:10.1175/2007MWR1858.1.

Bender, M. A., T. R. Knutson, R. E. Tuleya, J. J. Sirutis, G. A. Vecchi, S. T. Garner, and I. M. Held (2010), Modeled impact of anthropogenic warming on the frequency of intense Atlantic hurricanes, *Science*, *327*, 454–458, doi:10.1126/science.1180568.

Bengtsson, L., H. Bottger, and M. Kanamitsu (1982), Simulation of hurricane-type vortices in a general circulation model, *Tellus*, *34*, 440–457.

Bengtsson, L., K. I. Hodges, M. Esch, N. Keenlyside, L. Kornblueh, J. Luo, and T. Yamagata (2007), How may tropical cyclones change in a warmer climate?, *Tellus Series A*, *59*, 539–561, doi:10.1111/j.1600-0870.2007.00251.x.

Betts, A. K., and M. J. Miller (1986), A new convective adjustment scheme, Part II: Single column tests using GATE wave, BOMEX, ATEX and arctic air-mass data sets, *Quart. J. Roy. Meteor. Soc.*, *112*, 693–709, doi:10.1002/qj.49711247308.

Black, P. G., E. A. D'Asaro, W. M. Drennan, J. R. French, P. P. Niiler, T. B. Sanford, E. J. Terrill, E. J. Walsh, and J. A. Zhang (2007), Air sea exchange in hurricanes: Synthesis of observations from the coupled boundary layer air sea transfer experiment, *Bull. Am. Meteor. Soc.*, *88*, 357–374, doi:10.1175/BAMS-88-3-357.

Bode, L., and R. K. Smith (1975), A parameterization of the boundary layer of a tropical cyclone, *Bound.-Layer Meteor.*, *8*, 3–19, doi:10.1007/BF02579390.

Boer, G. J., and B. Denis (1997), Numerical covergence of the dynamics of a GCM, *Climate Dyn.*, *13*, 359–374.

Boville, B. A. (1991), Sensitivity of simulated climate to model resolution, *J. Climate*, *4*, 469–485.

Boville, B. A., and C. S. Bretherton (2003), Heating and kinetic energy dissipation in the NCAR Community Atmosphere Model, *J. Climate*, *16*, 3877–3887, doi:10.1175/1520-0442(2003)016<3877:HAKEDI>2.0.CO;2.

Bretherton, C. S., and S. Park (2009), A new moist turbulence parameterization in the Community Atmosphere Model, *J. Climate*, *22*, 3422–3448, doi:10.1175/2008JCLI2556.1.

Broccoli, A. J., and S. Manabe (1990), Can existing climate models be used to study anthropogenic changes in tropical cyclone climate?, *Geophys. Res. Lett.*, *17*, 1917–1920, doi:10.1029/GL017i011p01917.

Bryan, G. H., and R. Rotunno (2009a), The influence of near-surface, high-entropy air in hurricane eyes on maximum hurricane intensity, *J. Atmos. Sci.*, *66*, 148–158, doi:10.1175/2008JAS2707.1.

Bryan, G. H., and R. Rotunno (2009b), The maximum intensity of tropical cyclones in axisymmetric numerical model simulations, *Mon. Wea. Rev.*, *137*, 1770–1789, doi:10.1175/2008MWR2709.1.

Charney, J. G., and N. A. Phillips (1953), Numerical integration of the quasi-geostrophic equations for barotropic and simple baroclinic flows, *J. Atmos. Sci.*, *10*, 71–99, doi:10.1175/1520-0469(1953)010<0071:NIOTQG>2.0.CO;2.

Chen, J.-H., and S.-J. Lin (2011), The remarkable predictability of inter-annual variability of Atlantic hurricanes during the past decade, *Geophys. Res. Lett.*, *38*, L11804, doi:10.1029/2011GL047629.

Chen, Q., M. Gunzburger, and T. Ringler (2011), A scale-invariant formulation of the anticipated potential vorticity method, *Mon. Wea. Rev.*, *139*, 2614–2629, doi: 10.1175/MWR-D-10-05004.1.

Claussen, M., et al. (2002), Earth system models of intermediate complexity: closing the gap in the spectrum of climate system models, *Climate Dyn.*, *18*(7), 579–586.

Colella, P., and P. R. Woodward (1984), The Piecewise Parabolic Method (PPM) for gas-dynamical simulations, *J. Comput. Phys.*, *54*, 174–201, doi:10.1016/0021-9991(84)90143-8.

Collins, W. D., et al. (2004), Description of the NCAR Community Atmosphere Model (CAM 3.0), *NCAR Tech. Note NCAR/TN-464+STR*, National Center for Atmospheric Research, Boulder, Colorado, 226 pp.

Collins, W. D., et al. (2006), The formulation and atmospheric simulation of the Community Atmosphere Model: CAM3, *J. Climate*, *19*, 2144–2161.

Dennis, J., J. Edwards, K. J. Evans, O. N. Guba, P. H. Lauritzen, A. A. Mirin, A. St-Cyr, M. A. Taylor, and P. H. Worley (2011), CAM-SE: A scalable spectral element dynamical core for the Community Atmosphere Model, *Int. J. High Performance Computing Applications*, doi:10.1177/1094342011428142, published online on 11/14/2011.

Doblas-Reyes, F. J., A. Weisheimer, M. Déqué, N. Keenlyside, M. McVean, J. M. Murphy, P. Rogel, D. Smith, and T. N. Palmer (2009), Addressing model uncertainty in seasonal and annual dynamical ensemble forecasts, *Quart. J. Roy. Meteor. Soc.*, *135*, 1538–1559, doi:10.1002/qj.464.

Donner, L. J., et al. (2011), The dynamical core, physical parameterizations, and basic simulation characteristics of the atmospheric component AM3 of the GFDL global Coupled Model CM3, *J. Climate*, *24*, 34843519, doi:10.1175/2011JCLI3955.1.

Dudhia, J. (1993), A nonhydrostatic version of the Penn State NCAR Mesoscale Model: Validation tests and simulation of an Atlantic cyclone and cold front, *Mon. Wea. Rev.*, *121*, 1493–1513, doi:10.1175/1520-0493(1993)121<1493:ANVOTP>2.0.CO;2.

Emanuel, K. (2003), Tropical cyclones, *Ann. Rev. Earth Planet. Sci.*, *31*, 75–104, doi:10.1146/annurev.earth.31.100901.141259.

Emanuel, K. (2010), Tropical cyclone activity downscaled from NOAA-CIRES Reanalysis, 1908-1958, *J. Adv. Model. Earth Syst.*, *2*, 12 pp., doi: 10.3894/JAMES.2010.2.1.

Emanuel, K., K. Oouchi, M. Satoh, H. Tomita, and Y. Yamada (2010), Comparison of explicitly simulated and downscaled tropical cyclone activity in a high-resolution global climate model, *J. Adv. Model. Earth Syst.*, *2*, 9 pp., doi: 10.3894/JAMES.2010.2.9.

Emanuel, K. A. (1986), An air-sea interaction theory for tropical cyclones. part i: Steady-state maintenance, *J. Atmos. Sci.*, *43*, 585–605, doi:10.1175/1520-0469(1986)043<0585:AASITF>2.0.CO;2.

Emanuel, K. A. (1988), The maximum intensity of hurricanes, *J. Atmos. Sci.*, *45*(7), 1143–1155.

Emanuel, K. A. (1989), The finite-amplitude nature of tropical cyclogenesis, *J. Atmos. Sci.*, *46*, 3431–3456, doi:10.1175/1520-0469(1989)046<3431:TFANOT>2.0.CO;2.

Fournier, A., M. A. Taylor, and J. J. Tribbia (2004), The spectral element atmospheric model: High-resolution parallel computation and response to regional forcing, *Mon. Wea. Rev.*, *132*, 726–748.

Fox-Rabinovitz, M. S., G. L. Stenchikov, M. J. Suarez, and L. L. Takacs (1997), A finite-difference GCM dynamical core with a variable-resolution stretched grid, *Mon. Wea. Rev.*, *125*, 2943–2968.

Frierson, D. M. W., I. M. Held, and P. Zurita-Gotor (2006), A gray-radiation aqua-planet moist GCM. Part I: Static stability and Eddy scale, *J. Atmos. Sci.*, *63*, 2548–2566, doi:10.1175/JAS3753.1.

Fudeyasu, H., Y. Wang, M. Satoh, T. Nasuno, H. Miura, and W. Yanase (2008), Global cloud-system-resolving model NICAM successfully simulated the lifecycles of two real tropical cyclones, *Geophys. Res. Lett.*, *35*, L22808, doi: 10.1029/2008GL036003.

Fudeyasu, H., Y. Wang, M. Satoh, T. Nasuno, H. Miura, and W. Yanase (2010a), Multiscale interactions in the life cycle of a tropical cyclone simulated in a global cloud-system-resolving model. Part I: Large-scale and storm-scale evolutions, *Mon. Wea. Rev.*, *138*, 4285–4304, doi:10.1175/2010MWR3474.1.

Fudeyasu, H., Y. Wang, M. Satoh, T. Nasuno, H. Miura, and W. Yanase (2010b), Multiscale interactions in the life cycle of a tropical cyclone simulated in a global cloud-system-resolving model. Part II: System-scale and mesoscale processes, *Mon. Wea. Rev.*, *138*, 4305–4327, doi:10.1175/2010MWR3475.1.

Galewsky, J., L. M. Polvani, and R. K. Scott (2004), An initial-value problem to test numerical models of the shallow water equations, *Tellus*, *56A*, 429–440.

Garratt, J. R. (1992), *The Atmospheric Boundary Layer*, Cambridge University Press, 316 pp.

Gates, W. L. (1992), AMIP: The Atmospheric Model Intercomparison Project, *Bull. Amer. Meteor. Soc.*, *73*, 1962–1970.

Gates, W. L., et al. (1999), An overview of the results of the Atmospheric Model Intercomparison Project (AMIP I), *Bull. Amer. Meteor. Soc.*, *80*, 29–55.

Giraldo, F. X., and T. E. Rosmond (2004), A scalable Spectral Element Eulerian Atmospheric Model (SEE-AM) for NWP: Dynamical core tests, *Mon. Wea. Rev.*, *132*, 133–153, doi:10.1175/1520-0493(2004)132<0133:ASSEEA>2.0.CO;2.

Gualdi, S., E. Scoccimarro, and A. Navarra (2008), Changes in tropical cyclone activity due to global warming: Results from a high-resolution coupled General Circulation Model, *J. Climate*, *21*, 5204–5228, doi:10.1175/2008JCLI1921.1.

Hack, J. J. (1994), Parameterization of moist convection in the National Center for Atmospheric Research Community Climate Model (CCM2), *J. Geophys. Res.*, *99*, 5551–5568, doi:10.1029/93JD03478.

Hasse, L., and S. D. Smith (1997), Local sea surface wind, wind stress, and sensible and latent heat fluxes, *J. Climate*, *10*, 2711–2724, doi:10.1175/1520-0442(1997)010.

Held, I. M., and M. J. Suarez (1994), A proposal for the intercomparison of the dynamical cores of atmospheric general circulation models, *Bull. Amer. Meteor. Soc.*, *75*, 1825–1830, doi:10.1175/1520-0477(1994)075<1825:APFTIO>2.0.CO;2.

Held, I. M., and M. Zhao (2011), The response of tropical cyclone statistics to an increase in $CO_2$ with fixed sea surface temperatures, *J. Climate*, *24*, 5353–5364, doi:10.1175/JCLI-D-11-00050.1.

Hill, K. A., and G. M. Lackmann (2009a), Analysis of idealized tropical cyclone simulations using the Weather Research and Forecasting model: Sensitivity to turbulence parameterization and grid spacing, *Mon. Wea. Rev.*, *137*, 745–765, doi:10.1175/2008MWR2220.1.

Hill, K. A., and G. M. Lackmann (2009b), Influence of environmental humidity on tropical cyclone size, *Mon. Wea. Rev.*, *137*, 3294–3315.

Holland, G. J. (1980), An analytic model of the wind and pressure profiles in hurricanes, *Mon. Wea. Rev.*, *108*, 1212–1218, doi:10.1175/1520-0493(1980)108<1212:AAMOTW>2.0.CO;2.

Holland, G. J. (1983), Tropical cyclone motion: Environmental interaction plus a beta effect, *J. Atmos. Sci.*, *40*, 328–342, doi:10.1175/1520-0469(1983)040<0328:TCMEIP>2.0.CO;2.

Holton, J. R. (2004), *An Introduction to Dynamic Meteorology*, fourth ed., Elsevier Acadamic Press, ISBN 0123540151, 535 pp.

Holtslag, A. A. M., and B. A. Boville (1993), Local versus nonlocal boundary-layer diffusion in a global climate model, *J. Climate*, *6*, 1825–1842, doi:10.1175/1520-0442(1993)006<1825:LVNBLD>2.0.CO;2.

Hurrell, J., G. A. Meehl, D. Bader, T. L. Delworth, B. Kirtman, and B. Wielicki (2009), A unified modeling approach to climate system prediction, *Bull. Amer. Meteor. Soc.*, *90*, 1819–1832.

Jablonowski, C., and D. L. Williamson (2006a), A baroclinic instabilitiy test case for atmospheric model dynamical cores, *Quart. J. Roy. Meteor. Soc.*, *132*(621C), 2943–2975.

Jablonowski, C., and D. L. Williamson (2006b), A baroclinic wave test case for dynamical cores of General Circulation Models: Model intercomparisons, *NCAR Tech. Note NCAR/TN-469+STR*, National Center for Atmospheric Research, Boulder, Colorado, 89 pp.

Jablonowski, C., and D. L. Williamson (2011), The pros and cons of diffusion, filters and fixers in atmospheric general circulation models, in *Numerical Techniques for Global Atmospheric Models*, *Lecture Notes in Computational Science and Engineering*, vol. 80, edited by P. H. Lauritzen, C. Jablonowski, M. A. Taylor, and R. D. Nair, pp. 381–493, Springer.

Jablonowski, C., P. H. Lauritzen, R. D. Nair, and M. A. Taylor (2008), Idealized test cases for the dynamical cores of Atmospheric General Circulation Models: A proposal for the NCAR ASP 2008 summer colloquium, available online at http://www-personal.umich.edu/~cjablono/cv.html#Publication.

Jablonowski, C., R. C. Oehmke, and Q. F. Stout (2009), Block-structured adaptive meshes and reduced grids for atmospheric general circulation models, *Phil. Trans. R. Soc. A*, *367*, 4497–4522.

Jordan, C. L. (1958), Mean soundings for the west indies area, *J. Atmos. Sci.*, *15*, 91–97, doi:10.1175/1520-0469(1958)015.

Kaplan, J., and M. Demaria (2003), Large-scale characteristics of rapidly intensifying tropical cyclones in the North Atlantic basin, *Wea. Forecasting*, *18*, 1093–1108, doi:10.1175/1520-0434(2003)018<1093:LCORIT>2.0.CO;2.

Knutson, T. R., and R. E. Tuleya (2004), Impact of $CO_2$-induced warming on simulated hurricane intensity and precipitation: Sensitivity to the choice of climate model and convective parameterization, *J. Climate*, *17*, 3477–3495, doi: 10.1175/1520-0442(2004)017.

Knutson, T. R., R. E. Tuleya, W. Shen, and I. Ginis (2001), Impact of $CO_2$-induced warming on hurricane intensities as simulated in a hurricane model with ocean coupling, *J. Climate*, *14*, 2458–2468, doi:10.1175/1520-0442(2001)014.

Knutson, T. R., J. J. Sirutis, S. T. Garner, G. A. Vecchi, and I. M. Held (2008), Simulated reduction in Atlantic hurricane frequency under twenty-first-century warming conditions, *Nature Geosci.*, *1*, 359–364, doi:10.1038/ngeo202.

Kuo, H. L. (1965), On formation and intensification of tropical cyclones through latent heat release by cumulus convection., *J. Atmos. Sci.*, *22*, 40–63.

Kurihara, Y., and R. E. Tuleya (1974), Structure of a tropical cyclone developed in a three-dimensional numerical simulation model., *J. Atmos. Sci.*, *31*, 893–919.

Kurihara, Y., R. E. Tuleya, and M. A. Bender (1998), The GFDL hurricane prediction system and its performance in the 1995 hurricane season, *Mon. Wea. Rev.*, *126*, 1306–1322, doi:10.1175/1520-0493(1998)126<1306:TGHPSA>2.0.CO;2.

Kwon, I.-H., and H.-B. Cheong (2010), Tropical cyclone initialization with a spherical high-order filter and an idealized three-dimensional bogus vortex, *Mon. Wea. Rev.*, *138*, 1344–1367, doi:10.1175/2009MWR2943.1.

Lauritzen, P. H., C. Jablonowski, M. A. Taylor, and R. D. Nair (2010), Rotated versions of the Jablonowski steady-state and baroclinic wave test cases: A dynamical core intercomparison, *J. Adv. Model. Earth Syst.*, *2*, 34 pp., doi: 10.3894/JAMES.2010.2.15.

Leslie, L. M., and G. J. Holland (1995), On the bogussing of tropical cyclones in numerical models: A comparison of vortex profiles, *Meteor. Atmos. Phys.*, *56*, 101–110, doi:10.1007/BF01022523.

Li, F., W. D. Collins, M. F. Wehner, D. L. Williamson, J. G. Olson, and C. Algieri (2011), Impact of horizontal resolution on simulation of precipitation extremes in an aqua-planet version of Community Atmospheric Model (CAM3), *Tellus Series A*, *63*, 884–892, doi:10.1111/j.1600-0870.2011.00544.x.

Lin, S.-J. (2004), A "vertically Lagrangian" finite-volume dynamical core for global models, *Mon. Wea. Rev.*, *132*, 2293–2307.

Lin, S.-J., and R. B. Rood (1996), Multidimensional flux-form semi-Lagrangian transport scheme, *Mon. Wea. Rev.*, *124*, 2046–2070.

Lin, S.-J., and R. B. Rood (1997), An explicit flux-form semi-Lagrangian shallow water model on the sphere, *Quart. J. Roy. Meteor. Soc.*, *123*, 2477–2498.

Lorant, V., and J. Royer (2001), Sensitivity of equatorial convection to horizontal resolution in aquaplanet simulations with a variable-resolution GCM, *Mon. Wea. Rev.*, *129*, 2730–2745, doi:10.1175/1520-0493(2001)129<2730:SOECTH>2.0.CO;2.

Lorenz, E. N. (1960), Energy and numerical weather prediction, *Tellus*, *12*, 364–373.

Machenhauer, B. (1979), The spectral method, in *Numerical methods used in atmospheric models*, vol. 2, edited by A. Kasahara, pp. 121–275, GARP Publications Series No 17, WMO and ICSU, Geneva.

Madala, R. V., and S. A. Piacsek (1975), Numerical simulation of asymmetric hurricanes on a $\beta$-plane with vertical shear, *Tellus*, *27*, 453–468.

Manabe, S., J. Leith Holloway, Jr., and H. M. Stone (1970), Tropical circulation in a time-integration of a global model of the atmosphere, *J. Atmos. Sci.*, *27*, 580–613, doi:10.1175/1520-0469(1970)027.

Mathur, M. B. (1974), A multi-grid primitive equation model to simulate the development of an asymmetric hurricane (Isebell, 1964), *J. Atmos. Sci.*, *31*, 371–393.

Meehl, G. A., et al. (2007), Global climate projections, in *Climate Change 2007: The Physical Science Basis. Contribution of Working Group I to the Fourth Assessment Report of the Intergovernmental Panel on Climate Change*, edited by S. Solomon, D. Qin, M. Manning, Z. Chen, M. M. amd K. B. Averyt, M. Tignor, and H. L. Miller, pp. 747–845, Cambridge University Press, Cambridge, United Kingdom and New York, NY, USA.

Mishra, S. K., M. A. Taylor, R. D. Nair, P. H. Lauritzen, H. M. Tufo, and J. J. Tribbia (2011), Evaluation of the HOMME dynamical core in the aquaplanet configuration of NCAR CAM4: Rainfall, *J. Climate*, *24*, 4037–4055.

Miura, H., M. Satoh, H. Tomita, A. Noda, T. Nasuno, S. Iga, M. Satoh, and T. Matsuno (2007), A short-duration global cloud-resolving simulation with a realistic land and sea distribution, *Geophys. Res. Lett.*, *34*, L02804.

Molteni, F. (2002), Atmospheric simulations using a GCM with simplified physical parametrizations. I: model climatology and variability in multi-decadal experiments, *Climate Dyn.*, *20*, 175–191, doi:10.1007/s00382-002-0268-2.

Monaco, A. V., and R. T. Williams (1975), An atmospheric global prediction model using a modified Arakawa differencing scheme, *Tech. rep.*, Dept. of Meteorology, Naval Postgraduate School, Monterey, CA, NPS-51WU75041, 86pp.

Montgomery, M. T., M. M. Bell, S. D. Aberson, and M. L. Black (2006), Hurricane Isabel (2003): New insights into the physics of intense storms. Part I: Mean vortex structure and maximum intensity estimates, *Bull. Amer. Meteor. Soc.*, *87*, 1335–1347, doi:10.1175/BAMS-87-10-1335.

Murakami, H., and M. Sugi (2010), Effect of model resolution on tropical cyclone climate projections, *SOLA*, *6*, 73–76, doi:10.2151/sola.2010-019.

Murphy, J. M., D. M. H. Sexton, D. N. Barnett, G. S. Jones, M. J. Webb, M. Collins, and D. A. Stainforth (2004), Quantification of modelling uncertainties in a large ensemble of climate change simulations, *Nature*, *430*, 768–772, doi:10.1038/nature02771.

Nair, R. D., and C. Jablonowski (2008), Moving vortices on the sphere: A test case for horizontal advection problems, *Mon. Wea. Rev.*, *136*, 699–711.

Neale, R. B., and B. J. Hoskins (2000), A standard test for AGCMs including their physical parametrizations: I: the proposal, *Atmos. Sci. Letters*, *1*, 101–107, doi:10.1006/asle.2000.0019.

Neale, R. B., J. H. Richter, and M. Jochum (2008), The impact of convection on ENSO: From a delayed oscillator to a series of events, *J. Climate*, *21*, 5904–5924, doi:10.1175/2008JCLI2244.1.

Neale, R. B., et al. (2010a), Description of the NCAR Community Atmosphere Model (CAM 4.0), *NCAR Tech. Note NCAR/TN-485+STR*, National Center for Atmospheric Research, Boulder, Colorado, 206 pp.

Neale, R. B., et al. (2010b), Description of the NCAR Community Atmosphere Model (CAM 5.0), *NCAR Tech. Note NCAR/TN-486+STR*, National Center for Atmospheric Research, Boulder, Colorado, 282 pp.

Nolan, D. S. (2007), What is the trigger for tropical cyclogenesis?, *Aust. Meteorol. Mag.*, *56*, 241–266.

Nolan, D. S., and E. D. Rappin (2008), Increased sensitivity of tropical cyclogenesis to wind shear in higher SST environments, *Geophys. Res. Lett.*, *35*, L14805, doi: 10.1029/2008GL034147.

Nolan, D. S., M. T. Montgomery, and L. D. Grasso (2001), The wavenumber-one instability and trochoidal motion of hurricane-like vortices, *J. Atmos. Sci.*, *58*, 3243–3270, doi:10.1175/1520-0469(2001)058.

Nolan, D. S., E. D. Rappin, and K. A. Emanuel (2007), Tropical cyclogenesis sensitivity to environmental parameters in radiative-convective equilibrium, *Quart. J. Roy. Meteor. Soc.*, *133*(629), 2085–2107.

Nolan, D. S., J. A. Zhang, and D. P. Stern (2009), Evaluation of planetary boundary layer parameterizations in tropical cyclones by comparison of in situ observations and high-resolution simulations of Hurricane Isabel (2003). Part I: Initialization, maximum winds, and the outer-core boundary layer, *Mon. Wea. Rev.*, *137*, 3651–3674, doi:10.1175/2009MWR2785.1.

Oouchi, K., J. Yoshimura, H. Yoshimura, R. Mizuta, S. Kusunoki, and A. Noda (2006), Tropical cyclone climatology in a global-warming climate as simulated in a 20 km-mesh global atmospheric model: Frequency and wind intensity analyses, *J. Meteor. Soc. Japan*, *84*(2), 259–276.

Ooyama, K. (1969), Numerical simulation of the life cycle of tropical cyclones, *J. Atmos. Sci.*, *26*, 3–40, doi:10.1175/1520-0469(1969)026<0003:NSOTLC>2.0.CO;2.

Ooyama, K. (1982), Conceptual evolution of the theory and modeling of the tropical cyclone, *J. Meteor. Soc. Japan*, *60*, 369–379.

Palmer, T. N. (2000), Predicting uncertainty in forecasts of weather and climate, *Rep. Prog. Phys.*, *63*, 71–116, doi:10.1088/0034-4885/63/2/201.

Palmer, T. N. (2001), A nonlinear dynamical perspective on model error: A proposal for non-local stochastic-dynamic parametrization in weather and climate prediction models, *Quart. J. Roy. Meteor. Soc.*, *127*, 279–304, doi:10.1002/qj.49712757202.

Palmer, T. N., F. J. Doblas-Reyes, A. Weisheimer, and M. J. Rodwell (2008), Towards seamless prediction, *Bull. Amer. Meteor. Soc.*, *89*(4), 459–470.

Park, S., and C. S. Bretherton (2009), The University of Washington shallow convection and moist turbulence schemes and their impact on climate simulations with the Community Atmosphere Model, *J. Climate*, *22*, 3449–3469, doi: 10.1175/2008JCLI2557.1.

Persing, J., and M. T. Montgomery (2003), Hurricane superintensity, *J. Atmos. Sci.*, *60*, 2349–2371, doi:10.1175/1520-0469(2003)060<2349:HS>2.0.CO;2.

Phillips, N. A. (1957), A coordinate system having some special advantages for numerical forecasting, *J. Meteorol.*, *14*, 184–185.

Pielke, R., Jr., J. Gratz, C. Landsea, D. Collins, M. Saunders, and R. Musulin (2008), Normalized hurricane damage in the United States: 1900-2005, *Nat. Hazards Rev.*, *9*, 29–42.

Pielke, R. A., Jr., and C. W. Landsea (1998), Normalized hurricane damages in the United States: 1925-95, *Wea. Forecasting*, *13*, 621–631, doi:10.1175/1520-0434(1998)013<0621:NHDITU>2.0.CO;2.

Polvani, L. M., R. K. Scott, and S. J. Thomas (2004), Numerically converged solutions of the global primitive equations for testing the dynamical core of atmospheric GCMs, *Mon. Wea. Rev.*, *132*, 2539–2552, doi:10.1175/MWR2788.1.

Putman, W. M., and S.-J. Lin (2007), Finite-volume transport on various cubed-sphere grids, *J. Comput. Phys.*, *227*, 55–78.

Putman, W. M., and S.-J. Lin (2009), A finite-volume dynamical core on the cubed-sphere grid, in *Numerical Modeling of Space Plasma Flows: Astronum-2008*, vol. 406, pp. 268–276, Astronomical Society of the Pacific Conference Series.

Randall, D. A., K.-M. Xu, R. J. C. Somerville, and S. Iacobellis (1996), Single-column models and cloud ensemble models as links between observations and climate models, *J. Climate*, *9*, 1683–1697, doi:10.1175/1520-0442(1996)009<1683:SCMACE>2.0.CO;2.

Randall, D. A., et al. (2007), Climate models and their evaluation, in *Climate Change 2007: The Physical Science Basis. Contribution of Working Group I to the Fourth Assessment Report of the Intergovernmental Panel on Climate Change*, edited by S. Solomon, D. Qin, M. Manning, Z. Chen, M. Marquis, K. B. Averyt, M. Tignor, and H. L. Miller, pp. 589–662, Cambridge University Press, Cambridge, United Kingdom and New York, NY, USA.

Reed, K. A., and C. Jablonowski (2011a), An analytic vortex initialization technique for idealized tropical cyclone studies in AGCMs, *Mon. Wea. Rev.*, *139*, 689–710, doi:10.1175/2010MWR3488.1.

Reed, K. A., and C. Jablonowski (2011b), Impact of physical parameterizations on idealized tropical cyclones in the community atmosphere model, *Geophys. Res. Lett.*, *38*, L04805, doi:10.1029/2010GL046297.

Reed, K. A., and C. Jablonowski (2011c), Assessing the uncertainty of tropical cyclone simulations in NCAR's Community Atmosphere Model, *J. Adv. Model. Earth Syst.*, *3*, M08002, doi:10.1029/2011MS000076, 16 pp.

Richter, J. H., and P. J. Rasch (2008), Effects of convective momentum transport on the atmospheric circulation in the Community Atmosphere Model, version 3, *J. Climate*, *21*, 1487–1499, doi:10.1175/2007JCLI1789.1.

Ringler, T. D., D. Jacobsen, M. Gunzburger, L. Ju, M. Duda, and W. C. Skamarock (2011), Exploring a multi-resolution modeling approach within the shallow-water equations, *Mon. Wea. Rev.*, *139*, 3348–3368, doi:10.1175/MWR-D-10-05049.1.

Rogers, R., M. L. Black, S. S. Chen, and R. A. Black (2007), An evaluation of microphysics fields from mesoscale model simulations of tropical cyclones. Part I: Comparisons with observations, *J. Atmos. Sci.*, *64*, 1811–1834.

Rosenthal, S. L. (1969), Numerical experiments with a multilevel primitive equation model designed to simulate the development of tropical cyclones, experiment 1, *Tech. Rep. Technical Memorandum No. 82*, National Hurricane Research Laboratory, 36 pp.

Rosenthal, S. L. (1978), Numerical Simulation of Tropical Cyclone Development with Latent Heat Release by the Resolvable Scales I: Model Description and Preliminary Results., *Journal of Atmospheric Sciences*, *35*, 258–271, doi:10.1175/1520-0469(1978)035<0258:NSOTCD>2.0.CO;2.

Rotunno, R., and K. A. Emanuel (1987), An air-sea interaction theory for tropical cyclones. Part II: Evolutionary study using a nonhydrostatic axisymmetric numerical model, *J. Atmos. Sci.*, *44*, 542–561, doi:10.1175/1520-0469(1987)044<0542:AAITFT>2.0.CO;2.

Sadourny, R. (1972), Conservative finite-difference approximations of the primitive equations on quasi-uniform spherical grids, *Mon. Wea. Rev.*, *100*, 136–144, doi:10.1175/1520-0493(1972)100<0136:CFAOTP>2.3.CO;2.

Sadourny, R., A. Arakawa, and Y. Mintz (1968), Integration of the nondivergent barotropic vorticity equation with an icosahedral-hexagonal grid for the SPHERE1, *Mon. Wea. Rev.*, *96*, 351–356, doi:10.1175/1520-0493(1968)096<0351:IOTNBV>2.0.CO;2.

Satoh, M., H. Tomita, H. Miura, S. Iga, and T. Nasuno (2005), Development of a global cloud resolving model – A multi-scale structure of tropical convections, *J. Earth Simulator*, *3*, 1–9.

Scoccimarro, E., S. Gualdi, A. Bellucci, A. Sanna, P. Giuseppe Fogli, E. Manzini, M. Vichi, P. Oddo, and A. Navarra (2011), Effects of tropical cyclones on ocean heat transport in a high-resolution coupled general circulation model, *Journal of Climate*, *24*, 4368–4384, doi:10.1175/2011JCLI4104.1.

Shen, B.-W., R. Atlas, J.-D. Chern, O. Reale, S.-J. Lin, T. Lee, and J. Chang (2006a), The 0.125 degree finite-volume general circulation model on the NASA Columbia supercomputer: Preliminary simulations of mesoscale vortices, *Geophys. Res. Lett.*, *33*, L05801, doi:10.1029/2005GL024594.

Shen, B.-W., R. Atlas, O. Reale, S.-J. Lin, J.-D. Chern, J. Chang, C. Henze, and J.-L. Li (2006b), Hurricane forecasts with a global mesoscale-resolving model: Preliminary results with hurricane Katrina (2005), *Geophys. Res. Lett.*, *33*, L13813, doi:10.1029/2006GL026143.

Simmons, A. J., and D. M. Burridge (1981), An energy and angular-momentum conserving vertical finite-difference scheme and hybrid vertical coordinates, *Mon. Wea. Rev.*, *109*, 758–766.

Skamarock, W. C., J. B. Klemp, J. Dudhia, D. O. Gill, D. M. Barker, M. G. Duda, X.-Y. Huang, W. Wang, and J. G. Powers (2008), A description of the Advanced Research WRF Version 3, *NCAR Tech. Note NCAR/TN-475+STR*, National Center for Atmospheric Research, Boulder, Colorado, 113 pp., available from http://www.ucar.edu/library/collections/technotes/technotes.jsp.

Skamarock, W. C., J. Klemp, M. Duda, S.-H. Park, L. Fowler, T. Ringler, J. Thuburn, M. Gunzburger, and L. Ju (2010), Global non-hydrostatic modeling using Voronoi meshes: The MPAS model, Presentation at ECMWF Non-Hydrostatic Workshop, Reading, U.K. Nov. 8-10, 2010.

Smith, R. K. (2000), The role of cumulus convection in hurricanes and its representation in hurricane models, *Rev. Geophys.*, *38*, 465–490, doi:10.1029/1999RG000080.

Smith, R. K., and S. Vogl (2008), A simple model of the hurricane boundary layer revisited, *Quart. J. Roy. Meteor. Soc.*, *134*, 337–351, doi:10.1002/qj.216.

Stainforth, D. A., M. R. Allen, E. R. Tredger, and L. A. Smith (2007), Confidence, uncertainty and decision-support relevance in climate predictions, *Phil. Trans. R. Soc. A*, *365*(1857), 2145–2161.

Stainforth, D. A., et al. (2005), Uncertainty in predictions of the climate response to rising levels of greenhouse gases, *Nature*, *433*, 403–406, doi:10.1038/nature03301.

Sugi, M., H. Murakami, and J. Yoshimura (2009), A reduction in global tropical cyclone frequency due to global warming, *SOLA*, *5*, 164–167, doi:10.2151/sola.2009-042.

Sundqvist, H. (1965), Numerical simulation of the development of tropical cyclones with a ten-level model. Part 1., *Tellus*, *22*, 359–390.

Taylor, M., J. Tribbia, and M. Iskandarani (1997), The spectral element method for the shallow water equations on the sphere, *J. Comput. Phys.*, *130*, 92–108.

Taylor, M. A. (2011), Conservation of mass and energy for the moist atmospheric primitive equations on unstructured grids, in *Numerical Techniques for Global Atmospheric Models*, *Lecture Notes in Computational Science and Engineering*, vol. 80, edited by P. H. Lauritzen, C. Jablonowski, M. A. Taylor, and R. D. Nair, pp. 357–380, Springer.

Taylor, M. A., and A. Fournier (2010), A compatible and conservative spectral element method on unstructured grids, *J. Comput. Phys.*, *229*, 5879–5895.

Taylor, M. A., J. Edwards, S. Thomas, and R. D. Nair (2007), A mass and energy conserving spectral element atmospheric dynamical core on the cubed-sphere grid, *Journal of Physics: Conference Series*, *78*, 012074, available online at http://www.iop.org/EJ/toc/1742-6596/78/1.

Taylor, M. A., J. Edwards, and A. St-Cyr (2008), Petascale atmospheric models for the Community Climate System Model: New developments and evaluation of scalable dynamical cores, *Journal of Physics: Conference Series*, *125*, 012023.

Thomas, S. J., and R. D. Loft (2005), The NCAR spectral element climate dynamical core: Semi-implicit Eulerian formulation, *J. Sci. Comput.*, *25*, 307–322.

Tiedtke, M. (1987), Parametrization of non-convective condensation processes, *Lecture Notes NWP Course Parametrization of Diabatic Processes*, European Centre for Medium-Range Weather Forecasts, Reading, U.K., 11 pp.

Tomita, H., and M. Satoh (2004), A new dynamical framework of nonhydrostatic global model using the icosahedral grid, *Fluid Dyn. Res.*, *34*, 357–400.

Ullrich, P. A., P. H. Lauritzen, and C. Jablonowski (2009), Geometrically Exact Conservative Remapping (GECoRe): Regular latitude-longitude and cubed-sphere grids, *Mon. Wea. Rev.*, *137*, 1721–1741, doi:10.1175/2008MWR2817.1.

van Sang, N., R. K. Smith, and M. T. Montgomery (2008), Tropical-cyclone intensification and predictability in three dimensions, *Quart. J. Roy. Meteor. Soc.*, *134*, 563–582, doi:10.1002/qj.235.

Walsh, K. J. E. (2008), The ability of climate models to generate tropical cyclones: implications for prediction, in *Climate Change Research Progress*, edited by L. Peretz, pp. 313–329, Nova Publishers.

Walsh, K. J. E., K. Nguyen, and J. L. McGregor (2004), Fine-resolution regional climate model simulations of the impact of climate change on tropical cyclones near Australia, *Climate Dyn.*, *22*, 47–56, doi:10.1007/s00382-003-0362-0.

Wan, H. (2009), Developing and testing a hydrostatic atmospheric dynamical core on triangular grids, *Reports on Earth System Science 65*, Max Planck Institute for Meteorology, Hamburg, Germany, 153 pp., available from http://www.mpimet.mpg.de/en/wissenschaft/publikationen/berichte-erdsystemforschung.html.

Wang, D., X. Liang, Y. Zhao, and B. Wang (2008), A comparison of two tropical cyclone bogussing schemes, *Wea. Forecasting*, *23*, 194–204, doi: 10.1175/2007WAF2006094.1.

Wang, Y., and J. Xu (2010), Energy production, frictional dissipation, and maximum intensity of a numerically simulated tropical cyclone, *J. Atmos. Sci.*, *67*, 97–116, doi:10.1175/2009JAS3143.1.

Wehner, M. F., G. Bala, P. Duffy, A. A. Mirin, and R. Romano (2010), Towards direct simulation of future tropical cyclone statistics in a high-resolution global atmospheric model, *Adv. Meteor.*, *2010*, 915303, doi:10.1155/2010/915303.

Weller, H., H. G. Weller, and A. Fournier (2009), Voronoi, Delaunay and block structured mesh refinement for solution of the shallow water equations on the sphere, *Mon. Wea. Rev.*, *137*, 4208–4224.

White, A. A., B. J. Hoskins, I. Roulstone, and A. Staniforth (2005), Consistent approximate models of the global atmosphere: shallow, deep, hydrostatic, quasi-hydrostatic and non-hydrostatic, *Quart. J. Roy. Meteor. Soc.*, *131*, 2081–2107.

Whitehead, J., C. Jablonowski, R. B. Rood, and P. H. Lauritzen (2011), A stability analysis of divergence damping on a latitude-longitude grid, *Mon. Wea. Rev.*, *139*, 2976–2993.

Williamson, D. L. (1968), Integration of the barotropic vorticity equation on a spherical geodesic grid, *Tellus*, *20*, 642–653.

Williamson, D. L. (2002), Time-split versus process-split coupling of parameterizations and dynamical core, *Mon. Wea. Rev.*, *130*, 2024–2041, doi:10.1175/1520-0493(2002)130<2024:TSVPSC>2.0.CO;2.

Williamson, D. L. (2008a), Equivalent finite volume and Eulerian spectral transform horizontal resolutions established from aqua-planet simulations, *Tellus*, *60*, 839–847, doi:10.1111/j.1600-0870.2008.00340.x.

Williamson, D. L. (2008b), Convergence of aqua-planet simulations with increasing resolution in the Community Atmospheric Model, Version 3, *Tellus*, *60*, 848–862, doi:10.1111/j.1600-0870.2008.00339.x.

Williamson, D. L. (2011), Effect of time steps and time scales on parameterization suites, *Quart. J. Roy. Meteor. Soc.*, in review.

Williamson, D. L., and J. G. Olson (1994), Climate simulations with a semi-Lagrangian version of the NCAR Community Climate Model, *Mon. Wea. Rev.*, *122*(7), 1594–1610.

Williamson, D. L., J. B. Drake, J. J. Hack, R. Jakob, and P. N. Swarztrauber (1992), A standard test set for numerical approximations to the shallow water equations in spherical geometry, *J. Comput. Phys.*, *102*, 211–224, doi:10.1016/S0021-9991(05)80016-6.

Yamada, Y., K. Oouchi, M. Satoh, H. Tomita, and W. Yanase (2010), Projection of changes in tropical cyclone activity and cloud height due to greenhouse warming: global cloud-system-resolving approach, *Geophys. Res. Lett.*, *37*, L07709, doi: 10.1029/2010GL042518.

Yamasaki, M. (1965a), A tropical cyclone model with parameterized vertical partition of released latent heat., *J. Meteor. Soc. Japan*, *46*, 202–214.

Yamasaki, M. (1965b), Detailed analysis of a tropical cyclone simulated with a 13-layer model., *Pap. Meteorol. Geophys.*, *19*, 559–585.

Yoshimura, J., and M. Sugi (2005), Tropical cyclone climatology in a high-resolution AGCM – Impacts of SST warming and $CO_2$ increase –, *SOLA*, *1*, 133–136, doi: 10.2151/sola.2005-035.

Zhang, F., and J. A. Sippel (2009), Effects of moist convection on hurricane predictability, *J. Atmos. Sci.*, *66*, 1944–1961, doi:10.1175/2009JAS2824.1.

Zhang, G. J., and N. A. McFarlane (1995), Sensitivity of climate simulations to the parameterization of cumulus convection in the Canadian Climate Centre General Circulation Model, *Atmos.–Ocean*, *33*, 407–446.

Zhao, M., and I. M. Held (2010), An analysis of the effect of global warming on the intensity of Atlantic hurricanes using a GCM with statistical refinement, *J. Climate*, *23*, 6382–6393, doi:10.1175/2010JCLI3837.1.

Zhao, M., I. M. Held, S.-J. Lin, and G. A. Vecchi (2009), Simulations of global hurricane climatology, interannual variability, and response to global warming using a 50-km resolution GCM, *J. Climate*, *22*, 6653–6678.

Zhu, H., and A. Thorpe (2006), Predictability of extratropical cyclones: The influence of initial condition and model uncertainties., *J. Atmos. Sci.*, *63*, 1483–1497, doi: 10.1175/JAS3688.1.